TU Delft Delft University of Technology
Faculty of Applied Sciences
Chemical Engineering

BASF
The Chemical Company

Dynamic Modelling and Validation of an Industrial Adipic Acid Plant

---

The content of this report is **confidential**.

Author:	Coen de Ruiter
Student number:	1168185
Email address:	CHdeRuiter@gmail.com
Report number:	P&E-2340
Supervisors:	Dr.ir. Herman Kramer Ali Mesbah MSc Dr. Karsten Bartling (BASF)
2nd and 3rd reviewer:	Prof.dr.ir. Andrzej Stankiewicz Prof.ir. Johan Grievink
Date:	9th of September 2009

Summary

An industrial crystallization process is a complex process consisting of a lot of physical phenomena. Temperature, stirrer speed and other process inputs determine the rate of physical phenomena like agglomeration and growth. This study aims to develop a dynamic model structure that describes the physical phenomena in the crystallization process. The population balance equation is the basis of the model structure. Simple kinetic relations and the concentration balance are coupled to the population balance. The high resolution finite volume scheme is applied as the numerical solution method to solve the population balance equation. The dynamic model is validated with experimental results from an adipic acid crystallizer. Gathering the experimental results is a large part of this study. The crystal size distribution was measured with a new image analysis sensor. BASF has developed this sensor with sheathed streams that can measure the crystal size distribution and crystal shape on-line even at a high crystal concentration. Validation experiments with an off-line measurement device shows that the sensor give excellent results. Other experiments shows that the sensor works for longer times without any problems. The process inputs of the crystallizer are changed to see the effect on the crystal size distribution (CSD). A change in the temperature seems to have the largest influence on the CSD. A relative change of 2% in temperature can change the CSD for more than 10%. The recirculation rate is the most effective process input to vary. A relative change of 50% of the recirculation rate gives a change in the CSD for more than 20%. These experimental results were used to validate the model structure. The model results shows that the model can simulate the mean crystal size measured with the sensor accurately. Improvements on the kinetic relations have to be made to also simulate the complete CSD.

Table of contents

1. Introduction

Crystallization is commonly used in the chemical industry to purify and produce solid particles. The centrifuged and dried solid product is normally bagged and shipped to customers. For adipic acid crystals it is not uncommon that the crystals clog together in the bags to big chunks and can therefore not be used by the customers. As a result the customers need to return the product to the producer. The producer needs to dissolve the product and crystallize the product again. Next to the loss of money, time and energy of this operation the producer will also lose part of his image. Therefore it is important for the producer to prevent the problems caused by the clogging of the crystals. The rate of clogging of the crystals is determined by the particle characteristics, like size, shape and mother liquor inclusion. The particle characteristics are affected by the crystallization process, centrifuging process and drying. The crystal characteristics is mainly determined by the design of the crystallizer and the operation of the crystallization process. It is therefore of key importance to control the kinetics during the crystallization process.

In this report the effect of the process inputs on the product quality of adipic acid is studied. This is done by measuring the crystal size distribution (CSD) with a new type of sensor on-line in the outlet flow of the crystallizer. And by developing a model structure that describes the dynamic behaviour of the crystallization process. This work is done in cooperation with BASF, one of the world's main adipic acid producers (app. 12.5% market share in 1999, Musser, 2008).

1.1 Adipic acid

Adipic acid is produced worldwide on a large scale as a raw material for the production of polyamides. The manufacturing of the polyamide fibre is one of the dominant processes in the synthetic fibre industry. Adipic acid could be produced in several ways but all large-scale production processes are done via nitric acid oxidation of cyclohexanol (KA oil). Adipic acid is nearly always separated and purified by crystallization (Musser, 2008). A simple process flow scheme for the production of adipic acid is shown in Figure 1.1. The adipic acid crystals are odourless and colourless and have an acidic taste.

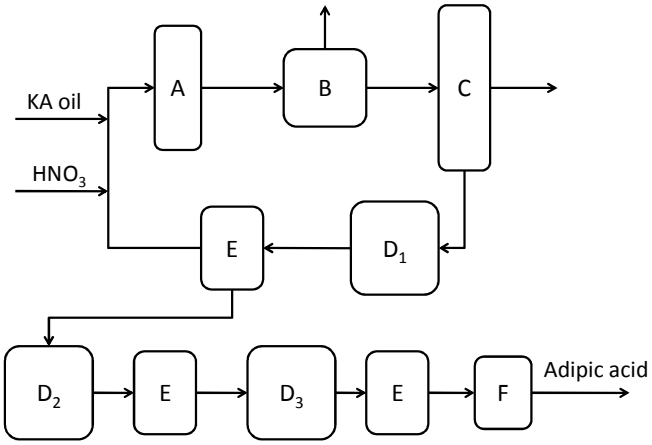

Figure 1.1: A simple process flow scheme for the production of adipic acid; a) reaction section, b) gas separation section, c) concentrator, d) crystallizer, e) centrifuge, f) dryer.

For the purification and production of the solid adipic acid particles there are three crystallization steps involved. These steps are required to meet the purity specifications of the final product. Important for the product quality of the last crystallization step beside the purity of the crystals is the crystal shape and size. Therefore the focus of this report is on the third and final crystallization step.

1.2 Product quality of adipic acid

In comparison to lab experiments industrial crystallization processes often shows fluctuations in product quality (Gerstlauer et al., 2006). An important measure for the product quality is the crystal size distribution. The crystal size distribution is a measure for the flowability of the crystals (Bayer et al., 2003) and therefore also the handling of the crystals as a solid product. Furthermore, the crystal shape influences the flowability of the final product. Figure 1.2 shows an image of surfboard shaped adipic acid crystals from an industrial crystallizer and an image of large compact adipic acid crystals from a lab experiment. The large hydrophilic surface of the surfboard shaped crystals will increase the agglomeration property of the crystals. Figure 1.3 shows an image of a single adipic acid crystal and a schematic drawing of the positioning of the adipic acid molecules in the crystal. Due to the positioning of the molecules the large surfboard surface is hydrophilic. The hydrophilic surface will attract hydrophilic surfaces of other crystals this will increase the agglomeration property of the crystals. Therefore the compact crystals produced in the lab are wanted over the industrial produced crystals.

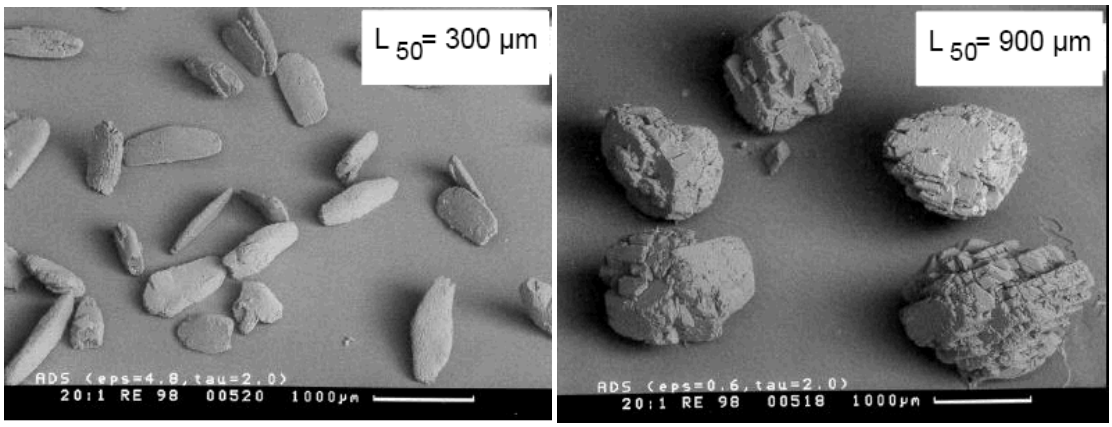

Figure 1.2: *Left:* Industrial produced surfboard shaped adipic acid crystals. *Right:* Lab produced large compact adipic acid crystals.

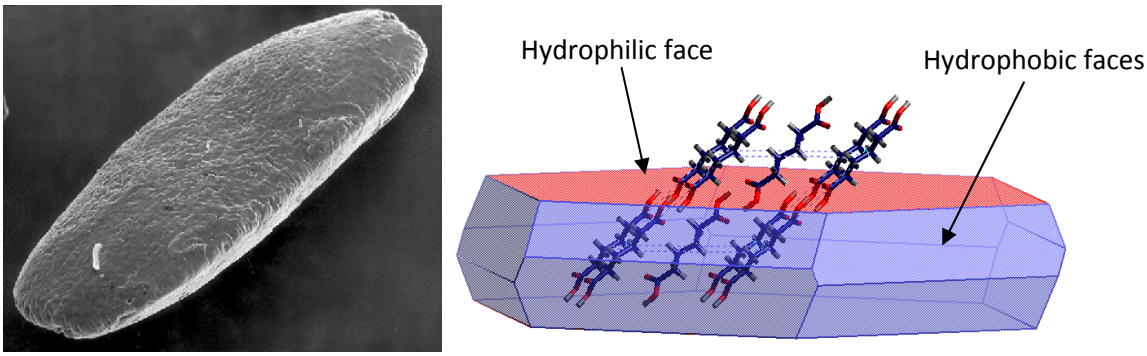

Figure 1.3: *Left*: A SEM picture of an industrial produced adipic acid crystal. *Right*: A schematic drawing of a adipic acid crystal. The red groups are the hydrophilic groups of the adipic acid molecule. Due to the positioning of the molecules in the crystal the surface of the crystal is hydrophilic and therefore the crystals will agglomerate easily.

1.3 Goal of the project

Process inputs, like crystallizer temperature, residence time and stirrer speed, influence the crystallization process. This complex process consist of physical phenomena like agglomeration, attrition, growth and nucleation. These physical phenomena do all contribute to the characteristics of the final product. Indirectly the process inputs will determine the product quality. Therefore the aim of this research is to investigate the contribution of the different process inputs on the product characteristics. Also the contribution of the process inputs on the physical phenomena in the

crystallizer is investigated. The research question is: what is the effect of the process inputs on the physical phenomena in the crystallizer and what is the effect of these phenomena on the product characteristics? Two question will arise from this research question. How can the product characteristics be measured? And more important how to investigate the effect of the physical phenomena independently?

Experiments are done to measure the evolution of the product quality in the crystallizer and a dynamic model is developed to study the effect of the process inputs on the physical phenomena. The crystal size distribution is one of the important properties of the product characteristics. In this report a newly developed image analysis sensor is used to measure the crystal size distribution and shape characteristics of the crystals. This sensor is applied in the process for the first time and therefore the sensor is tested, optimized and validated first. Afterwards the dynamics of a number of parameters related to the CSD in the crystallizer are measured with the sensor. In addition a dynamic model of the crystallization process is developed to simulate the crystal size distribution in the crystallizer and to study the effect of the variation of the process inputs on the physical phenomena independently. The model structure is based on a numerical solution of the population balance equation. Next to the population balance equation also kinetic relations and a mass balance over the crystallizer is derived and adopted. For the population balance a numerical solution method is applied to solve the equation. The model structure is tested and validated with experimental results. For the validation some parameters are estimated. This is done rigorously because a parameter estimation study falls outside the scope of this research. An overview of the approach of this research is shown in Figure 1.4.

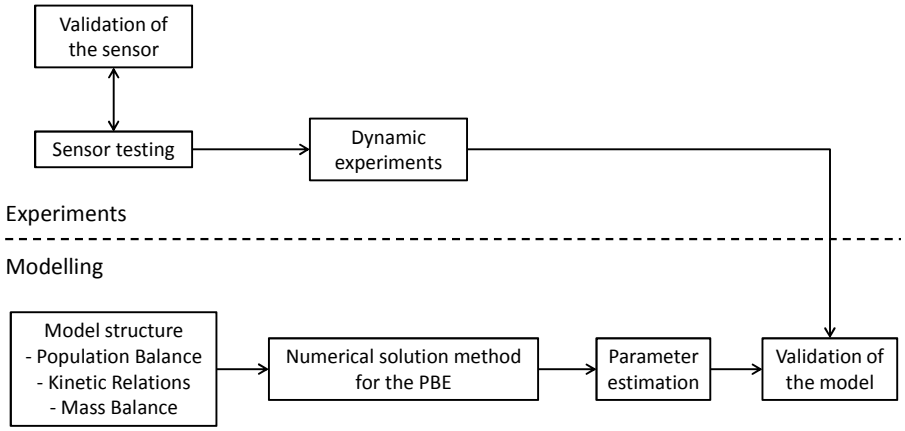

Figure 1.4: Schematic overview of the approach of this research

This report starts with a literature review about the crystallization of adipic acid on an industrial scale and the physical phenomena that will occur. Also a study is done about the different measurement methods for the crystal size distribution and especially about the newly developed sensor. The theoretical part will be finalized with a study about the population balance equation and the solution methods for this equation. The report will continue with an overview of the experimental setups used in the research. The experiments that are done are described and the model structure is developed. The results of the experiments and the modelling are described in the fourth chapter. The conclusions are discussed in the fifth chapter and the final chapter discusses the recommendations to improve the experimental work and the model structure.

2. Theory

This chapter is divided into three parts. The first part is about the crystallization of adipic acid. The crystallization method, the solubility of adipic acid in water and other physical parameters of adipic acid are described. The second part is about the different methods for crystal size distribution measurements, especially about the image analysis sensor with a special particle concentration dilution method developed by BASF. The third part is about the population balance equation. The population balance equation is adapted for the crystallization of adipic acid and a solution method for the population balance equation is selected and derived as described in the literature.

2.1 Crystallization of adipic acid

Adipic acid is crystallized at the end of the production process to obtain a solid product. The driving force for crystallization is supersaturation of the solute in the solvent. The supersaturation of the solute in the solvent can be created in several ways. For large industrial processes cooling crystallisation or evaporative crystallization is often used. The first method implies that the solution will be cooled down so that the solubility of the solute in the solvent decreases until a supersaturated state is reached. The second method implies that the solvent is evaporated so that the concentration of the solute in solvent increases until also a supersaturated state is reached. In continuous industrial crystallization processes evaporative crystallization is frequently used. To control the crystallization process the temperature is set to a constant value to have a constant supersaturation rate. The temperature is controlled by the pressure in the crystallizer. For an adipic acid – water mixture below 100 °C this implies that the pressure inside the crystallizer needs to be lower than the atmospheric pressure. For the industrial crystallization of adipic acid the hot feed is cooled down by evaporation of the solvent. This combination of cooling and evaporation crystallization is also called flash crystallization.

The solubility of the solute in the solvent is therefore very important for the crystallization process. Adipic acid is slightly soluble in water at room temperature but the solubility increases steeply when the temperature is increased. The solubility of adipic acid in water is measured before (BASF, 2006, see Figure 2.1). Additional physical data of adipic acid are listed in Appendix 1.

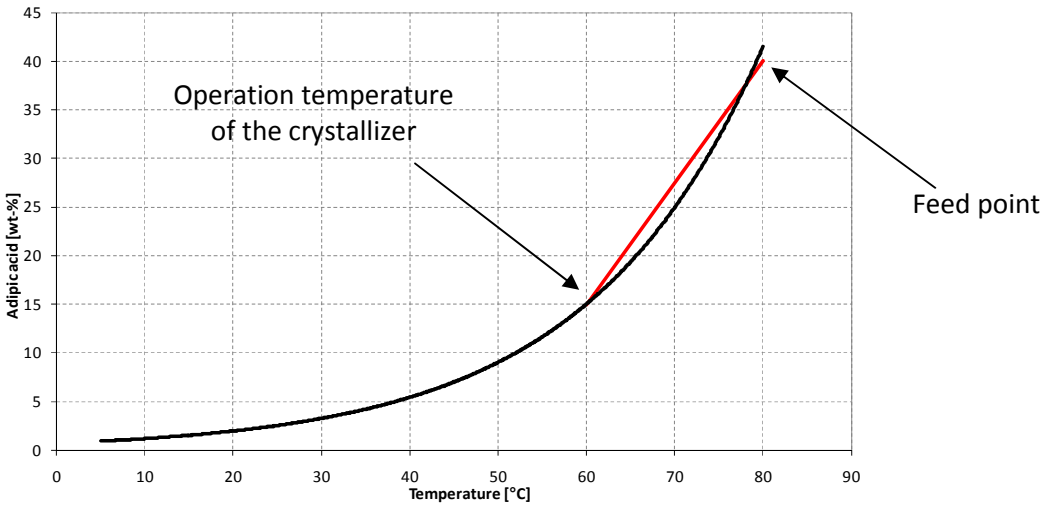

Figure 2.1: The solubility curve of adipic acid in water, mass fraction versus temperature (BASF, 2006)

Supersaturation is the driving force for growth of crystals in the crystallizer. Furthermore, supersaturation is the driving force for nucleation. In an industrial crystallizer at steady state conditions secondary nucleation is dominant over primary nucleation (Zhu et al., 2005). The relative supersaturation rate is too low for primary nucleation and the presence of other crystalline particles lead to the dominance of secondary nucleation. However primary nucleation can occur at the feed

point in the crystallizer. The feed entering the crystallizer, 40 wt-% and 80 °C, is cooled down to 60 °C. The cooling line crosses the solubility curve (see Figure 2.1) therefore primary nucleation can occur at the feed point. Besides the processes that are mainly driven by supersaturation also mechanical processes play an important role in the industrial crystallization of adipic acid. Secondary nucleation or attrition of crystals are physical phenomena that will occur, especially in industrial crystallizers. Attrition of crystals will occur upon impact of the crystals with the impeller or the wall of the crystallizer. The fragments that result from the collision between the crystals and the impeller or wall are the main source for secondary nucleation. Agglomeration is a phenomenon that, next to supersaturation, is also driven by mechanical forces. When a crystal hits another crystal there exists the possibility that both crystals stick together and agglomerate. The chance that two crystals hits each other is larger at increased stirrer speeds.
All these physical phenomena such as growth, secondary nucleation, attrition and agglomeration will occur during the crystallization of adipic acid (David et al., 1991, Riemann and Gerstlauer, 2003, Costa et al., 2005).

2.2 Crystal size distribution measurement

The crystal size distribution is an important measure for the product quality. An on-line crystal size distribution sensor gives the CSD that is present in the crystallizer at that moment in time and an on-line sensor decrease the measurement errors made by measuring after centrifuging and drying or sampling. There are some methods, such as laser diffraction, ultrasound and image analysis, to measure crystal size distribution on-line in the crystallizer. The general weakness of these methods is that agglomerated crystals, different shapes of the crystals and the volume of the crystals cannot be measured accurately or cannot even be determined at all. The most common commercial available on-line crystal size distribution device is a laser diffraction sensor. The laser diffraction sensor measures the volume of the crystals very accurately but cannot measure the size and shape of the crystal. Some companies developed a system that is a combination between an image analysis sensor for the size and shape of the crystal and a laser diffraction sensor for the volume of the crystal (Ankersmid, 2009). The disadvantage of an image analysis sensor in an industrial crystallizer is that the crystal concentration is often too high and that transparent crystals cannot be measured. The research group of Dr. Michael Schäfer, BASF GCT/P, has developed an image analysis sensor, called the Hüllstrom (sheathed stream) sensor, together with a software tool that eradicates these limitations.

A sample of the crystallizer suspension is diluted before the measurement. The dilution is done with two sheathed streams. A sample from the suspension of the crystallizer is taken and sheathed with a fluid and measured. The sheathed streams will squeeze the product stream to a very thin stream so that all particles can be measured individually. All streams, the sheathed streams and the product stream, have a laminar flow, so mixing will not occur. This dilution method with sheathed streams cannot be done with every liquid. If there is a chemical potential (e.g. concentration difference or temperature difference) between the sheathed streams and the product stream schlieren can occur. Schlieren are caused by light refraction at the boundary between two layers (Cox and McLachlan, Jr., 1974) and will disturb the measurement of the crystal size distribution. A depiction of schlieren is shown in Figure 2.2. To minimize the amount of schlieren the fluid to sheath the product stream needs to closely mimic the product stream in terms of concentration and temperature.

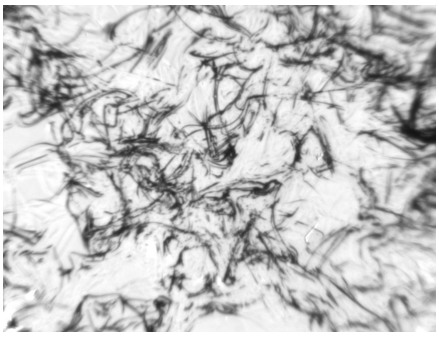

Figure 2.2: Schlieren are caused by a difference in chemical potential of the product stream and sheathed streams. Here condensate (sheathed stream, 90 °C) and adipic acid (product stream, 15 wt-%, 60 °C).

The name of the sensor refers to the German word of sheathed stream; 'Hüllstrom'. In this report the name 'Hüllstrom sensor' is used to refer to the image analysis sensor that uses the sheathed streams dilution method to measure the crystal size distribution.

2.3 Dynamic modelling

The dynamic behavior of a crystallization process can be described with a population balance equation (Hulbert and Katz, 1964 and Ramkrishna, 1985). In this section a literature review is given about the population balance equation as well as different ways to solve the population balance equation.

2.3.1 Population Balance Equation

Growth, nucleation, attrition, breakage, dissolution and agglomeration of crystals can change the crystal size distribution in a crystallizer. The population balance couples these crystal kinetics and provide a differential equation for the crystal size distribution or a number density distribution in general. The general one-dimensional form of the population balance equation (PBE) for a continuous well mixed process given by Ramkrishna (1985) is shown in equation 2.1.

$$\frac{\partial n(t,L)}{\partial t}+\frac{\partial\left[G(t,L)n(t,L)\right]}{\partial L}=\frac{\dot{V}_{in}}{V}n_{in}(t,L)-\frac{\dot{V}_{out}}{V}n(t,L)+B-D \quad [2.1]$$

where *n(t,L)* denotes the number density function describing the crystal size distribution, *G* denotes the growth rate of the crystals, *L* denotes the characteristic length of the crystals and *t* denotes the time. The right hand side of the equation denotes the inlet and outlet streams and the birth and death terms (*B* and *D*, respectively). Hereby the assumption is made that the volume (*V*) in the crystallizer will not change with time.

The growth and dissolution of crystals are included in the convection term. All other kind of physical phenomena such as nucleation, attrition, agglomeration and breakage can be included in the birth and death terms. For the industrial continuous crystallization of adipic acid it can be assumed that primary nucleation and breakage will not occur in the crystallizer. In equation 2.2 the adopted population balance including secondary nucleation or attrition (*S*) and agglomeration (Q_{agg}) is shown.

$$\frac{\partial n(t,L)}{\partial t}+\frac{\partial\left[G(t,L)n(t,L)\right]}{\partial L}=\frac{\dot{V}_{in}}{V}n_{in}(t,L)-\frac{\dot{V}_{out}}{V}n(t,L)+Q_{agg}(t,L,n)+S(t,L,n) \quad [2.2]$$

The boundary conditions are $t<0$ and $L=[L_{\min}-L_{\max}]$.

The moments of the number density distribution are defined by Randolph and Larson (1988) and shown in equation 2.3. The moments are used to describe the number density distribution and are used to develop analytical solutions of number density distribution problems (Filbet and Laurençot,

2004). The moments can be used to calculate the mean crystal size, μ, and the coefficient of variation, *cv* (Chung et al., 1999). The latter is a measure of the width of the crystal size distribution. The definitions are shown in equation 2.4 and 2.5.

$$m_i = \int_0^\infty n(t,L)\,L^i dL \quad \text{for } i = [0-4] \qquad [2.3]$$

$$\mu = \frac{m_4}{m_3} \qquad [2.4]$$

$$cv = \sqrt{\frac{m_2 m_0}{m_1^2} - 1} \qquad [2.5]$$

2.3.2 Solution method for the population balance equation

The population balance equation is a partial differential equation that is a function of the characteristic crystal size (length) and time. There is a lack of analytical methods to solve the system when all the physical phenomena are considered. Therefore Hulbert and Katz (1964) and Randolph and Larson (1988) used the method of moments. This solution method solved PBE at different moments so that only a set of ordinary differential equations remain. The disadvantage is that the solution does not provide a full number density distribution in time. Therefore, numerical solution methods are applied to solve the PBE. In the literature there are numerous studies that use a numerical solution method to solve the PBE. Qamar (2007) compared and optimized a number of numerical solution methods to solve different kinds of problems in a mathematical way while David et al. (1991) used a numerical solution method to solve the PBE for a batch crystallization problem. Gerstlauer et al. (2006) even used a numerical solution method to solve the PBE for a continuous crystallization process. All these different literature studies are necessary to solve the PBE for a specific problem. The first type of literature studies give you a numerical method to solve PBE and the second and third type of literature studies give you an example of the application of the solution method and also an optimization of the kinetic relations that are coupled to the PBE.

Numerical solutions will introduce new difficulties like boundary value problems, initial value problems, and numerical diffusion problems. There are different numerical solution methods to overcome or reduce these problems. Mesbah et al. (2009) also compared different kinds of solution methods for different situations for solving the PBE. He gives a comprehensive overview of the strengths and weaknesses of the different solution methods. The most common numerical methods used are the method of moments, the method of weighted residuals (the commercial package PARSIVAL® belongs to this class) and the Monte Carlo methods. According to Mesbah et al.(2009) the most accurate method to solve the PBE for a problem for growth and nucleation is the method of characteristics (belonging to the method of lines). In this method the grid mesh will move with the growth rate and therefore there is no numerical diffusion. To account for nucleation a new grid needs to be added at the beginning of the grid mesh. The disadvantage of this method is the long calculation time. This will only increase more when the calculations are more complex and when more physical phenomena are taking into account. For the case that more physical phenomena play a role the finite volume method with high resolution scheme is a fast and accurate solution method. This method discretizes the length domain so that a set of ordinary differential equation (ODE) remain. To prevent numerical diffusion there is a high resolution scheme used to calculate the values on the grids. Often used high resolution schemes are the Koren or the Van Leer flux limiters. For more information about numerical solution methods of the PBE and high resolution schemes the reader is referred to Mesbah et al. (2009).

2.3.3 Discretization of PBE with high resolution scheme

The discretization of the PBE with growth, secondary nucleation and agglomeration with the finite volume method with a high resolution scheme is done by Qamar and Warnecke (2007a). The ODE´s that remain can be solved with an ODE solver like the Runge Kutta method of MATLAB.

To discretize the length domain the PBE (eq. 2.2) is integrated over the domain $\Omega_i = \left[L_{i-1/2}, L_{i+1/2} \right]$.

$$\int_{\Omega_i} \frac{\partial n(t,L)}{\partial t} dL = -\int_{\Omega_i} \frac{\partial G(t,L) n(t,L)}{\partial L} dL + \frac{\dot{V}_{in}}{V} \int_{\Omega_i} n_{in}(t,L)\, dL - \frac{\dot{V}_{out}}{V} \int_{\Omega_i} n_{out}(t,L)\, dL - \int_{\Omega_i} Q_{agg}(t,L,n)\, dx + \int_{\Omega_i} S(t,L,n)\, dL \quad [2.6]$$

The discretized population balance is shown in equation 2.7.

$$\frac{\partial n_i}{\partial t} = -\frac{1}{\Delta L_i} \left[(Gn)_{i+1/2} - (Gn)_{i-1/2} \right] + \frac{\dot{V}_{in}}{V} n_{in,i} - \frac{\dot{V}_{out}}{V} n_{out,i} - Q_{agg,i} + S_i \quad [2.7]$$

For the flux, $(Gn)_{i+1/2}$, a flux-limiting formula is used as shown in equation 2.8.

$$(Gn)_{i+1/2} = G_{i+1/2} \left(n_i + \frac{\Delta L_i}{2\Delta L_{i-1/2}} \Phi\left(r_i^+\right)\left(n_{i+1} - n_i\right) \right) \quad [2.8]$$

where $\Delta L_{i-1/2} = L_i - L_{i-1}$ and $\Delta L_i = L_{i+1/2} - L_{i-1/2}$

The Van Leer flux limiter is used (Qamar and Warnecke, 2007a). The definition of Van Leer´s flux limiter is shown in equation 2.9.

$$\Phi\left(r_i^+\right) = \frac{\left|r_i^+\right| + r_i^+}{1 + \left|r_i^+\right|} \quad [2.9]$$

The argument r_i^+ of equation 2.9 is the so called upwind ratio of two consecutive solution gradients and defined as shown in equation 2.10.

$$r_i^+ = \frac{n_i - n_{i-1} + \varepsilon}{n_{i+1} - n_i + \varepsilon} \text{ with } \varepsilon = 10^{-10} \quad [2.10]$$

For the flux $(Gn)_{i-½}$ for *i* is 1, 2 and N+1 boundary equations need to be defined as done by Qamar et al. (2007). The boundary condition of the first grid point is shown in equation 2.11.

$$(Gn)_{½} = 0 \quad [2.11]$$

For the second and last (N[th]) grid equation 2.12 and 2.13 give the boundary solutions.

$$(Gn)_{1½} = G_{1½} \left(\frac{\left(2\Delta L_{1½} - \Delta L_1\right) n_1 + \Delta L_1 n_2}{2\Delta L_{1½}} \right) \quad [2.12]$$

$$(Gn)_{N+½} = G_{N+½} \left(n_N + \frac{\Delta L_N}{2\Delta L_{N-½}} \left(n_N - n_{N-1}\right) \right) \quad [2.13]$$

3. Experimental work

This chapter consist of four sections. The first three sections describe in detail the experimental work done at the adipic acid plant at BASF in Ludwigshafen, i.e. the operation of the crystallizer, the sensor and the different kind of experiments are explained. The fourth section describes the development of the model, such as the type of model structure used, the assumptions made and the initial and boundary conditions employed for the model.

3.1 Crystallizer

The measurements are done in the outlet flow of the crystallizer of the final solid formation step of the production process for adipic acid. For this crystallizer the product quality is very important. Flowability, crystal shape, crystal size (distribution), colour and purity are parameters that describe the product quality. With the Hüllstrom sensor the crystal size distribution and crystal shape can be measured (see Chapter 3.2 for details).

3.1.1 Draft Tube Crystallizer

The crystal size distribution measurements are done in a draft tube (DT) adipic acid crystallizer at BASF SE in Ludwigshafen am Rhein (Germany), internally called B1317A (or DP3). The crystallizer has a designed volume of 42 m³ and an effective volume of around 34 m³. The inlet flow is around 18 m³/h (S02), which results in a residence time of approximately 1,8 h. The operational settings of the crystallizer are a pressure of 200 mbar, a temperature of 60 °C and a stirrer speed of 35 rpm. The outlet flow of the crystallizer (about 75 m³/h, S05) is split into a recirculation loop (S06) and the actual product stream (S07) going to the subsequent process steps such as centrifugation and drying. The recirculation loop re-enters the crystallizer at the bottom of the crystallizer and is used to prevent sedimentation of crystals at the bottom. The flow of the recirculation loop is 60 m³/h and is heated by a heat exchanger to 65 °C. The resulting product stream of around 16 m³/h is going from the crystallizer to the centrifuges and dryers. A schematic overview of the crystallizer is shown in Figure 3.1 and an overview of the operating and process parameters is given in Table 3.1.

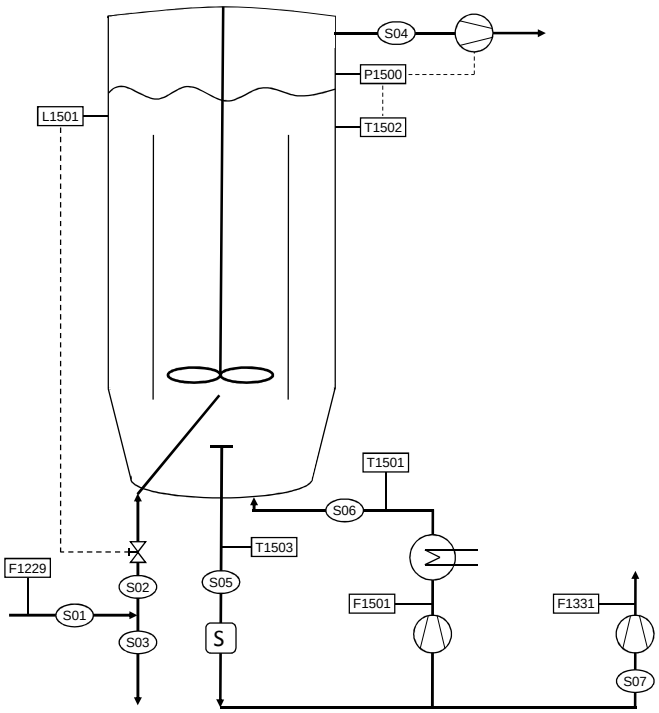

Figure 3.1: Schematic overview of the DP3 crystallizer. The labelling of the streams and the sensors for the measurement of the physical parameters are added to the Figure.

Table 3.1: Summary of the operating and process parameters of the crystallizer

Process/operating parameter	*Sensor*	*DP3*	*Unit*
Temperature	T1502	60	°C
Pressure	P1500	200	mbar
Volume		42	m^3
Level	L1501	74	%
		34	m^3
Stirrer speed	S1501	35	rpm
Recirculation rate	F1501	60	m^3/h
Recirculation temperature	T1501	65	°C
Inlet flow	F1229	18	m^3/h
Outlet flow	F1331	16	m^3/h

3.1.2 Sensors and control

The inlet flow of the crystallizer is measured by a flow sensor (F1229). The stream is split into two streams, one is the feed for the DP3 crystallizer and the other stream is the feed for the B1317 crystallizer. The parameters in the crystallizer are measured by a temperature (T1502), a pressure (P1500) and a level sensor (L1501). The temperature is automatically compared with the set temperature. If the difference is too big a new set point is given to the pressure control. The pressure sensor controls the vacuum pump and the set temperature is important for that. The level is controlled by the inlet flow of the crystallizer. If the level is too high or too low the inlet flow will be adjusted by closing or opening the inlet valve, respectively. The temperature of the outlet flow of the crystallizer is also measured (T1503). This sensor should give the same value as the temperature sensor in the crystallizer. If the difference between the measured values of the temperature sensors is too large something is wrong with the crystallizer, probably there is a shortcut between the inlet flow and the outlet flow due to heavy built up inside the crystallizer. This results in the inlet feed to exit the crystallizer right away without being mixed. As the inlet feed is at 80 °C an increase of the crystallizer outlet stream temperature indicates such a shortcut within the crystallizer.

The outlet flow is split into two streams, a recirculation stream that returns to the crystallizer and a product stream. The flow of the recirculation stream is also measured with a flow sensor (F1501). The recirculation stream is heated to 65 °C by a heat exchanger to prevent crystallization in the pipeline that can cause blockage. The temperature of this stream is monitored by a temperature sensor (T1501). Finally, the flow of the product stream is also measured with a flow meter (F1331) and the flow of this stream is manually controlled. Changes in the outlet flow are realized via the product pump.

The Hüllstrom sensor is placed in the outlet flow tube directly below the crystallizer. A flow of around 76 m^3/h is passing the sensor with a velocity of 2,7 m/s. From this product stream a small amount of sample is taken and the crystal size distribution is determined continuously.

3.2 Hüllstrom sensor

The image analysis sensor with a sheathed streams dilution method, the Hüllstrom sensor, described in Chapter 2.2 is used to measure the crystal size distribution. The sensor is placed in the outlet flow of the DP3 crystallizer without interrupting the process. The equipment needed for this operation and for the operation of the sensor are described in this section.

3.2.1 Sensor

The sensor is composed of a 50 cm long stainless steel cylinder with a diameter of 50 mm. At the backend of the sensor there is a 20 cm long black plastic cover with a diameter of 10 cm that houses the digital camera for image acquisition. The data cables are connected to the black cover at the

backend of the sensor (see Figure 3.2 for a picture of the frontend of the sensor and a picture of the sensor in the spool piece).

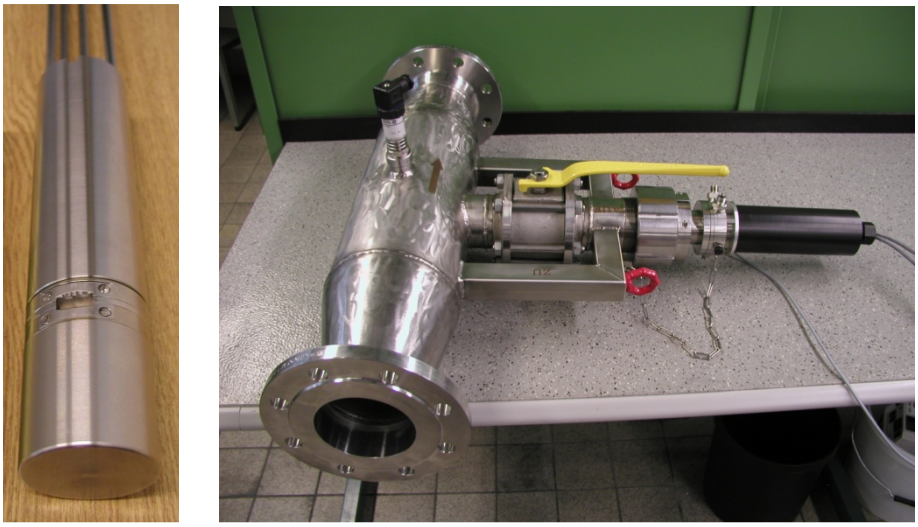

Figure 3.2: *Left:* Picture of the frontend of the Hüllstrom sensor. The sample point (square slit) is situated approximately 5 cm from the front end of the sensor. *Right:* Picture of the spool piece with the sensor installed in the process. In the black cover the camera is situated. The yellow handle is to open the process valve.

The camera is placed at the backend of the sensor at the opposite site of the sampling point in the black plastic cylinder (see Figure 3.2). The camera is sensitive to heat and placing it at the backend of the sensor keeps it furthest away from the warm product stream. This requires the use of an endoscope to connect the camera to the image acquisition point in the front tip of the sensor. A set of lenses will focus the camera on the measurement plane. The two sheathed streams are also entering the sensor at the backend and are routed inside the sensor to the front end. Within the sensor head a LED and a prism are used to provide background light to the camera (see Figure 3.3). The sheathed streams are entering from both sides of the product stream. The sheathed streams are laminar and will compress the product stream as described in Chapter 2.2. The combined waste stream will leave the sensor at the backend and flow to the drain.

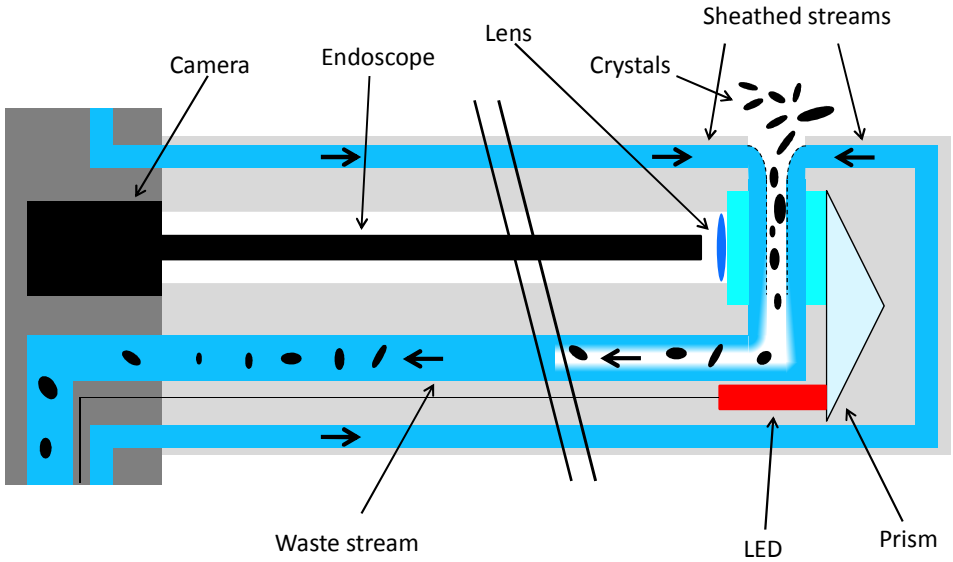

Figure 3.3: Schematic overview of the sensor; the backend part with the camera and the frontend part where the compressing (dilution) take place.

The sensor is installed into the process without interrupting the outlet flow of the process. This is achieved by installing the sensor into the outlet stream via a t-connector. The spool piece has a wider diameter to keep the overall flow velocity constant around the sensor (Figure 3.2 shows a picture of the spool piece and Figure 3.4 shows a schematic drawing of the spool piece).

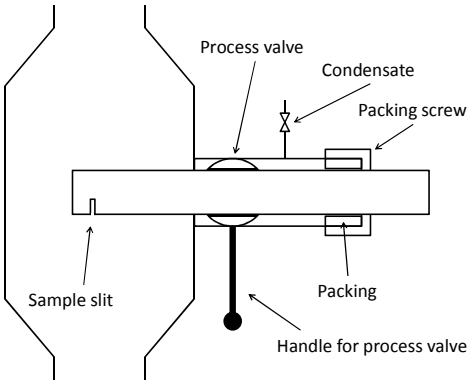

Figure 3.4: Schematic drawing of the spool piece with the sensor installed in the process.

With this system the sensor can be installed in the process safely, easily and without having to shut down the crystallizer. With the process valve being closed the sensor is inserted into the t-connector right up to the process valve. Afterwards the packing screw is tightened by hand to prevent product spill. Once the packing screw is tightened the process valve is opened and the sensor is rinsed and simultaneously heated with condensate. Finally the sensor is pushed all the way into the product stream of the crystallizer and securely locked into place.

3.2.2 Sheathed streams

To prevent the formation of schlieren (see Chapter 2.2) it is important that the sheathed streams have a similar temperature and concentration as the product stream, i.e. 60 °C and 15 wt-%, respectively. According to lab tests at BASF the temperature difference between both streams may not exceed 10 °C and the concentration difference may not exceed 2 wt-%.

The adipic acid solution used for the sheathed streams is prepared in a separate tank (B2221) and pumped in a recycle loop through the plant (HS01). At the DP3 crystallizer a small amount of the solution is tapped to use for the sheathed streams (HS02). The flow of this stream is controlled by a valve (HV01) and measured with a flow meter, also the pressure and temperature of this stream is monitored. To prevent blockage in the sheathed stream pipelines the temperature in the sheathed stream storage tank is increased so that the sheathed stream temperature at the sensor is 70 °C. After the sheathed streams pass through the Hüllstrom sensor the temperature and pressure of the sheathed stream is measured again. The flow of the product stream (HS03) is controlled by a pump (HP01). The pump pumps a certain amount of fluid from the sensor head to the drain. The pump is located after the measurement cell to prevent breakage or attrition caused by the pump. This fluid contains the sheathed streams and the product stream. The sheathed stream is measured with a flow meter before the sensor. The difference between the two flows, entering and leaving the sensor, is the amount of product sampled from the crystallizer. This value gives also an impression about the rate of dilution/compression. The combined stream of product and sheathed streams is going to the drain for waste water treatment. A schematic process and instrumentation diagram is shown in Figure 3.5.

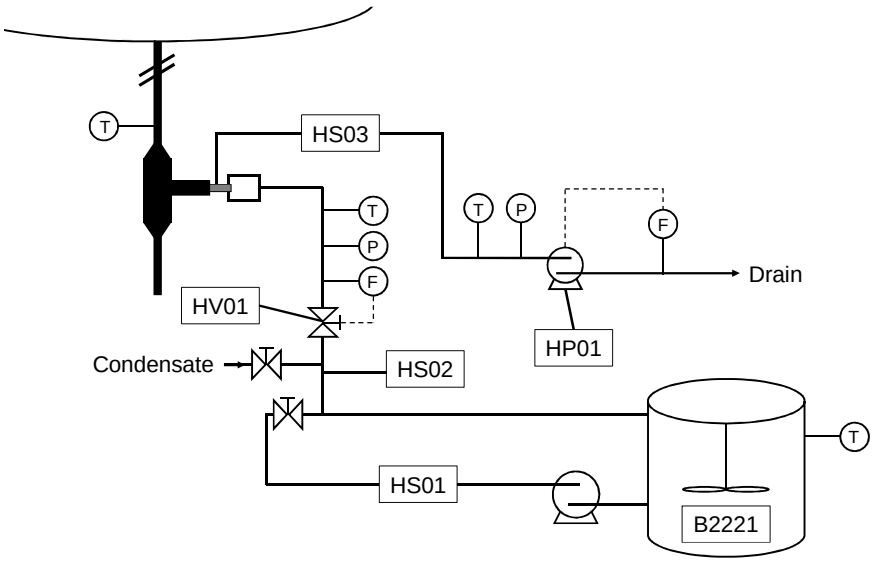

Figure 3.5: A schematic process and instrumentation diagram of the concentrated adipic acid solution used for the sheathed streams.

3.2.3 Measurement of the crystals

Due to the sheathed streams and the laminar flow of the product stream the crystals will orientate all in the same way in the measurement compartment. The forces on the crystals are shown in Figure 3.6. According to this analysis the shortest particle diameter is in the z-axis of the image. So the shortest diameter of the crystal will not be measured.

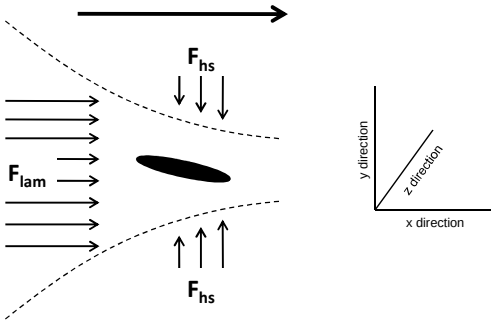

Figure 3.6: The forces on the crystals in the head of the sensor.

The digital images of the crystals made by the camera are 'translated' to different crystal sizes and characteristics of the crystal shape. The software determines seven different size and shape characteristics of the crystals, an overview is shown in table 3.2.

Table 3.2: Overview of the different crystal sizes and shape characteristics analyzed by the software.

Size or characteristic	*Equation*	*Explanation*
Maximum Feret diameter	$F_{\max}$	The maximum diameter of the crystal
Minimum Feret diameter	$F_{\min} = A_{crystal} / F_{\max}$	The area of the crystal divided by the max. Feret diameter
Waddel Disk diameter	$F_{area} = 2\sqrt{\frac{A_{crystal}}{\pi}}$	The diameter of a perfect circle with the same area as the crystal
Elongation	$E = F_{\max} / F_{\min}$	The ratio between the max. and min. Feret diameter
Heywood	$H = \frac{P}{2 \cdot \sqrt{\pi \cdot A_{crystal}}}$	The ratio between the perimeter of the crystal and the perimeter of a perfect sphere with the same area as the crystal
Volume	$V = 0,55 \cdot F_{\max} \cdot F_{\min}^2$	The volume of a rectangular cuboids of the max. and min. Feret diameter times a shape factor
3D equivalent diameter	$3dD = \sqrt[3]{\frac{6 \cdot V}{\pi}}$	The diameter of a perfect sphere with the same calculated volume as the crystal.

The measured crystal sizes and shape characteristics are stored as a number density distribution by the software. The software uses an anti-shading correction for all the pictures, which means that the background is removed from all the pictures including dirt at the lens or prism that sticks there during the entire measurement. Figure 3.7 gives a comparison between a image with and another image without shading correction.

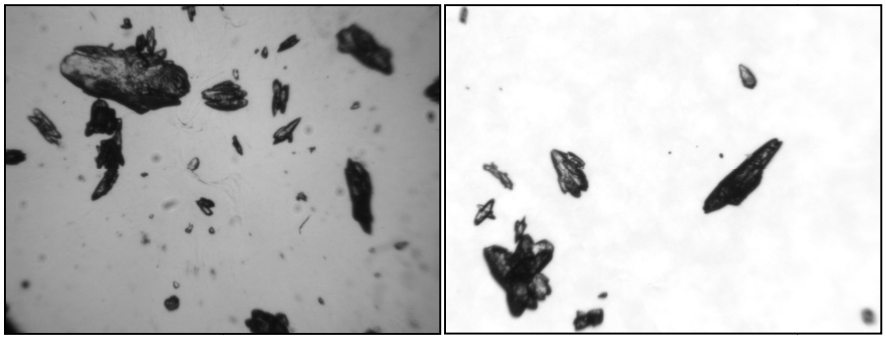

Figure 3.7: *Left:* An image without shading correction. *Right:* Another image with shading correction.

Not all the particles are measured, only the particles that are not touching the border of the image area are measured. Even particles with a transparent body can be measured. The borders of these particles are measured and the software recognizes this border and translates it to a solid particle. Particles that are overlapping or touching each other are measured as one particle; therefore it is important that the particle density in the image frame is not too high. This can be tuned manually by changing the outlet stream of the sensor (stream HS03 and pump HP01 in Figure 3.5).

To make a perfect size distribution an infinite number of particles is required. To see every small change in time a size distribution should be made as frequent as possible. To balance those opposite requirements the software generates a crystal size distribution after counting 1000 particles and 20.000 particles. This is for a time period of 15-30 seconds and for 5-10 minutes, respectively. These size distributions are stored and used for the analysis.

3.2.4 Representation of the crystal size distribution

The generated crystal size distributions by the software are cumulative distributions. To see trends in the distributions in time the x_{10}, x_{50} and x_{90} are taken and plotted versus the time (see Figure 3.8). The x_{50} is the crystal length were 50% of the crystals in the cumulative distribution are smaller and 50% are larger. For the x_{10}, 90% of the crystals are larger and 10% of the crystals are smaller for the x_{90} it is vice versa. Changes in these crystal lengths represent changes in the mean size of the CSD and the width of the distribution. The results are shown in cumulative distributions but most commonly in $x_{10}x_{50}x_{90}$ graphs.

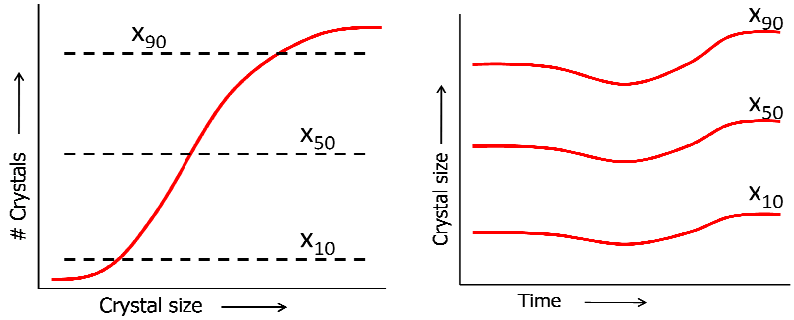

Figure 3.8: *Left:* The cumulative distribution, the intersection of the dashed line and distribution represent the crystal length were 50% of the crystals are larger and 50% are smaller, the x_{50}. *Right:* The x_{10}, x_{50} and x_{90} are plotted versus the time to see trends with time.

3.2.5 Off-line measurement

Every measurement is prone to errors and the results obtained therefore have to be validated by a separate measurement. For these validation experiments an off-line measurement system is used. The measurement method used for the off-line measurement is based on the same principle as the on-line measurement (image analysis). The difference is the way of dilution. In the off-line method a sample is added to a vessel containing 30 litre of saturated adipic acid solution. The saturated adipic acid solution in the vessel has the same temperature and concentration as in the process so no crystals will dissolve or grow. A small stream out of the vessel is continuously measured with an image analysis sensor. From these measurements also a crystal size distribution is generated. An overview of the off-line measurement setup is shown in Appendix 2.

3.3 Experiments

In this work the Hüllstrom sensor is used for the first time in an operational chemical plant. Tests at BASF showed that the Hüllstrom sensor measured crystal size distributions properly in an off-line lab setup. For the on-line plant data acquisition the entire setup is designed to install the Hüllstrom sensor safely and without interrupting the crystallization process. The aims of the experiments designed in this section are to validate the measurement outcome of the sensor, to operate the sensor at steady state and to measure dynamics in crystal size distribution when the operational parameters of the crystallization process are changed. Series of experiments have been designed to fulfil these aims.

3.3.1 Validation experiments

Validation of the measurements made by the Hüllstrom sensor comprises the first series of experiments. The correctness of crystal size distribution measured by the sensor needs to be confirmed. The distribution can be different due to the sampling of the sensor and also due to the sensor settings. For example, schlieren or a high concentration of particles will give a measurement error (see Section 2.2). These problems can be circumvented by adjusting the settings of the software of the sensor or the concentration in the tank of the sheathed stream. An error caused by the sampling of the sensor can also be corrected in the software but the magnitude of the deviation needs to be determined first.

Direction of the sampling slit

The direction of the sampling slit of the sensor is the only variable in the sampling process that cannot be adjusted in the software. The sampling slit can be rotated 360° with respect to the overall crystallizer exit flow, which is visualized in Figure 3.9. Only the rotation from 0° to 180° is evaluated because the rotation from 180° to 360° will give the same results.

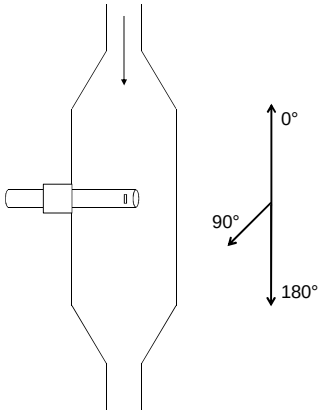

Figure 3.9: The sampling slit can be rotated from 0° to 180°; in the drawing the slit is rotated to 90° with respect to the overall crystallizer outlet flow.

To investigate the influence of the direction of the sampling slit an experiment was done where the sensor slit was rotated from 0° to 180° with otherwise identical process conditions. In this experiment differences in crystal size distribution should only be caused by the direction of the sampling slit.

On-line-off-line measurement
To validate the outcome of the sensor the results need to be compared with another accurate measurement. A combined on-line-off-line measurement was done. It is important that the sample that was tapped gives an accurate representation of the crystal size distribution in the crystallizer. Therefore an isokinetic sample point was designed and constructed into the process. In Appendix 2 the position and a schematic drawing of the sample point is shown.

The sample point is located after the product pump to the centrifuges. The volumetric flow in this tube is smaller than in the outlet flow tube where the Hüllstrom sensor is located. Furthermore, the pressure is different at these two points. At the sensor the pressure is around 1 bar (absolute) and at the off-line sampling point the pressure is around 5 bar. Nevertheless this should not contribute to a different crystal size distribution. The diameter of the internal tube is 20 mm and it reaches about 50 cm into the process pipeline. The sampling tube was going directly to the dilution tank of the off-line measurement setup described in Chapter 3.2.4. To be sure that the sample was a good representation of what is inside the pipelines, the sampling tubes were preheated with condensate and a first sample was discarded to achieve isothermal conditions. After the sampling the crystal size distribution was measured.

3.3.2 Steady state measurements
For the measurements of the crystal size distribution in the outlet flow of the DP3 crystallizer the Hüllstrom sensor described in Section 3.2 was used. During the steady state experiments the crystallizer as well as the sensor inputs were kept constant. The conditions used for these experiments are shown in Table 3.1 of Section 3.1. The DP3 crystallizer is an industrial crystallizer and therefore there is a change of demand for product, which results (in slightly) variable inlet and outlet flows of the crystallizer at certain times. The experiments were done for a time period to a maximum of 36 hours.

3.3.3 Dynamic measurements
The same setup and method described in the previous sections is also used for the measurement of process dynamics. According to the theory of crystallisation (Section 2.1) the crystal size and shape depends on the process inputs and the design of the crystallizer. The design of the crystallizer cannot be changed within the scope of this research. Therefore the process inputs of the crystallizer were changed to obtain information to the extent of the dynamics in the crystal size distribution. The theory described that temperature, residence time (crystallizer outlet flow, see Section 3.1) and stirrer speed can influence physical processes, namely growth, secondary nucleation (attrition), agglomeration and breakage. Therefore, those inputs were varied to see the effect on the crystal size distribution. For the external process input the recirculation rate was changed. The recirculation pump rate was changed to alter the recirculation rate and hence the power input. Normally the crystals pass the pump two times every hour, so four times in total. During the measurement crystals passed the pump more or less frequently and were hit by the pump more or less powerful by a change of the pump rate. Therefore, changing the pump rate can change the amount of crystals that will be damaged by the pump. In the experiments the operational and process parameters were altered one at a time from their normal settings to their maximum or minimum allowed settings. The maximum and minimum allowed settings permit to run the crystallizer safely without causing a premature shutdown. In Table 3.3 these values are shown.

Table 3.3: Overview of all process inputs that were changed during the experiments. The changes were from the normal conditions to the maximum or minimum conditions of a parameter. The changes are done separately for all variables. The physical phenomena that are influenced by changing the variable are also mentioned.

Parameter	*Physical phenomena*	*'Normal'*	*'Max'*	*'Min'*	*Unit*
Temperature	Growth, nucleation	60	65	55	°C
Outlet flow (Residence time)	Growth, Attrition, agglomeration	16 (2)	20 (1,4)	10 (3)	m³/h (h)
Stirrer speed	Attrition, agglomeration	35	40	27,5	rpm
Recirculation rate	Breakage, attrition	60	70	30	m³/h

3.4 Model structure

In this section a model structure is developed that describes the dynamic behaviour of the crystal size distribution for the crystallization of adipic acid. The model is tested and validated with the experimental results done with the Hüllstrom sensor. The model structure described in this section is developed by adapting the PBE for continuous crystallization processes. Kinetic relations describing the rate of physical phenomena, like agglomeration, growth and nucleation, are coupled to the PBE. Finally, the concentration balance is derived and also coupled to the PBE.

3.4.1 Population Balance Equation

The population balance equation derived by Ramkrishna (1985) and described in Section 2.3.1 is used as a start. For the modelling the assumption is made that agglomeration and stiff nucleation are the two main physical phenomena. Therefore only those two phenomena will be taken into account for the PBE. The use of stiff nucleation means that the secondary nucleation term disappears from the PBE. Also, the assumption is made that no classification occurs at the outlet flow of the crystallizer. That means that the crystal size distribution in the crystallizer is the same as the crystal size distribution in the outlet flow of the crystallizer. A part of this flow is recirculated back to the crystallizer. The crystal stream will pass a pump and a heat exchanger. For the modelling the assumption is made that the influence of the pump and heat exchanger on the crystal size distribution can be neglected. Experiments need to proof if these assumptions are correct.

To couple agglomeration to the PBE the PBE will be multiplied by the characteristic length (*L*) as described by Qamar and Warnecke (2007a). The adopted PBE is shown in equation 3.1.

$$\frac{\partial f(t,L)}{\partial t} + L\frac{\partial\left[G(t,L)n(t,L)\right]}{\partial L} = \frac{\dot{V}_{rec}}{V} f(t,L) - \frac{\dot{V}_{out}}{V} f(t,L) + \tilde{Q}_{agg}(t,L,f) \quad [3.1]$$

$$\text{where } f(t,L) = n(t,L)\cdot L \text{ and } \tilde{Q}_{agg}(t,L,f) = Q_{agg}(t,L,n)\cdot L$$

The multiplication rule, shown in equation 3.2, can be applied for the convection term.

$$L\frac{\partial\left[G(t,L)n(t,L)\right]}{\partial L} + G(t,L)n(t,L) = \frac{\partial\left[G(t,L)f(t,L)\right]}{\partial L} \quad [3.2]$$

Combining equation 3.1 and 3.2 will give the adopted PBE as shown in equation 3.3.

$$\frac{\partial f(t,L)}{\partial t} = G(t,L)\frac{f(t,L)}{L} - \frac{\partial\left[G(t,L)f(t,L)\right]}{\partial L} + \frac{\dot{V}_{rec}}{V} f(t,L) - \frac{\dot{V}_{out}}{V} f(t,L) + \tilde{Q}_{agg}(t,L,f) \quad [3.3]$$

with as initial condition $n(0,L)\cdot L = f(0,L) = f_0(L)$ and the boundary conditions as described in Section 2.3.3.

Agglomeration

The source and sink terms due to agglomeration are described by Qamar and Warnecke (2007a) but derived earlier by Saffman (1956). The formula for agglomeration is shown in equation 3.4.

$$Q_{agg}(t,x,n) = \frac{1}{2}\int_{x_{\min}}^{x} \beta_{agg}\left(x-x',x'\right) n\left(t,x-x'\right) n\left(t,x'\right) dx' - n(t,x)\int_{x_{\min}}^{x_{\max}} \beta_{agg}\left(x,x'\right) n\left(t,x'\right) dx' \quad [3.4]$$

where the first part of the right hand side (r.h.s.) represents the source term and the second part of the r.h.s. the sink term. The variable *x´* denotes a crystal of volume *x'*. This crystal agglomerates with another crystal with the volume *x-x´* to form a new particle of volume *x*. The variable β_{agg} symbolizes the agglomeration kernel, which is a measure for the agglomeration rate of two crystals. The agglomeration kernel is size depending, non-negative and symmetric.

$$0 \le \beta_{agg}\left(x-x',x'\right) = \beta_{agg}\left(x',x-x'\right) \quad [3.5]$$

Filbet and Laurençot (2004) rewrote the agglomeration term after multiplying the term by the characteristic volume of the crystal.

$$xQ_{agg} = -\frac{\partial F(t,x)}{\partial x} \quad [3.6]$$

$$\text{where } F(t,x) = -\int_0^x \int_{x-u}^{\infty} u\beta(t,u,v)\, f(t,u)\, f(t,v)\, dv du \quad [3.7]$$

The volume based agglomeration term (equation 3.6) and the length based PBE (equation 3.3) can be coupled with equation 3.8.

$$\tilde{Q}_{agg}(t,x,f) = xQ_{agg}(t,x,f) = LQ_{agg}(t,L,f) = \tilde{Q}_{agg}(t,L,f) \quad [3.8]$$

$$\text{where } x = k_v L^3$$

Discretized PBE

For the numerical solution the finite volume method with high resolution scheme is used as described by Qamar and Warnecke (2007a) and described in Section 2.3.2. The discretized population balance equation is shown below. The boundary conditions for PBE are described by Qamar et al. (2007) and are also shown below.

$$\frac{\partial f_i}{\partial t} = \underbrace{\frac{G_i f_i}{L_i} - \frac{1}{\Delta L}\left[(Gf)_{i+1/2} - (Gf)_{i-1/2}\right]}_{\text{Growth of crystals}} + \underbrace{\frac{\dot{V}_{rec}}{V} f_{in,i} - \frac{\dot{V}_{out}}{V} f_{out,i}}_{\text{In and out flow of crystals}} - \underbrace{\frac{1}{\Delta x}\left[F_{i+1/2} - F_{i-1/2}\right]}_{\text{Agglomeration of crystals}}$$

$$\text{with } (Gf)_{1/2} = B_0 L_1 \quad [3.9]$$

$$(Gf)_{1\frac{1}{2}} = G_{1\frac{1}{2}}\left(\frac{(2\Delta L_{1\frac{1}{2}} - \Delta L_1) f_1 + \Delta L_1 f_2}{2\Delta L_{1\frac{1}{2}}}\right) \quad [3.10]$$

$$(Gf)_{N+1/2} = G_{N+1/2}\left(f_N + \frac{\Delta L_N}{2\Delta L_{N-1/2}}(f_N - f_{N-1})\right) \quad [3.11]$$

and for the agglomeration rate $F_{1/2} = 0$ and $F_{N+1/2} = 0$.

As an initial condition a crystal fraction of 2.5 wt-% is taken with a log normal size distribution with an average crystal size of 100µm and standard deviation of 1.5.

Grid mesh

A geometric grid mesh is used for discretizing the length domain of the PBE. The geometric grid mesh is defined as described in Qamar and Warnecke (2007a). The formula for the length of the grids is shown in equation 3.12.

$$L_{i+½} = L_{\min} + 2^{(i-N)/q}\left(L_{\max} - L_{\min}\right) \qquad [3.12]$$

for *i* is 1, 2, ..., *N*.

where L_{min} is equal to zero and L_{max} is 2500µm. *N* represents the total number of nodes, *i* denotes the number of the grids and *q* denotes the degree of the geometric grid.

3.4.2 Kinetic relations

In the literature different relations are used to describe the kinetics of the physical phenomena. In Appendix 3 a number of relations that are used to describe the kinetics for adipic acid are shown. The main difference between the relations is how mechanistic the relations are. For the modelling done in this section the simpler empirical relations are chosen over the more mechanistic but also more complex relations.

Growth rate

The relation used by Gahn and Mersmann (1999, Appendix 3.2) is a mechanistic relation to describe a size dependent growth rate. In the modelling an empirical size independent relation shown in equation 3.13 is used.

$$G = a_1\left(\frac{C - C_{sat}}{C_{sat}}\right)^{a_2} \qquad [3.13]$$

where *C* is the mass fraction of the crystallizing solute and C_{sat} the saturated mass fraction of the crystallizing solute. The parameters in the growth rate expression needs to be estimated. As an initial condition for the saturation concentration 15 wt-% is taken according to the solubility diagram of adipic acid at 60 °C. The actual concentration in the crystallizer need to be calculated with the concentration balance equation.

Agglomeration rate

To solve the agglomeration term of the model the agglomeration flux needs to be discretized and a kinetic expression for the agglomeration kernel needs to be defined. Filbet and Laurençot (2004) discretized the agglomeration flux, *F(t,x)*, that is described in Section 3.4.1. The expression is adapted for the situation that the PBE is a function of length instead of volume. The discretized expression for *F(t,x)* is shown in equation 3.14.

$$F_{i+½} = \sum_{k=0}^{i} \Delta x_k f_k \left\{ \sum_{j=\alpha_{i,k}}^{N} f_j \int_{x_{j-½}}^{x_{j+½}} \frac{\beta\left(x', x_k\right)}{x'} dx' + f_{\alpha_{i,k}-1} \int_{x_{i+½}-x_k}^{x_{\alpha_{i,k}-½}} \frac{\beta\left(x', x_k\right)}{x'} dx' \right\} \qquad [3.14]$$

with $x_{i+½}(t) - x_k(t) \in \Omega_{\alpha_{i,k}-1}(t) = \left[x_{\alpha_{i,k}-1½}, x_{\alpha_{i,k}-½}\right]$ and $x_i = k_v L_i^3$.

The expression of Riemann and Gerstlauer (2003, see Appendix 3.3) for the agglomeration kernel is the most mechanistic relation available in literature. The expression is size dependent; smaller crystals will agglomerate faster with large crystals then crystals of the same size. The expression is complex and therefore in this report a constant agglomeration kernel is used. The experimental results are used to estimate the value of the agglomeration kernel.

Secondary nucleation

The model developed by Gahn (1997, Appendix 3.2) for attrition is based on a lot of different physical parameters, physical relations and design parameters, like crystal hardness and stirrer blade angle. For adipic acid not all the physical parameters required by the model of Gahn are available in literature. Also, the design parameters of the stirrer are not known, which is due to its unique and atypical design as well due to changes done to the stirrer in the last decade. Therefore, an empirical stiff secondary nucleation expression is used. The empirical relation is shown in equation 3.15. The stiff secondary nucleation rate appears in the boundary condition for the PBE as shown in equation 3.9.

$$B_0 = a_1 \sum_{i=a_2}^{N} f_i(t,L) L_i^2 \Delta L_i \qquad [3.15]$$

The experimental results are also used to estimate the parameters a_1 and a_2 of the nucleation rate.

3.4.3 Concentration, mass and energy balance

To calculate the supersaturation the actual concentration in the crystallizer is required. To check the correctness of the PBE the mass balance can be used. Therefore the concentration, mass and energy balances are the backbone of the model. For the mass and energy balance the following equation holds:

$$Accumulation = In - Out + Production \qquad [3.16]$$

The concentration balance is derived in Appendix 4 and shown in equation 3.17.

$$\varepsilon\rho_l \frac{dC}{dt} = \frac{\dot{Q}_{in}}{V}\rho_{in}C_{in} + \frac{\dot{Q}_{rec}}{V}\rho_l C - \frac{\dot{Q}_{out}}{V}\rho_l C - (\rho_c - C\rho_l)\left(3k_v\int_0^\infty GfLdL + k_v\int_0^\infty \tilde{Q}_{agg}L^2 dL\right) \qquad [3.17]$$

where ε denotes the liquid fraction in the crystallizer, ρ_l and ρ_c denotes the density for the liquid and the crystals, respectively and C denotes the concentration in the crystallizer (in weight percent, wt-%). The concentration change is influenced by the properties of the in and out going streams (flow rate, Q, concentration and density). The last term of the r.h.s. of equation 3.17 is the concentration difference due to growth and agglomeration of crystals. The inlet concentration of the crystallizer is 40 wt-% adipic acid solution at a temperature of 80 °C.

The mass balance is derived in the same way as the concentration balance (equation 3.18). In the mass balance an extra term appears, which is the amount of solvent that is evaporated in the crystallizer. The dependency of the liquid fraction disappears in the mass balance.

$$\frac{\dot{Q}_v}{V}\rho_v = \frac{\dot{Q}_{in}}{V}\rho_{in} + \frac{\dot{Q}_{rec}}{V}\rho_l - \frac{\dot{Q}_{out}}{V}\rho_l - (\rho_c - C\rho_l)\left(3k_v\int_0^\infty GfLdL + k_v\int_0^\infty \tilde{Q}_{agg}L^2 dL\right) \qquad [3.18]$$

Finally, the energy balance is established. 60 °C is used as reference temperature for the energy balance to mimic the actual temperature inside the crystallizer. With the energy balance in place the evaporation rate of the solvent can be calculated. The energy balance is shown in equation 3.19.

$$\frac{\dot{Q}_v\rho_v}{V} = \frac{1}{H_v}\left(\frac{\dot{Q}_{in}}{V}\rho_{in}c_{p,l}(T_{in} - T) + \frac{\dot{Q}_{rec}}{V}(T_{rec} - T)\left(\varepsilon\rho_l c_{p,l} + (1-\varepsilon)\rho_c c_{p,c}\right) + 3\frac{H_c}{V}\int_0^\infty k_v GLfdL\right) \qquad [3.19]$$

3.4.4 Implementation

The model is developed stepwise. The model was implemented in MATLAB and a solver (Runge Kutta method, ODE45) was used to solve the system of ODE´s. The numerical cases of Qamar and Warnecke (2007a and b) were used to implement and test the different model parts. The parts

growth, secondary nucleation and agglomeration were added separately and compared with the analytical solution and the numerical solution of Qamar and Warnecke (2007a and b). For all these cases the growth rate, agglomeration kernel and secondary nucleation rate were kept constant. The initial crystal size distribution was also given by the publication. The concentration balance was not used here because the supersaturation is not used in the kinetic relations. In the second part the experimental results and process conditions during the experiments were used for modelling purposes. The process conditions were the initial values used for modelling. The experimental results were used for parameter estimation. The simulations were done to reproduce the mean crystal size.

3.5 Overview of Experimental work

Finally, an overview of the experimental work that was done:

- On-line-off-line experiments to validate the outcome of the measurements.
- Rotating sensor experiments to find the optimal direction of the sampling slit.
- Steady state experiments for proof-of-concept experiments and to become familiar with the Hüllstrom sensor.
- 24-hour experiments to proof the long-term stability of the sensor.
- Short-term changes of process inputs to obtain information about the dynamics of the crystallization process.
- Reproduce literature cases to validate the numerical solution method.
- Reproduce experimental results with a numerical solution of the PBE.

4. Results and Discussion

This chapter on results and discussions is divided into two parts. In the first part the experimental results obtained during plant trials with the Hüllstrom sensor including the validation experiments are presented and discussed. In the second part of this chapter the development of the model is evaluated. Furthermore, the final model structure is assessed for the simulation of experimental results.

4.1 Validation experiments

There were two experiments performed to validate the results of the measurement with the Hüllstrom sensor. In the first experiment the sensor was rotated to see the effect the CSD and in the second experiment an on-line and off-line measurement was compared.

4.1.1 Rotation of the sensor

The experiment was done as described in Section 3.3.1. The operation parameters of the process were kept constant (see Appendix 5). Figure 4.1 shows the results of the experiment (see Section 3.2.4 for data preparation).

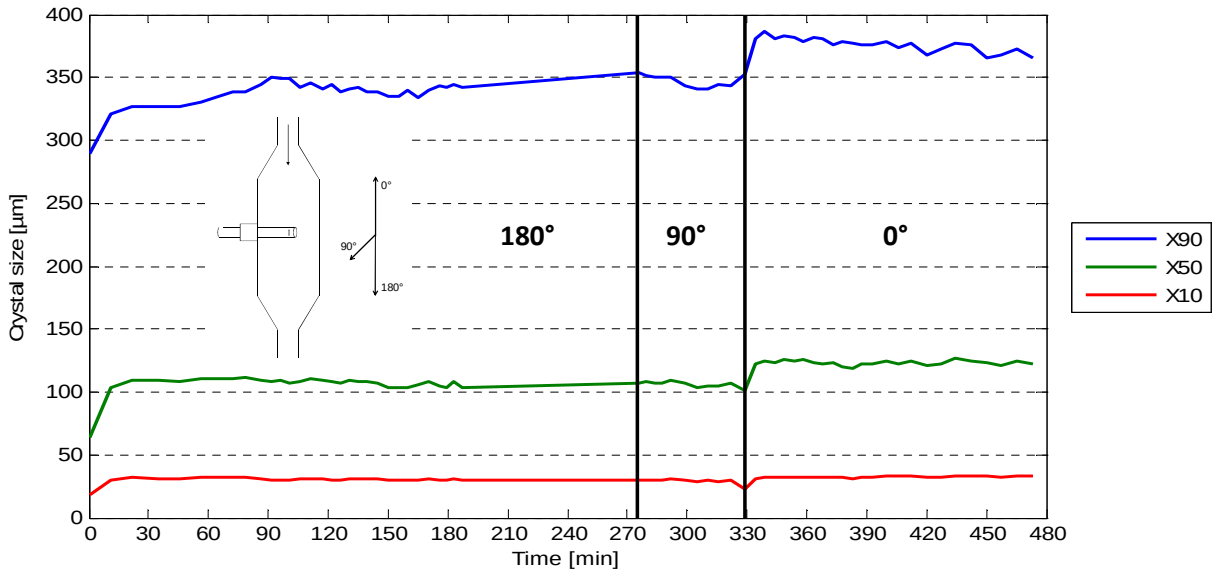

Figure 4.1: Sensor rotation: Values of x_{10}, x_{50} and x_{90} versus time. After 275 minutes the sensor was rotated from 180° to 90° and after 329 minutes the sensor was rotated from 90° to 0°.

Initially, the measured crystal sizes were smaller, but stabilized after about 20 minutes into the measurement. The explanation for this phenomenon is that the sensor needs some time to stabilize to measure the CSD accurately. When the sensor is rotated from the 180 °C to the 90° position the CSD is stable, i.e. there is no appreciable change in particle size upon rotation of the sensor (less than 3% variation). An obvious change in particle size was measured when the sensor was turned to the 0° position. Here the crystal sizes increased as much as 25% (x_{50}).

An explanation for the apparent crystal size increase upon rotation of the sensor to the 0° position is that the sampling slit is now directly facing the flow of the product stream. Therefore the sample that is taken is not isokinetic (Neumann, 2001). The sample slit direction allows for the product stream to be pushed into the sampling slit rather than being accurately pumped into the sensor. Due to their larger mass the bigger crystals follow their natural flow pattern straight downwards and directly into the sampling slit. Smaller crystals on the other hand are more likely to move with the bulk liquid around the sensor head. This causes a classification of the product sample in favour of the larger

crystals. Based on these findings the sensor should not be rotated to the 0° position when measurements are performed.

4.1.2 On-line-off-line measurement

The setup as described in Chapter 3.2.5 was used to take the off-line sample. The off-line sample was measured with an image analysis setup. Figure 4.2 and 4.3 show a graph of the normalised number distribution and the cumulative number distribution of the off-line measurement and the measurement done with the Hüllstrom sensor.

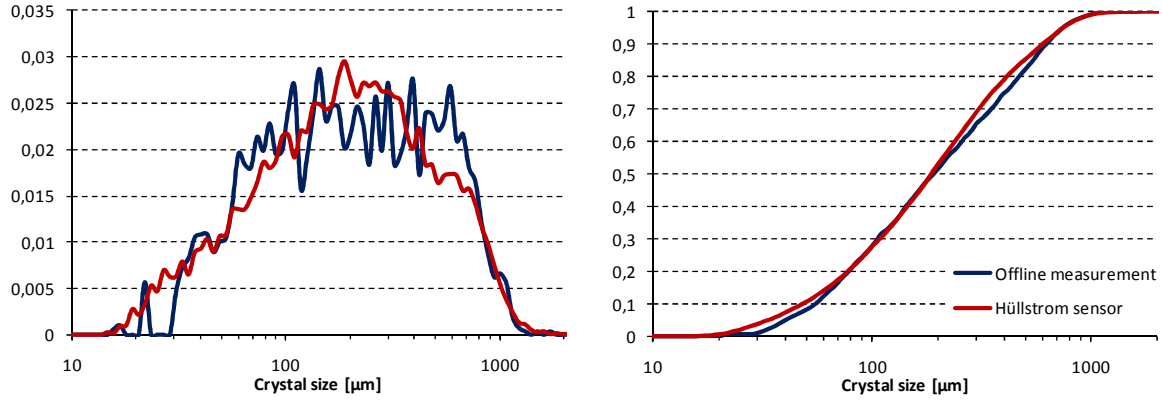

Figure 4.2: Crystal size distribution of the on-line and off-line measurement at 60 °C and 24 m³/h for the recirculation rate. *Left:* Normalized particle number distribution. *Right:* Cumulative number distribution.

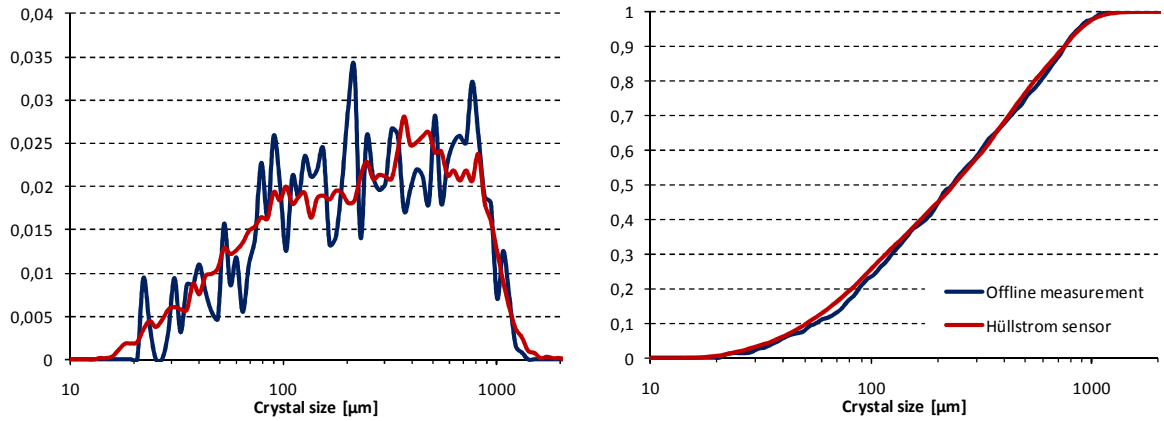

Figure 4.3: Crystal size distribution of the on-line and off-line measurement at 65 °C and 30 m³/h for the recirculation rate. *Left:* Normalized particle number distribution. *Right:* Cumulative number distribution.

Figure 4.2 and 4.3 represent measurements done at different operation conditions, i.e. at 60 °C and 24 m³/h and 65 °C and 30 m³/h, respectively. The particle number distribution shows that the off-line experiments are much more prone to fluctuations. It is reasonable that the fluctuations were due to the extra process steps that were necessary for the off-line measurements, such as sampling, particle concentration dilution and the residence time before the measurement. The cumulative distributions of the off-line measurements are an excellent representation of the on-line measurements. Appendix 5 shows more validation experiments at different operation conditions. Based on these results it can be concluded that the measurements done with the off-line sensor give the same results as the measurements of the Hüllstrom sensor. Therefore it is reasonable to state that the Hüllstrom sensor measures the correct CSD of the outlet flow of the crystallizer.

4.2 Steady state measurements

Here the sensor was used for longer periods of time. The stability of the sensor was tested and the dynamics of the process under steady state conditions were determined. Figure 4.4 shows the trends of the x_{10}, x_{50} and x_{90} for an extended time period.

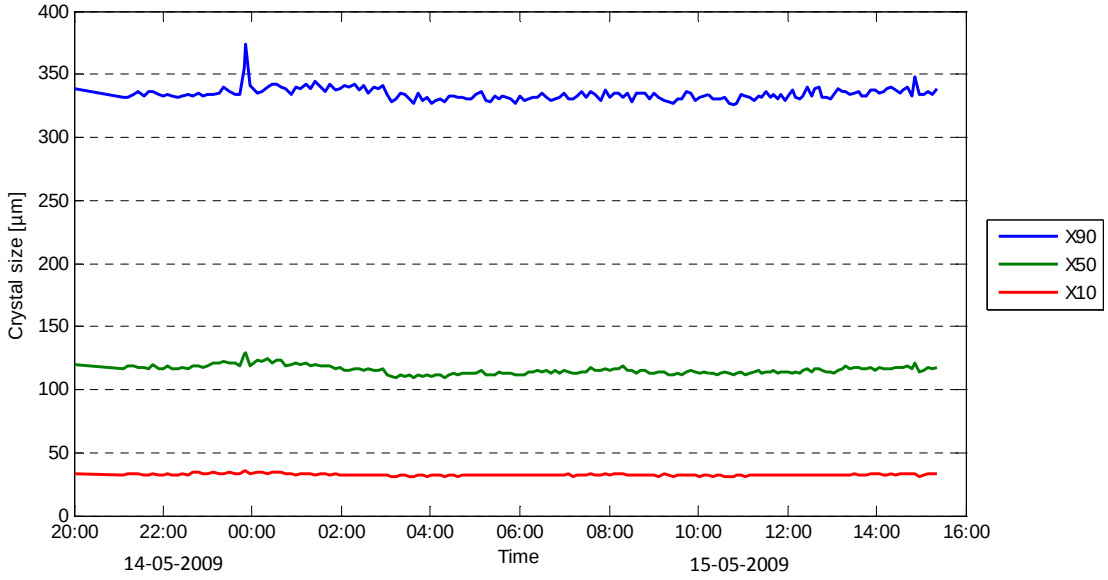

Figure 4.4: Extended time measurements of the x_{10}, x_{50} and x_{90}.

The crystal size distribution was constant with time and hence there were no fluctuations in crystal size. Figure A6.2 of Appendix 6 shows that the experiment was done during a period of time where all the process inputs were kept constant. The inlet and outlet streams of the sensor were constant (Figure A6.1 of Appendix 6), which means that the sampling rate was constant. The frequency of the pump was also constant (Figure A6.1 of Appendix 6). The pump frequency is a measure for the stability of the measurement with the Hüllstrom sensor. A fluctuating pump frequency means accumulation of crystals in the pipelines after the sensor. Which results in fluctuations in the particle concentration on the images and fluctuations in the CSD. The measurements could have continued for quite some time but unfortunately the limited volume of the sheath stream tank required the measurement to be terminated after 19 hours. The results clearly demonstrate that the sensor runs stable for an extended period of time

4.3 Dynamic measurements

Different kind of dynamic measurements were done as described in Section 3.3.3. The process inputs, like residence time, temperature, stirrer speed and recirculation rate were changed separately, i.e. only one parameter was changed at a time. The results of the measurements are shown below.

4.3.1 Residence time

The residence time is a function of the volume and the outlet flow of the crystallizer. The outlet flow of the crystallizer is the most fluctuating process input as the operators manually adapt this input in a defined range to obtain the required amount of product. During the measurement period the demand was changing on a daily basis and therefore a lot of measurements were done at different residence times. A representative value of the x_{10}, x_{50} and x_{90} were taken per day and plotted versus the residence time (see Figure 4.5).

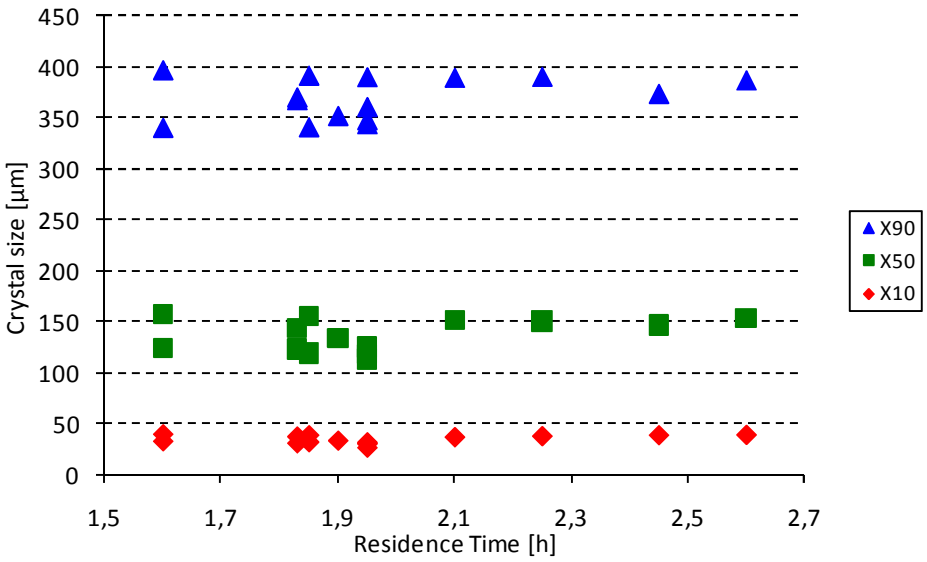

Figure 4.5: The trend of the x_{10}, x_{50} and x_{90} when the residence time changed in the range between 1,6 to 2,6 hours.

The majority of the measurements was done at a residence time of about 1,9 hours. This residence time is the most optimal value to run the process with respect to the entire production process of adipic acid according to the operators. The graph shows a flat trend of the crystal size. That means that the residence time does not have any influence on the crystal size. There are some experiments with a residence time around 1,9 hour that deviates, with a maximum of 15%, of the flat trend.

It is possible that the calculated residence time is not the real residence time. The crystallizer is normally operated for weeks before it is turned off for maintenance purposes due to massive fouling with adipic acid crystals. The crystals are growing on solid-liquid interface on the wall of the crystallizer and therefore reduce the area of evaporation. After a period of time the area between the wall of the crystallizer and the draft tube is fully crystallized and blocked. During this process the volume of the crystallizer is reduced while the level of the crystallizer stays constant. In this case the actual residence time is shorter than the calculated residence time, with an estimated maximum of 10% respectively. Although a change of the residence time will change the results shown in Figure 4.5, it can be concluded that the residence time has almost no influence on the crystal size in the range of 1,6 to 2,6 hours.

4.3.2 Temperature

The crystallizer is operated at 60 °C while the temperature is adjusted by controlling the pressure inside the crystallizer. The temperature was changed to 65 °C and to 55 °C. The measurements were performed on different days and as stated before the crystal size could be different due to unwanted crystallization on the walls of the crystallizer. Therefore only the experiments done on the same day or on two or more consecutive days are compared. Figure 4.6 shows the trend of the crystal size at crystallization temperature of 60 °C and 55 °C.

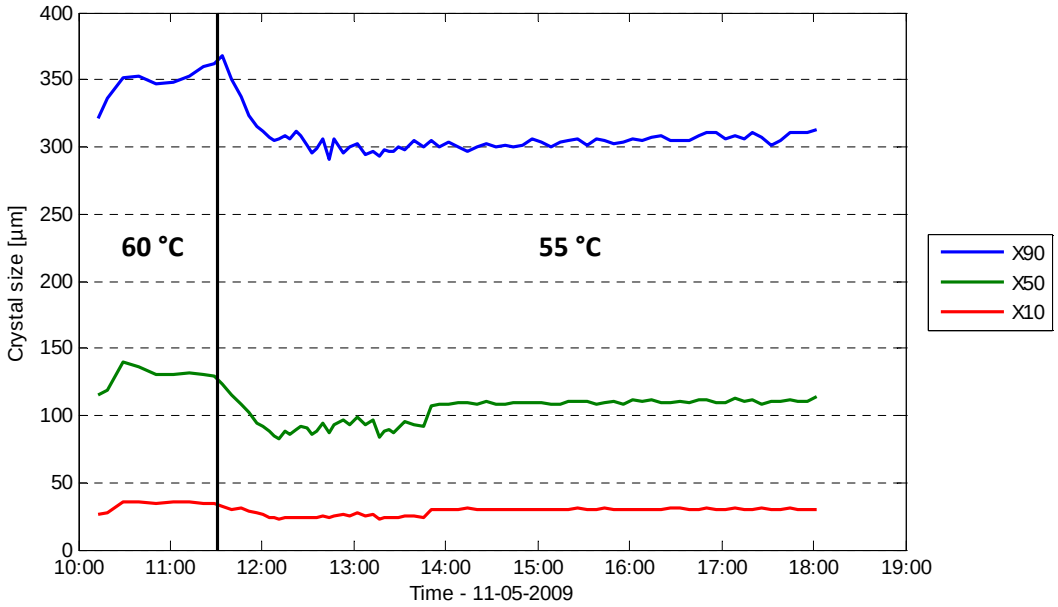

Figure 4.6: The trend of the x_{10}, x_{50} and x_{90} with time at 60 °C and 55 °C (the time of temperature change is indicated by the solid black line).

The first 10 minutes of the measurement the crystal size fluctuates due to the stabilization effect, as mentioned before. At 11:30h the temperature in the crystallizer was changed from 60 °C to 55 °C. The crystal size decreased for approximately 15% and was stable after about 2 hours (±1 residence time). The fluctuations between 12:00h and 14:00h are due to unsuitable settings of the sensor software. The sensor was measuring perfectly under steady state conditions but when there are changes in the number of particles or pressure in the crystallizer the settings of the sensor need to be changed. At this point, the sensor was not able to automatically follow the dynamic behaviour of the crystallizer.

In Figure 4.7 a graph is shown with the average crystal size at steady state conditions at different temperatures and on different days.

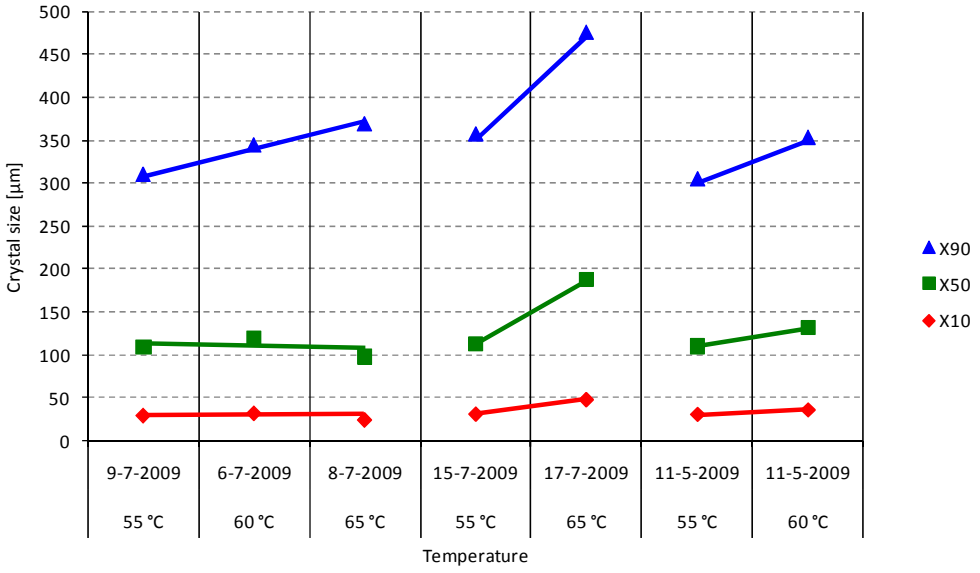

Figure 4.7: The x_{10}, x_{50} and x_{90} at different temperatures and on different days. The x_{10}, x_{50} and x_{90} represent average values over a few hours within the steady state phase. The lines represent the linear trend of different experiments.

The trend lines in Figure 4.7 shows in general an increase in crystal size when the temperature was increased. Only the experiment performed at the 8th of July shows different crystal sizes. The crystal size increases relatively with a maximum of 20% per 5 °C for all crystal sizes (x_{10}, x_{50} and x_{90}).

It was observed that the fluctuations of the CSD as shown between 12:00h and 14:00h in Figure 4.6 are due to a higher concentration of particles in the crystallizer. Unfortunately the crystal concentration could not be measured but an increase of the crystal concentration could be observed by the fluctuation of the pump frequency of the sensor (see Figure A7.2 of Appendix 7). Together with the trend shown in Figure 4.7 it can be concluded that number of crystals increases and the size of the crystals decreases when the temperature was decreased. This effect is probably caused by primary nucleation or an enhanced secondary nucleation rate. The supersaturation at the entrance of the feed in the crystallizer is higher at lower temperatures (see Appendix 1). The entrance of the feed is located directly under the mixer. Primary nucleation will occur when the supersaturation is high and at a higher supersaturation small crystal fragments, occurring due to crystal collisions with the mixer, have a higher chance to grow to real crystals.

4.3.3 Stirrer speed

Several experiments were performed with a different stirrer speed in the range of 24 rpm to 40 rpm. Due to problems with the crystallizer the other process inputs could not be kept constant for all experiments. Figure 4.8 shows the results of the measurement done on the 6th of August. The stirrer speed was changed from 24 rpm to 35 rpm and later even further to 40 rpm.

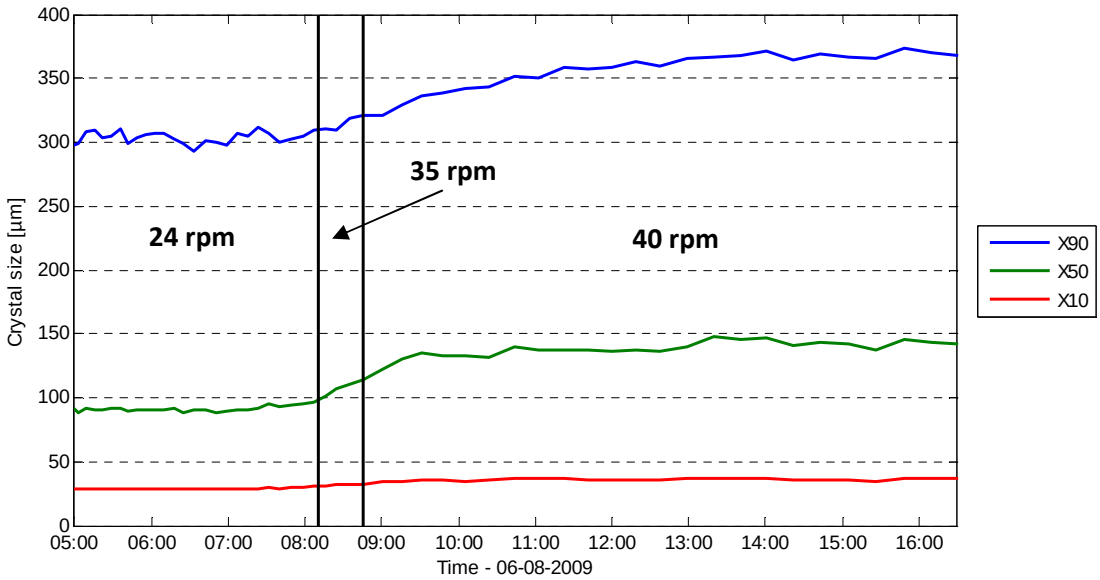

Figure 4.8: The trend of the x_{10}, x_{50} and x_{90} values with time. The stirrer speed was changed from 24 rpm to 35 rpm at 8:10 (first black line) and then to 40 rpm at 8:45 (second black line).

The stirrer speed was changed two times, at 8:10h from 24 rpm to 35 rpm and at 8:45 from 35 rpm to 40 rpm. The other process inputs were kept constant (see Appendix 8). Directly after the change of the stirrer speed the crystal size increased. The x_{50} increased about 50% of the original crystal size. In the contrary, as the stirrer speed was reduced the average crystal size decreased. Two experiments were performed by which the stirrer speed was reduced (see Table 4.1).

Table 4.1: The x_{10}, x_{50} and x_{90} at different stirrer speeds. The listed values were typical crystal sizes at steady state conditions.

Stirrer speed	*Date*	x_{10}	x_{50}	x_{90}	*Unit*
35 rpm	21-07-2009	39.6	143.5	374.7	µm
27 rpm		35.6	125.1	349.9	µm
35 rpm	08-05-2009	32.5	120.5	342.9	µm
27.6 rpm		28.7	98.0	316.9	µm

In both experiments the crystal size decreased with decreasing stirrer speed. The absolute crystal size decrease was almost the same. Table 4.2 gives an overview of the absolute and relative crystal size change of all three experiments.

Table 4.2: Absolute and relative crystal size change of the three stirrer speed experiments. Relative change is based on the crystal size with the slowest stirrer speed.

Date	*from*	*to*	*Δ*	*unit*				*/rpm*			
					x_{10}	x_{50}	x_{90}	x_{10}	x_{50}	x_{90}	*unit*
08-05-2009	35	27.6	7.4	rpm	3.8	22.5	26	0.5	3.0	3.5	µm
					13.2	23	8.2	1.8	3.1	1.1	%
21-07-2009	35	27	8	rpm	4	18.4	24.8	0.5	2.3	3.1	µm
					11.2	14.7	7.1	1.4	1.8	0.9	%
06-08-2009	24	40	16	rpm	7	42	55	0.4	2.6	3.4	µm
					23	44	18	1.4	2.8	1.1	%

The relative and absolute increase for all three experiments are almost the same. There are small deviations for the x_{50} but the x_{10} and x_{90} are almost the same.

The stirrer speed influences the rate of agglomeration and the rate of attrition. Riemann and Gerstlauer (2003) for agglomeration and Gahn (1997) for attrition developed mechanistic kinetic relations based on the stirrer speed. A higher stirrer speed will cause more collisions of the crystals with the stirrer and therefore more attrition. Fortunately, a higher stirrer speed will also cause more crystal-to-crystal collision and hence more agglomeration. The crystal size will normally be smaller due to attrition and larger due to agglomeration. The measurements show that the crystal size increased when the stirrer speed increased. It can be concluded that agglomeration is a more important physical phenomenon in the crystallizer than attrition.

4.3.4 Recirculation rate

The recirculation rate is the operational variable that is situated outside the crystallizer. The recirculation rate was changed from 60 m³/h to 30 m³/h. Figure 4.9 shows the results of two measurements. At time zero the recirculation rate was changed. The other process inputs were kept constant (see Appendix 9).

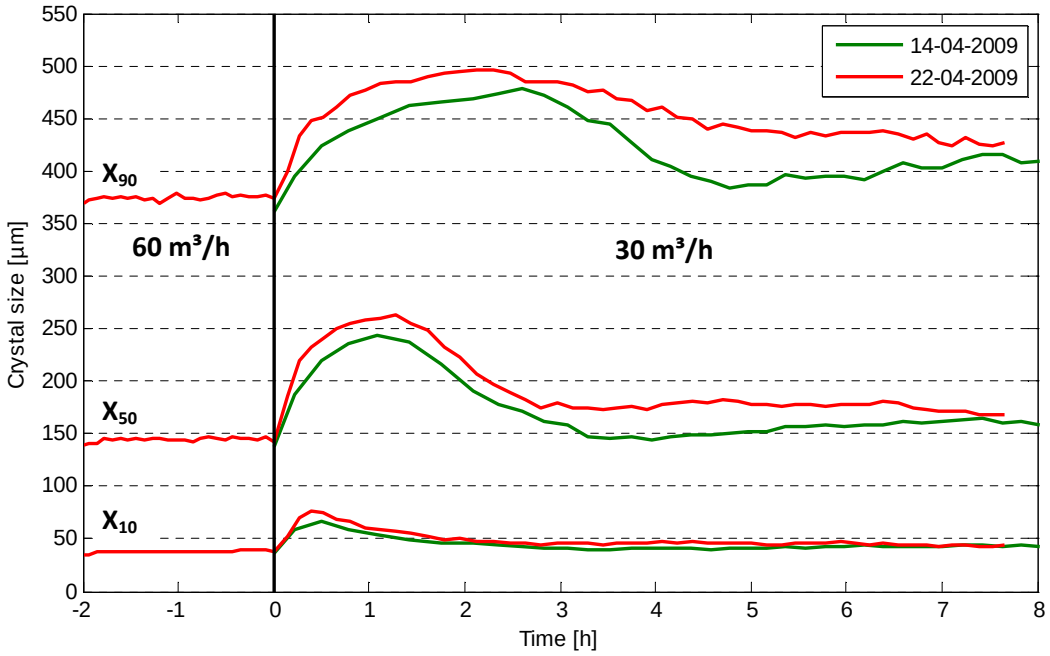

Figure 4.9: The trend of the x_{10}, x_{50} and x_{90} when the recirculation rate is changed from 60m3/h to 30m³/h. At zero the recirculation rate is changed.

The crystal size increased very steeply immediately after the change of the recirculation rate. After a few hours the crystal size stabilized at up to 20% higher values than at the start of the experiments. The sudden increase in crystal size upon the change of the recirculation rate was due to an altered flow pattern especially at the bottom of the crystallizer. The inlet of the recirculation stream is at the bottom of the crystallizer and is operated to prevent sedimentation of crystals at the bottom. Since the bottom of the crystallizer was not mixed as well any more, larger crystals tended to settle and were subsequently preferentially removed from the crystallizer. The reduced recirculation rate will change the flow regime in this area and a new steady state is reached after a few hours.

No other process inputs are coupled to the change of the recirculation rate. Therefore the change in crystal size at the new steady state is most likely due to the pump in the recirculation stream. The pump probably breaks the agglomerated crystals in two or more parts. When the recirculation rate is decreased, the power input of the pump is decreased, hence fewer crystals will pass the pump, and therefore less crystal will be deagglomerated by the pump. It could be concluded that the external recirculation pump has a significant influence on the CSD.

4.4 Modelling results

As described in Section 3.4.4 the model structure that was developed in the experimental work was first tested with literature data. Finally, the model was tested with experimental data from measurements with the Hüllstrom sensor.

4.4.1 Model structure tests

The different cases of Qamar and Warnecke (2007a and 2007b) were used to test the different model parts (see Chapter 3.4.4). In Appendix 10 the numerical results of all the cases are shown. In Figure 4.10 the results of the case with constant growth, exponential nucleation and agglomeration with a constant kernel is shown.

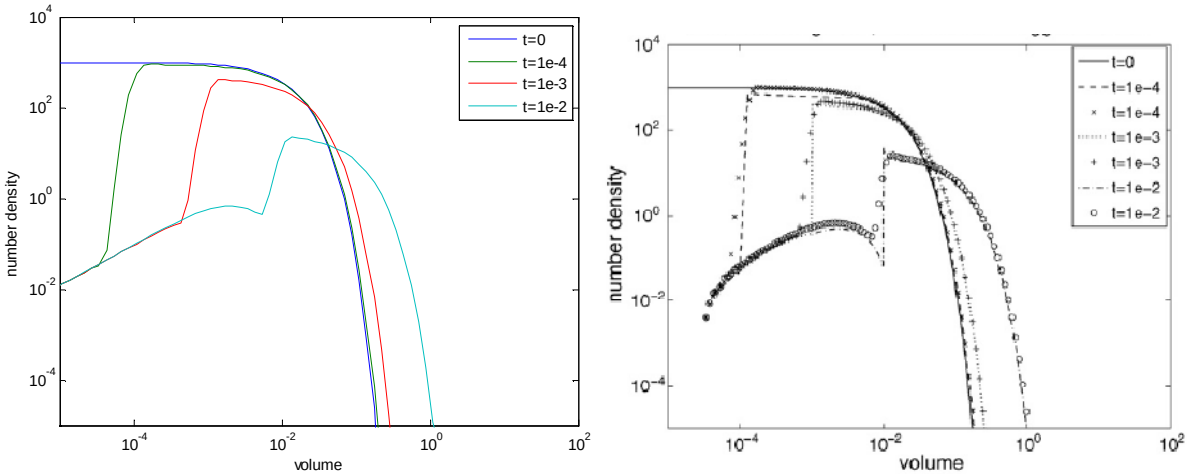

Figure 4.10: *Left:* Numerical solution of a growth, nucleation and aggregation problem with constant growth (G=1), exponential nucleation (B_0=1, $x_{0,n}$=0,001) and a constant kernel (B=100) at different times. Number of grids: 80, q = 3. *Right:* Numerical solution and analytical solution of Qamar and Warnecke (2007a) at different times.

The numerical solution for this problem is in agreement with the numerical solution derived by Qamar and Warnecke (2007a). There is only some numerical diffusion at the left end of the volume domain. This is due to the boundary conditions of the PBE (see Section 2.3.2). These cases are extreme examples to test the limits of the numerical solution. Therefore this will probably not cause problems for the numerical solution of the industrial crystallization process problem.

As described in Section 3.4.2 it is assumed that there will be stiff nucleation, constant growth and agglomeration with a constant kernel. Figure 4.11 shows an simulation of these physical phenomena with constant kinetic parameters.

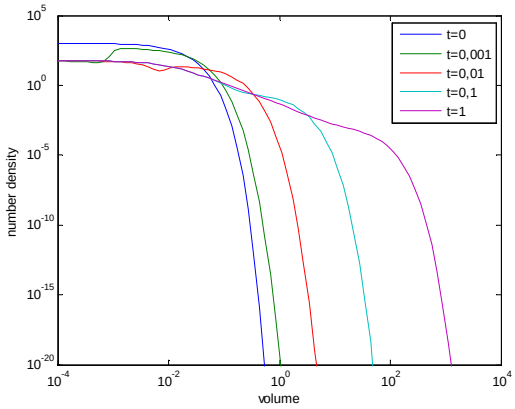

Figure 4.11: Numerical solution of a growth, nucleation and aggregation problem with constant growth (G=1), stiff nucleation (f(1)=1) and a constant kernel (B=100) at different times. Number of grids: 100, q = 3.

Also this solution shows no disruptions and gives a good representation of the physical phenomena that were simulated.

4.4.2 Model validation with experimental data

For the model validation with experimental data the same model structure was used as described in the previous section. Kinetic relations for growth, stiff secondary nucleation and agglomeration were added to the model structure (see section 3.4.2). The relations include the crystallizer temperature and in and out flows but the relations do not include the stirrer speed and the deagglomeration term

of the recirculation rate. Therefore the model structure cannot simulate the trends of the CSD due to a change of the stirrer speed and recirculation rate.

The results of the measurement done on the 20th of April 2009 were used for the parameter estimation and the simulation of the start-up. As an initial condition a crystal fraction of 2.5 wt-% is taken with a log normal size distribution with an average crystal size of 100µm (see Section 3.4.1) and process inputs at the 20th of April were as input for the model. Table 4.3 shows the mean crystal size and the coefficient of variation calculated from the moments of the CSD (shown in Appendix 11).

The simulation results of the mean crystal size and the crystal fraction are shown in Figure 4.12 and table 4.5. For the simulation time 15 hours was taken, because after that time the mean crystal size was constant. The simulation of the CSD, the coefficient of variation and the concentration in the crystallizer are shown in Appendix 11. The parameters that were used are shown in table 4.4.

Table 4.4: The values of the parameters that were taken to simulate the CSD.

Parameter	*Description*	*Value*
a_1	Linear nucleation parameter	0.01
a_2	Lower boundary of integral for nucleation	27
a_3	Linear growth parameter	$1 \cdot 10^{-7}$
a_4	Supersaturation power parameter	0.7
B	Agglomeration kernel	$5.58 \cdot 10^{-15}$

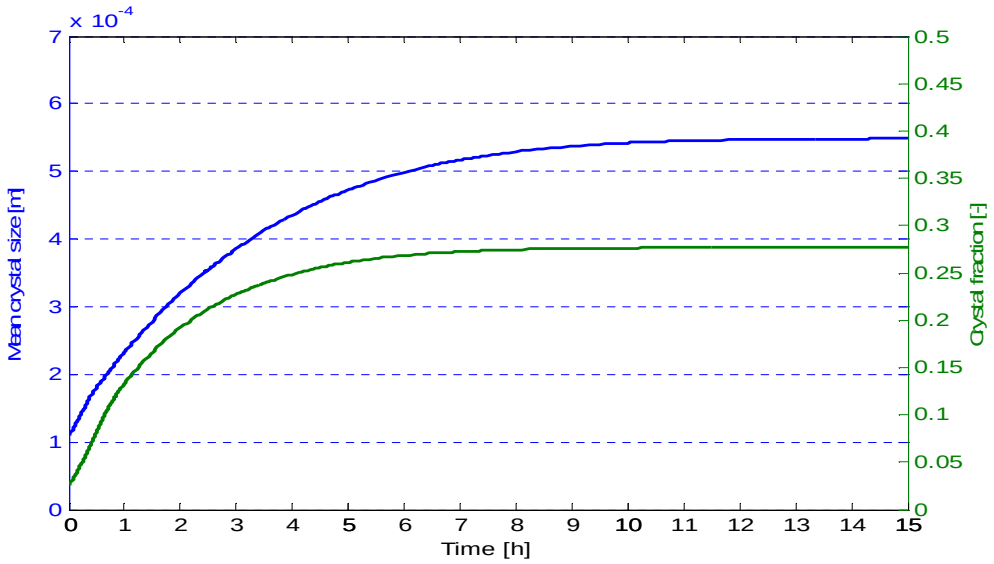

Figure 4.12: The modelled mean crystal size in time and the crystal fraction in time.

Table 4.5: The experimental (on 20-04-2009 at 17:04) and simulation results: the moments, the mean crystal size, coefficient of variation, crystal fraction and calculation time (only for the model).

Parameter	*Experiment*	*Model*	*Unit*
m_0	$1.09 \cdot 10^{-5}$	$1.44 \cdot 10^{12}$	-
m_1	$2.99 \cdot 10^{-9}$	$1.13 \cdot 10^{7}$	m
m_2	$1.12 \cdot 10^{-12}$	$1.39 \cdot 10^{3}$	m^2
m_3	$5.24 \cdot 10^{-16}$	0.503	m^3
m_4	$2.88 \cdot 10^{-19}$	$2.76 \cdot 10^{-4}$	m^4
μ	548.9	548.7	µm
cv	0.613	3,801	-
ε		0.2766	-
t		23.23	s

Figure 4.12 shows the development of the mean crystal size with time and also the crystal fraction in the crystallizer is plotted with time. The simulated mean crystal size is equal to the experimental determined mean crystal size after 14 hours, which were approximately 9 residence times. The modelled crystal fraction is reaching a steady state after 10 hours already. The final crystal fraction in the crystallizer is 28 wt-%. This number cannot be compared with an actual crystal fraction because the crystal fraction was not continuously measured. The calculation time of the software was 23 seconds. The moments were not equal to the moments of the experimental results. This is due to the normalized particle size distribution that is used to calculate the moments for the experimental results.

A second simulation was performed whereby the temperature was changed from 60 °C to 55 °C. Again the data of the experiment of 20th of April is used as input. The temperature was changed after 20 hours of simulation. The results of the simulation for the mean crystal size and crystal fraction are shown in Figure 4.13.

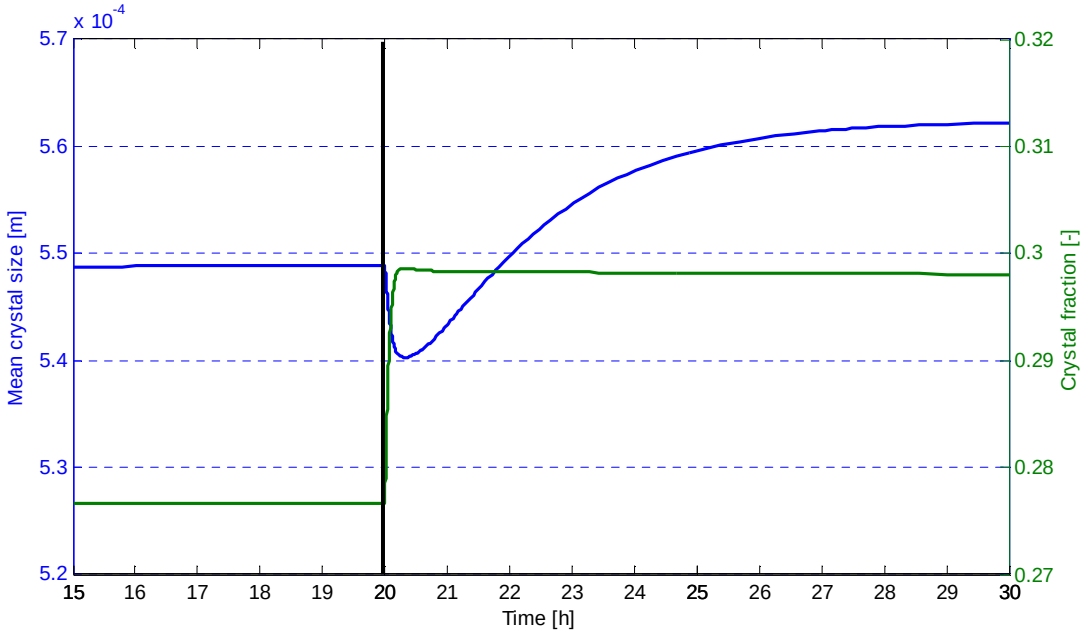

Figure 4.13: The modelled mean crystal size and crystal fraction. The temperature was changed after 20 hours from 60 °C to 55 °C.

The mean crystal size decreased after the change of the temperature but after half a hour the mean crystal size increased to a new steady state with a crystal size larger than at the start. The steady state was reached 9 hours after the temperature was changed. The experimental results showed that after a change of temperature a new steady state was reached within 2 hours. The experimental results also showed a steady state with a smaller crystal size than the initial one. The difference is due to the simple kinetic relation that were applied. According to conclusion of the experimental results the smaller crystal size is due to primary nucleation or enhanced secondary nucleation. Unfortunately primary nucleation was not included in the model and also secondary nucleation is not related to the supersaturation or temperature. Therefore a decrease of the temperature will lead to an increase of the supersaturation and that will lead to an increase of the growth rate. The crystal fraction increased from 27.6 wt-% to 29.8 wt-%. An increase of the crystal concentration was also observed during the experiments at was expected. The crystal fraction could not be compared as stated before.

5. Conclusion

BASF has developed a new type image analysis sensor to measure the CSD on-line in a crystallizer. The sensor uses sheathed streams to dilute the particle concentration of a sample that is taken to measure the CSD. The sensor was used in an industrial crystallizer for the first time. The experimental work of this report started with tests and validation of the measurement results of the sensor. Afterwards the sensor was used to measure the effect of the dynamics of the process inputs on the CSD. The measurements were used for the last part of the research; the validation of a dynamic model. The model structure was developed first and tested with literature examples. Finally the model was validated with the results of the measurements from the sensor. In every phase of the research some conclusions are made. This chapter gives an overview of all conclusions including a general conclusion.

Two experiments were performed to validate the results of the measurements of the sensor. The effect of the direction of the sensor slit on the CSD was studied with the first experiment. The sensor slit was rotated for 180° with regard to the flow direction of the product stream. If the sample slit was in the upwards direction the results deviates from the other rotations. The conclusion was that an isokinetic sample cannot be taken when the sampling slit is in the upwards direction. This conclusion was confirmed with off-line CSD measurements. An isokinetic sample was taken and measured with the same method as the sensor. At different process inputs the CSD shows the same results for the on-line as for the off-line measurement. It was concluded that the sensor with a downwards directed sample slit measures a representative CSD of the outlet flow of the crystallizer.

The sensor was tested on its stability for steady state measurements and dynamic measurements. It was observed that the sensor works perfectly for steady state measurements. Only the first minutes of the measurement the sensor needed to stabilize. Dynamic measurements were more difficult to perform with the sensor. For some dynamic measurements the samples have a different composition (crystal size and particle number) and therefore the frequency of the sensor pump need to be adapted. This could only be done manually and therefore performing dynamic measurements needed more attention. It was concluded that the sensor works perfectly for steady state and dynamic measurements also for longer periods of time.

A series of experiments were performed to study the effect of the variation of the process inputs on the CSD. The process inputs, like residence time, temperature, stirrer speed and recirculation rate, were varied while the sensor measures the CSD. The residence time was different during a large number of experiments. Although the calculated residence time could be different from the actual residence time it could be concluded that the residence time has hardly any influence on the CSD in the measured range of the residence time. The temperature was varied in the range of 55°C to 65°C. Almost all experiments showed that the crystal size increases when the temperature was increased. The relative increase of the crystal size varied to a maximum of 4% per centigrade. It was concluded that an increase of temperature will create more and smaller particles but the relative increase need to be studied more in the future. A set of stirrer speed measurements were performed to study the effect of the stirrer speed on the CSD. Increase in the stirrer speed showed increase the crystal size. The x_{50} of the CSD increased with an average of 3% per rpm. It was concluded that agglomeration is more dominant than attrition for the crystallization of adipic acid. The last process input that was varied was the recirculation rate. The flow of the recirculation stream was reduced from 60 m^3/h to 30 m^3/h. After a huge peak of the crystal size the crystal size stabilize with a maximum of a 20% higher value. The increase of the crystal size was due to the decreased power input of the recirculation pump. The pump breaks the agglomerated crystals into several parts. It was concluded that a decrease of the recirculation rate will increase the deagglomeration rate of crystals.

A dynamic model was developed to study the effect of the process inputs on the different physical phenomena. Physical phenomena, like agglomeration, secondary nucleation and growth, are

influenced by process inputs, like stirrer speed, temperature and residence time. The physical phenomena determine all together the CSD. The population balance equation calculates the dynamics of the crystal size including kinetic relations and mass balances. The rigorous model was solved numerically with a high resolution finite volume scheme. The model structure was tested with different numerical problems from literature. The result of these test simulations were in good agreement with examples from literature. It was concluded that the model structure gives the correct solution for the numerical problems. Simple empirical kinetic relations were added to model the dynamics of the process at hand. With the model a simulation was done to reproduce the CSD in the crystallizer. The parameters of the kinetic relations were estimated to get the best reproduction of the CSD. The simulated mean crystal size was in good agreement with the experiments. The other process variables could not be simulated with the model or validated with the experimental results. It was concluded that the model was working well but the model is only a backbone for the development of a complete dynamic model.

It can be concluded that the aim of this report mainly succeed. The measurement give a nice overview of the dynamics of the crystallizers and the influence of the process inputs on these dynamics. At the other hand a model structure is developed to simulate the dynamics. The model structure is not finished completely. More mechanistic kinetic relations need to be implemented to transform the model structure in a predictive model that can simulate and predict the CSD of the crystallization process of adipic acid.

6. Recommendations

As shown in the previous chapters the measurement results of the sensor are excellent and also the model structure works good. There are some aspects of the sensor that can be improved and also some results of the sensor that can be used for a more intensive analysis. The model structure can be improved to a full dynamic model that reproduce the CSD of the measurements. In this chapter an overview of recommendation for future work is given.

6.1 Sensor

The Hüllstrom sensor is not ready to operate continuously in a crystallizer. The large demand of sheathed streams that is necessary to operate the sensor is the bottleneck of the device. It is recommended to find a source for the sheathed streams in the plant e.g. the mother liquor that comes from the centrifuge. This stream can be used, if necessary after some simple operations, for the sheathed streams in the sensor. Another weakness of the sensor is the dilution method. The tuned dilution rate has no connexion with the actual dilution rate. Therefore the measured crystal concentration cannot be coupled to the crystal concentration in the crystallizer. It is recommended to solve this problem mechanically in the sensor or to install an extra sensor that gives you information about the crystal concentration. The crystal concentration is an important value for the validation of the dynamic model.

The shape information that is measured by the sensor is not analysed in this report. It is recommended to do a study to the influence of the process inputs on the crystal shape. An analysis of the transformation of the shape in a continuous industrial crystallisation process is never done before and therefore it would provide unique information about the shape of the crystals.

The characteristics of the crystals that is measured by the sensor is two dimensional. It would be valuable for future work to have a sensor that gives three dimensional characteristics of the crystals. A sophisticated image analysis sensor that can measure three dimensional crystal characteristics would be an option. A simpler option is to combine the present Hüllstrom sensor with a laser diffraction sensor. The laser diffraction sensor will provide information about the crystal volume and crystal fraction and the Hüllstrom sensor will provide information about the crystal shape. A software package can combine this information to valuable three dimensional crystal characteristics.

6.2 Experiments

The experimental results presented in this report does not give a complete overview of all dynamics in the crystallization process. It is recommended do more measurements with different residence times and temperatures to complete these measurements. In general it is necessary to study the effect of the operational time (after cleaning) on the crystal size. What effect does scaling have on the mixing behaviour in the crystallizer and how does that results in a difference of the crystal size. It is recommended to do set of experiments to study the effect of the operational time of the crystallizer on the CSD.

6.3 Model

The model structure for the crystallization of adipic acid that is presented in this report is the backbone of a complete model. As concluded agglomeration is dominant over attrition. Therefore it is recommended to focus the modelling on agglomeration. The following list of actions are recommendations for the development of the model.

1) Implementing mechanistic kinetic relations for growth and agglomeration (size dependent).
2) Implementing the Gahn model for attrition and secondary nucleation.
3) A parameter estimation study for the different parameters in the kinetic relations.

4) Adding the contribution of the pump and heat exchanger to the model (dissolution and breakage).
5) A classification study and if necessary compartment modelling.
6) Applying the two dimensional population balance equation.

The first four points are logical continuations on the model structure that is developed in this report. The last two points are more difficult developments but very interesting to study.

6.4 Future possibilities

A continuously working on-line sensor that gives you information about the CSD in the crystallizer and a fully working dynamic model that can reproduce and predict the CSD are a powerful combination to improve the control of the crystallizer. Product quality demands of customers can be modelled and so the most optimal process inputs can be set. Also failures in the crystallizer can be detected much sooner with an on-line sensor. Simple or complex control can be applied to the crystallizer. This can save money and energy and the customers will be more satisfied with the adipic acid crystals.

Symbols

Latin symbols

Symbol	*Description*	*Unit*
n	Number density	# m^{-1}
G	Growth rate	m s^{-1}
t	Time	s
L	Characteristic length of a crystal	m
ΔL_i	Length difference of the i^{th} grid	m
V	Volume of crystallizer or crystal	m^3
$\dot{V}$ or $\dot{Q}$	Volume flow	m^3 s^{-1}
Q_{agg}	Agglomeration rate	# m^{-1} s^{-1}
S	Nucleation rate	# m^{-1} s^{-1}
m_i	Moment of the number density function	# m^i
cv	Coefficient of variation	-
r	Upwind ratio of two consecutive solution gradients	-
$F_{\max}$	Maximum Feret diameter	m
$F_{\min}$	Minimum Feret diameter	m
F_{area}	Waddle disc diameter	m
E	Elongation number	-
H	Heywood number	-
$3dD$	3D equivalent diameter	m
x_i	Characteristic length in the distribution where i percent is smaller	m
f	Number density	#
$\tilde{Q}_{agg}$	Agglomeration rate	# s^{-1}
x	Characteristic volume of a crystal	m^3
F	Particle flux due to agglomeration	# m^{-3} s^{-1}
k_v	Shape factor	-
B_0	Nucleation rate	# s^{-1}
q	Degree of the geometric grid	-
C	Concentration of adipic acid	wt-%
H_v	Heat of vaporization	kJ kg^{-1}
H_c	Heat of crystallization	kJ kg^{-1}
T	Temperature	°C
D	Diffusivity	m^2 s^{-1}

Greek symbols

Symbol	*Description*	*Unit*
μ	Mean crystal size	m
Ω_i	Length domain from $L_{i-½}$ to $L_{i+½}$	m
Φ	Flux limiter	-
β_{agg}	Agglomeration kernel	s^{-1}
ρ_i	Density of substance i	kg m^{-3}
ε	Liquid fraction/Crystal fraction	-

Subscripts/Superscripts

Symbol	*Description*
in	Entering the crystallizer
out	Leaving the crystallizer
rec	Recirculation stream
i	Grid number i
N	Number of grids
$\min$	Minimum
$\max$	Maximum
sat	Saturation
l	Liquid
c	Crystal

References

Ankersmid, *EyeTech laser probe / video probe*, information flyer on website, August 2009

BASF, *Löslichkeit ADS-Wasser*, internal BASF research, 2006

Bayer, Gropp, Rauls, M., Rizk, *Concept for producing adipic acid with high flowability*, Report: 102.0564.3Q (2003), BASF SE, Chemicals Research and Engineering, Process Engineering

Bermingham, S.K., *A design procedure and predictive models for solution crystallization processes*, PhD dissertation, Delft University of Technology, Delft University Press, Delft, 2003

Chung, S.H., Ma, D.L. & Braatz, R.D., *Optimal Seeding in Batch Crystallization*, Canadian Journal of Chemical Engineering, volume 77 (1999), issue 3, page 590 – 596

Costa, C.B.B., da Costa, A.C. & Maciel Filho, R., *Mathematical modelling and optimal control strategy development for an adipic acid crystallization process*, Chemical Engineering and Processing, volume 44 (2005), issue 7, page 737 – 753

Cox, H.M., McLachlan, Jr., D., *The use of a schlieren-type microscope in the study of crystal growth*, Journal of Crystal Growth, volume 23 (1974), issue 1, page 71 – 73

David, R., Marchal, P., Klein, J.P., & Villermaux, J., *Crystallization and precipitation engineering – III. A discrete formulation of the agglomeration rate of crystals in a crystallization process*, Chemical Enineering Science, volume 46 (1991), issue 1, page 205 – 213

Filbet, F., and Laurençot, P., *Numerical simulation of the Smoluchowski coagulation equation*, Siam Journal Science Comput., volume 25 (2004), issue 6, page 2004 – 2028

Gahn, C., *Die Festigkeit von Kristallen und ihr Einfluß auf die Kinetik in Suspensionkristallisatoren*, PhD thesis, Technical University of Munich, Herbert Utz Verlag Wissenschaft, München, 1997

Gahn, C., Mersmann, A., *Brittle fracture in crystallization processes Part A and B*, Chemical Engineering Science, volume 54 (1999), issue 9, page 1273 – 1292

Garside, J., *The concept of effectiveness factors in crystal growth*, Chemical Engineering Science, volume 26 (1971), issue 9, page 1425 – 1431

Gerstlauer, A., Motz, S., Mitrovic, A. & Gilles, E.-D., *Development, analysis and validation of population models for continuous and batch crystallizers*, Chemical Engineering Science, volume 57 (2002), issue 20, page 4311 – 4327

Gerstlauer, A., Gahn, C., Zhou, H., Rauls, M. & Schreiber, M., *Application of population balances in the chemical industry – current status and future needs*, Chemical Engineering Science, volume 61 (2006), issue 1, page 205 – 217

Hulbert, H.M., Katz, S., *Some problems in particle technology: A statistical mechanical formulation*, Chemical Engineering Science, volume 19 (1964), issue 8, page 555 – 574

Kruis, F.E., Kusters, K.A., The *collision rate of particle in turbulent flow*, Chemical Engineering Communications, volume 158 (1997), issue 1, page 201 – 230

Marchal, P., David, R., Klein, J.P. & Villermaux, J., *Crystallization and precipitation engineering – I. An efficient method for solving population balance in crystallization with agglomeration*, Chemical Engineering Science, volume 43 (1988), issue 1, page 59 – 67

Mersmann, A., *Crystallization Technology Handbook*, 2nd edition, Marcel Dekker Inc., New York, 2001

Mesbah, A., Kramer, H.J.M., Huesman, A.E.M., Van den Hof, P.M.J., *A control orientated study on the numerical solution of the population balance equation for crystallization processes*, Chemical Engineering Science, 2009, on-line version

Musser, M.T., *Adipic Acid*, Ullmann's Encyclopedia of Industrial Chemistry, John Wiley & Sons, on-line version, last update 30 Oct 2008

Myerson, A.S., *Handbook of Industrial Crystallization*, Butterworth-Heinemann, New York, 1993

Neumann, A.M., *Charactering Industrial Crystallizers of Different Scale and Type*, PhD thesis, Delft University of Technology, Delft University Press, Delft, 2001

Ó Meadhra, R., *Modelling of kinetics of suspension crystallizers*, PhD thesis, Delft University of Technology, Delft University Press, Delft, 1995

Qamar, S., Ashfaq, A., Warnecke, G., Angelov, I., Elsner, M.P., Seidel-Morgenstern, A., *Adaptive high-resolution schemes for multidimensional population balances in crystallization processes*, Computers and Chemical Engineering, volume 31 (2007), issue 10, page 1296 – 1311

Qamar, S. & Warnecke, G., *Numerical solution of population balance equations for nucleation, growth and aggregation processes*, Computers and Chemical Engineering, volume 31 (2007a), issue 12, page 1576 – 1589

Qamar, S. & Warnecke, G., *Solving population balance equations for two-component aggregation by a finite volume scheme*, Chemical Engineering Science, volume 62 (2007b), issue3 , page 679 – 693

Ramkrishna, D., *The status of population balances*, Reviews in Chemical Engineering, volume 3 (1985), page 49 – 95

Randolph, A., and Larson, M.A., *Theory of Particulate Processes*, Academic Press, San Diego, 2nd edition (1988)

Riemann, C. & Gerstlauer, A., *Modelling and simulation of adipic acid crystallization accounting for crystal growth, attrition and agglomeration*, Report: 103.0313.0Q (2003), BASF SE, Chemicals Research and Engineering, Process Engineering

Saffman, P.G., Turner, J.S., *On the collision of drops in turbulent clouds*, Journal of Fluid Mechanics, volume 1 (1956), issue 1, page 16 – 30

Westhoff, G.M., *Design and analysis of suspension crystallizers*, PhD thesis, Delft University of Technology, Delft University Press, Delft, 2002

Zhu, Y., Haut, B., Halloin, V., Delplancke-Ogletree, M.P., *Investigation of crystallization kinetics of sodium bicarbonate in a continuous stirred tank crystallizer*, Journal of Crystal Growth, volume 282 (2005), issues 1 – 2, page 220 – 227

Appendix

Table of contents appendices

Appendix 1: Physical data of adipic acid

Solubility of adipic acid

In 2006 several solubility measurements were done at BASF. All these experiments are stored in an internal database of BASF (BASF, 2006). In Figure A1.1 the experiments are plotted and a calculated average of those experiments is plotted through the data points.
The equation for the calculated average is:

$$y = ae^{bx} \qquad \text{[A1.1]}$$

With *a* being 0,7087 and *b* being 0,0509.

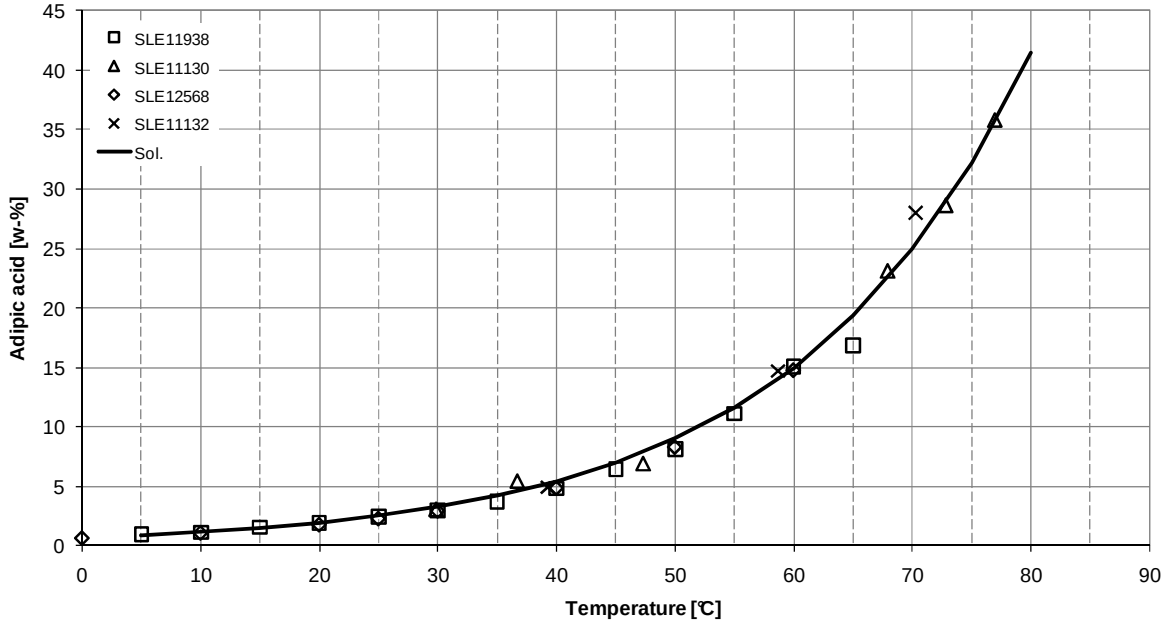

Figure A1.1: The solubility of adipic acid at different temperatures. The solid line is the average of the experiments.

Relations for density and diffusivity

The relation for the density is (Westhoff, 2002):

$$C = c_1 + c_2\rho + c_3\rho^2 + c_4T + c_5T^2 + c_6\rho T \qquad \text{[A1.2]}$$

Where *C* denotes the concentration (g adipic acid / 100g water), *T* denotes the temperature (°C) and *ρ* denotes the density (1000 kg / m³). The *c´*s are the fit parameters as shown in table A1.1.

Table A1.1: Parameters for density function

Parameter	*Value*
c_1	37,8590
c_2	-78,1661
c_3	40,3646
c_4	-0,0678
c_5	$5{,}007\cdot10^{-5}$
c_6	0,0655

The density function is an emperical equation that holds for the temperature range of 55 – 65 °C and for the concentration range of 4,5 – 22,5 g/100 g water.

The relation for the diffusivity is (Westhoff, 2002):

$$D = \left(2.23 + 0.205T\right)10^{-10} \qquad \text{[A1.3]}$$

Where *D* denotes the diffusivity (m²/s) and *T* denotes the temperature (°C). The relation holds for the temperature range of 15 – 60 °C.

Other physical parameters

Other important physical parameters of adipic acid and adipic acid – water solutions are shown in table A1.2 (Westhoff, 2002).

Table A1.2: Physical data of adipic acid and adipic acid – water solutions

Property	*Unit*	*Value*
Molecular formula		$C_6H_{10}O_4$
Molecular weight	g/mol	146,14
Density	kg/m	1344
Specific heat crystal	kJ / kg K	1,59
Heat of fusion	kJ / kg K	115
Entropy of fusion	J / mol K	79,8
Heat of vaporisation	kJ/kg	549
Heat of solution in H_2O	kJ/kg	214
Dissociation constant in H_2O	kJ/kg	
K_1 (@ 50°C)		$3{,}29 \cdot 10^{-5}$
K_2 (@ 50°C)		$3{,}22 \cdot 10^{-5}$
Interfacial energy between solid and water	J/m^2	0,060
Specific heat saturated solution at 50°C	kJ / kg K	4.022

Appendix 2: Sampling and setup for off-line measuring

Off-line measurement setup

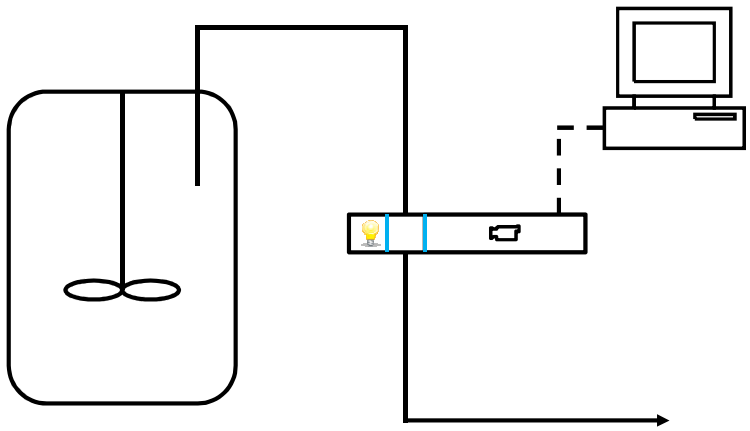

The off-line measurement set-up:
A sample is added to a 30-liter vessel, which is stirred and the temperature is kept the same as in the crystallizer. From the vessel a continuous product stream is pumped through the measuring cell. The cell also contains a light source, a camera and several lenses. The measurement data is analyzed by a computer. The measured crystals are flowing to the drain.

Sampling for off-line measurement

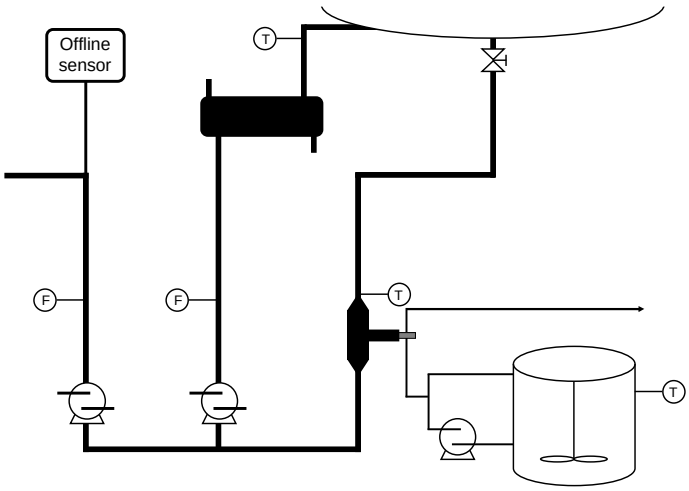

Figure A2.1: The position of the sampling point for the off-line measurements. The sampling is done directly after the product pump to the centrifuge and dryers.

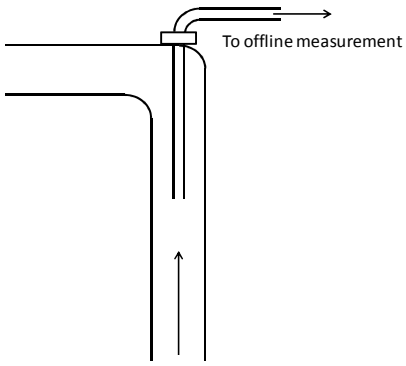

Figure A2.2: For the off-line measurement a tube is installed in the product pipeline for isokinetic sampling.

Appendix 3: Kinetics: Growth rate model, attrition model and agglomeration kernel model

3.1 Growth

The growth rate as used in Gahn and Mersmann (1999) and Mersmann (1994):

$$\frac{G(L)}{2k_d(L)} = \frac{\Delta c_{L,A}}{c_S} + \frac{k_d(L)}{2k_r c_S} - \sqrt{\left(\frac{k_d(L)}{2k_r c_S}\right) + \left(\frac{k_d(L)}{k_r c_S}\right)\frac{\Delta c_{L,A}}{c_S}} \qquad [A3.1]$$

The mass transfer coefficient can be calculated with (Marchal et al., 1988, Mersmann, 1994):

$$k_d(L) = \frac{D_{dif}}{L}\left(2 + 0.8\left[\frac{\varepsilon L^4}{\nu_l^3}\right]^{1/5}\left[\frac{\nu_l}{D_{dif}}\right]^{1/3}\right) \qquad [A3.2]$$

The expression for the real supersaturation is (Mersmann, 1994):

$$\Delta c = -c^*_{real}(L) = c - c^* \exp\left(\frac{\omega_s}{RT}\right) \qquad [A3.3]$$

A size independent empirical relation for the growth rate (Ó Meadhra, 1995):

$$G = a_1\left(\frac{C - C_{sat}}{C_{sat}}\right)^{a_2} \qquad [A3.4]$$

3.2 Attrition

There are a lot of models developed in the past to describe secondary nucleation. Most of these are empirical models and therefore don not have much physical meaning. Gahn (1997) developed a mechanistic model that combines attrition, secondary nucleation and growth. In the literature the models of Gahn (1997) and Gahn and Mersmann (1999) are used to describe these physical processes that occur during crystallization. The models can be used for any attrition event and therefore also for the crystallisation of all kinds of inorganic and organic compounds. The model consist of three fluxes; a negative particle number flux of crystals that collide with the stirrer (*1*), a positive particle number flux for abraded crystals (*2*) and a positive particle number flux for crystal fragments (*3*).

$$S(t,L,n) = -\dot{n}_{at,1}(t,L) + \dot{n}_{at,2}(t,L) + \dot{n}_{at,3}(t,L) \qquad [A3.5]$$

The fluxes are based on the probability of collisions between crystals and the stirrer blades. The parameters are the geometry of the stirrer blades, the speed of the crystals, the stirrer speed and some physical parameters of the crystals.

The empirical kinetic relations for secondary nucleation are easier to implement. Bermingham (2003) evaluates different kind of relations, like the Ottens relation. These relations are in the form of equation A3.6.

$$B_0 = a_1\left(\int_{a_2}^{\infty} n(t,L)\,G(t,L)^{a_3}\,L^{a_4}\,dL\right)^{a_5} \qquad [A3.6]$$

Where a_i (*i=[1 – 4]*) are the parameters depending on stirrer speed, stirrer size, internal fluid velocity, density, supersaturation and survival rate. For some parameters there are physical based relations

but the other parameters need to be estimated. These secondary nucleation relations are stiff nucleation relations, which means that nucleation only takes place at infinite small crystal sizes.

3.2.1 Derivation of the Gahn model

The fluxes for attrition are:

Flux of original crystals

$$\dot{n}^{-}_{at,1}(L) = \beta_{at}(L)\cdot n(L) \qquad \text{[A3.7]}$$

Flux of abraded crystals

$$\dot{n}^{+}_{at,2}(L) = \int_{L}^{L_\infty} \delta\left(L - \left[L'^3 - \frac{V_{p,at}(L')}{k_v} \right]^{1/3} \right) \beta_{at}(L')\cdot n(L')\,dL' \qquad \text{[A3.8]}$$

Flux of fragments

$$\dot{n}^{+}_{at,3}(L) = \int_{L}^{L_\infty} N_{frag}(L')\left[h(L - L_{frag,\min}) - h(L - L_{frag,\max}(L')) \right] \times f_{frag}(L, L')\,\beta_{at}(L')\cdot n(L')\,dL' \qquad \text{[A3.9]}$$

To relate the last two formulas an attrition spectrum is defined to describe a connection between the particles disappearing and appearing in the particle population.

$$P(d_p, d_p') = \frac{N_{frag}(d_p')}{1+N_{frag}(d_p')}\left[h(d_p - d_{p,frag,\min}) - h(d_p - d_{p,frag,\max}(d_p')) \right] f_{frag}(d_p, d_p') + \frac{1}{1+N_{frag}(d_p')}\delta\left(d_p - \left[d_p'^3 - \frac{V_{p,at}(d_p')}{k_v} \right]^{1/3} \right) \qquad \text{[A3.10]}$$

The following normalization condition needs to be applied to guarantee that only N_{frag} crystal fragments and one abraded crystal is produced.

$$\int_0^{d_p'} P(d_p, d_p')\,dd_p = 1 \qquad \text{[A3.11]}$$

Combining the last to equations gives:

$$\frac{N_{frag}(d_p')}{1+N_{frag}(d_p')}\int_0^{d_p'}\left[h(d_p - d_{p,frag,\min}) - h(d_p - d_{p,frag,\max}(d_p')) \right] f_{frag}(d_p, d_p')\,dd_p + \frac{1}{1+N_{frag}(d_p')}\int_0^{d_p'}\delta\left(d_p - \left[d_p'^3 - \frac{V_{p,at}(d_p')}{k_v} \right]^{1/3} \right) dd_p = 1 \qquad \text{[A3.12]}$$

The second integral can be simplified to 1 (the assumption is made that $d_p = d_p'$). So the above equation can be simplified to:

$$\int_0^{d_{p,\infty}}\left[h(d_p - d_{p,frag,\min}) - h(d_p - d_{p,frag,\max}(d_p')) \right] f_{frag}(d_p, d_p')\,dd_p = 1 \qquad \text{[A3.13]}$$

To guarantee mass conservation after attrition the following should hold:

$$\left(1+N_{frag}\left(d_p^{'}\right)\right)\int_0^{d_p^{'}} k_v d_p^3 P\left(d_p, d_p^{'}\right) dd_p^{'} = k_v d_p^{'3} \qquad \text{[A3.14]}$$

If the attrition spectrum is inserted mass conservation can be guaranteed if:

$$V_{p,at}\left(d_p^{'}\right) = N_{frag}\left(d_p^{'}\right)\int_0^{d_p^{'}} k_v d_p^3 \left[h\left(d_p - d_{p,frag,\min}\right) - h\left(d_p - d_{p,frag,\max}\left(d_p^{'}\right)\right)\right] f_{frag}\left(d_p, d_p^{'}\right) dd_p$$

[A3.15]

Gahn and Mersmann (1999) derived physical relationships for the attrition rate, the abraded volume and the distribution of attrition fragments. These relations are necessary to solve the balances.

The attrition rate:

$$\beta_{at}\left(d_p\right) = \frac{\dot{V}_{pump}}{V}\int_0^{d_{stirrer}/2} \eta_{geo}\left(r\right)\eta\left(d_p, r\right) dr \qquad \text{[A3.16]}$$

The abraded volume:

$$V_{p,at}\left(d_p, r\right) = \frac{2}{3}\frac{H_V^{2/3} K_r}{\mu_{shear}\Gamma} E_{kin}\left(d_p, r\right)^{4/3} \qquad \text{[A3.17]}$$

Distribution of attrition fragments:

$$f_{frag}\left(d_p, d_p^{'}, r\right) = \frac{2.25}{d_{p,frag,\min}^{-2,25} - d_{p,frag,\max}^{-2,25}\left(d_p^{'}, r\right)} d_p^{-3.25} \qquad \text{[A3.18]}$$

To calculate the maximum fragment size, the following relation is used:

$$d_{p,frag,\max}\left(d_p^{'}, r\right) = \frac{1}{2}\frac{H_V^{2/9} K_r^{1/3}}{\mu_{shear}^{1/3}\Gamma^{1/3}} E_{kin}\left(d_p^{'}, r\right)^{4/9} \qquad \text{[A3.19]}$$

The minimum fragment size is:

$$d_{p,frag,\min} = \frac{32}{3}\frac{\mu_{shear}\Gamma}{H_V^2 K_r} \qquad \text{[A3.20]}$$

3.3 Agglomeration kernel

David et al. (1991) and Costa et al. (2005) developed kinetic relations for the agglomeration kernel. The relations used in the publications are based on general agglomeration kernel models including phenomenological and fluid mechanical phenomena. The particle concentration, the supersaturation, the power dissipation per unit of mass and the size of the crystallizer and of the crystals are taken into account. Riemann and Gerstlauer (2003) also developed a kinetic relation for the agglomeration kernel, this relation has a better physical meaning. The model contains two major parameters. The first parameter describes the possibility of two crystals colliding, the second parameter describes the possibility of two colliding crystals to agglomerate. The relation of Riemann and Gerstlauer (2003) is based on the particle collision theory of Kruis and Kusters (1997) and takes into account the stirrer speed, the residence time, the density and the crystal size. The derivation of the agglomeration kernel kinetics in Riemann and Gerstlauer (2003) is done below. Some estimations for parameters of the agglomeration and attrition model based on experiments done by Riemann and Gerstlauer (2003) are also given. The result of the derivation of the agglomeration kernel is shown in equation A3.21.

$$\beta_{Agglo}\left(d_P, d_P^{'}\right) = k_{Agglo} \cdot \beta_{Coll}\left(d_P, d_P^{'}\right) \cdot E_{Agglo}\left(d_P, d_P^{'}, k_{eff}\right) \qquad \text{[A3.21]}$$

3.3.1 Probability that particles colliding

Theory from Kruis and Kusters (1997).

$$\beta_{Coll}\left(d_P, d_P^{'}\right)=\left(\frac{8\pi}{3}\right)^{1/2}\left(\frac{d_P+d_P^{'}}{2}\right)\sqrt{3\cdot\overline{\mathbf{w}}_i^2} \quad \text{[A3.22]}$$

Where **w** is the collision velocity vector as derived by Kruis & Kusters (1997).

$$\overline{\mathbf{w}}_i^2=\overline{\mathbf{v}}_f^2(1-b)^2\frac{\gamma}{\gamma-1}\left(\frac{\left(\Theta_{P1}+\Theta_{P2}\right)^2-4\Theta_{P1}\Theta_{P2}\left[\left(1+\Theta_{P1}+\Theta_{P2}\right)/\left(\left(1+\Theta_{P1}\right)\left(1+\Theta_{P2}\right)\right)\right]^{1/2}}{\Theta_{P1}+\Theta_{P2}}\right)$$
$$\times\left(\frac{1}{\left(1+\Theta_{P1}\right)\left(1+\Theta_{P2}\right)}-\frac{1}{\left(1+\gamma\Theta_{P1}\right)\left(1+\gamma\Theta_{P2}\right)}\right) \quad \text{[A3.23]}$$

With the added mass coefficient, *b*:

$$b=\frac{3\rho_f}{2\rho_P+\rho_f} \quad \text{[A3.24]}$$

Correction factor for the movement of small particles, *γ*:

$$\gamma=2\left(\frac{T_L}{\tau_L}\right) \quad \text{[A3.25]}$$

The dimensionless particle relaxation time, Θ_P:

$$\Theta_P=\frac{\tau_P}{T_L} \quad \text{[A3.26]}$$

The integral length can be calculated by:

$$\Lambda=\frac{1}{3}d_{stirrer} \quad \text{[A3.27]}$$

At homogeneous turbulences (C ≈ 2) the average variance of isotropic fluctuation velocity (isotropen Schwankungsgeschwindigkeit) can be calculated as.

$$\overline{\mathbf{v}}_f^2=\overline{\mathbf{u}}_{f,iso}^2=C(\varepsilon\Lambda)^{2/3} \quad \text{[A3.28]}$$

The energy input rate can be calculated as:

$$\varepsilon=\frac{P}{\rho_f V_{crys}} \quad \text{[A3.29]}$$

The Langrange times can be calculated with the variance and the integral length according to.

$$T_L=0.4\frac{\Lambda}{\sqrt{\overline{\mathbf{v}}_f^2}} \text{ and } \tau_L=\left(2\frac{\overline{\mathbf{v}}_f^2}{\varepsilon^{3/2}}\nu_f^{1/2}\right)^{1/2} \quad \text{[A3.30]}$$

And the particle relaxation time (according to Nguyen (2003)).

$$\tau_P=\frac{2\rho_P}{9\nu_f}d_P^2 \quad \text{[A2.31]}$$

3.3.2 Chance of agglomeration

For the agglomerated crystal diameter a special equation is used. In this formula the smaller crystals have a larger influence on the final crystal size.

$$d = 2\frac{d_P \cdot d_P^{'}}{d_P + d_P^{'}} \qquad \text{[A2.32]}$$

With this special diameter the probability of agglomeration can be calculated.

$$E_{Agglo}(d) \approx \exp\left(-k_{eff}\,\frac{d}{\Lambda}\right) \qquad \text{[A2.33]}$$

3.3.3 Agglomeration kernel

The agglomeration kernel can now be calculated with an extra parameter added to fit the model to the experimental results.

$$\beta_{Agglo}\left(d_P, d_P^{'}\right) = k_{Agglo} \cdot \beta_{Coll}\left(d_P, d_P^{'}\right) \cdot E_{Agglo}\left(d_P, d_P^{'}, k_{eff}\right) \qquad \text{[A2.34]}$$

The parameters k_{agglo}, k_{eff} and also k_{at} are gathered with parameter estimation, therefore some experiments are done. From experiments with adipic acid and modelling in PARSIVAL® the following estimations of the parameters were calculated:

k_{agglo}	$3.35 \cdot 10^{-3}$
k_{eff}	$1.05 \cdot 10^{3}$
$k_{at,low}$ ($\varepsilon \approx 1$)	$5.9803 \cdot 10^{-5}$
$k_{at,high}$ ($\varepsilon > 2$)	$1.21 \cdot 10^{-5}$

Appendix 4: Derivation of the concentration, mass and energy balance

The population balance

$$\frac{\partial n}{\partial t}+\frac{\partial Gn}{\partial L}=-\frac{\dot{Q}_{out}}{V}n+\frac{\tilde{Q}_{agg}}{L}+\frac{\tilde{S}}{L} \qquad \text{[A4.1]}$$

Multiplied by $k_v L^3$:

$$\int_0^\infty \frac{\partial n}{\partial t}k_v L^3 dL+\int_0^\infty \frac{\partial Gn}{\partial L}k_v L^3 dL=-\frac{\dot{Q}_{out}}{V}\int_0^\infty nk_v L^3 dL+\int_0^\infty \tilde{Q}_{agg}k_v L^2 dL+\int_0^\infty \tilde{S}k_v L^2 dL \qquad \text{[A4.2]}$$

Defining the voidage factor, $\varepsilon=1-k_v m_3$, and substitute:

$$-\frac{\partial \varepsilon}{\partial t}=3k_v\int_0^\infty GnL^2 dL-\frac{\dot{Q}_{out}}{V}(1-\varepsilon)+k_v\int_0^\infty \tilde{Q}_{agg}L^2 dL+k_v\int_0^\infty \tilde{S}L^2 dL \qquad \text{[A4.3]}$$

The concentration balance

$$V\frac{d}{dt}\left(\varepsilon C\rho_l+(1-\varepsilon)\rho_c\right)=\dot{Q}_{in}\rho_{in}C_{in}-\dot{Q}_{out}\left(\varepsilon C\rho_l+(1-\varepsilon)\rho_c\right) \qquad \text{[A4.4]}$$

The partial differential equation at the l.h.s. can be worked out:

$$V\frac{d}{dt}\left(\varepsilon C\rho_l+(1-\varepsilon)\rho_c\right)=V\left(\varepsilon\rho_l\frac{dC}{dt}-(\rho_c-\rho_l C)\frac{d\varepsilon}{dt}\right) \qquad \text{[A4.5]}$$

$$\varepsilon\rho_l\frac{dC}{dt}-(\rho_c-\rho_l C)\frac{d\varepsilon}{dt}=\frac{\dot{Q}_{in}}{V}\rho_{in}C_{in}-\frac{\dot{Q}_{out}}{V}\left(\varepsilon\rho_l C+(1-\varepsilon)\rho_c\right) \qquad \text{[A4.6]}$$

The population balance (eq. A4.3) and the concentration balance (eq. A4.6) can be combined:

$$\varepsilon\rho_l\frac{dC}{dt}=-(\rho_c-\rho_l C)\left(3k_v\int_0^\infty GnL^2 dL-\frac{\dot{Q}_{out}}{V}(1-\varepsilon)+k_v\int_0^\infty \tilde{Q}_{agg}L^2 dL+k_v\int_0^\infty \tilde{S}L^2 dL\right)+ \qquad \text{[A4.7]}$$
$$\frac{\dot{Q}_{in}}{V}\rho_{in}C_{in}-\frac{\dot{Q}_{out}}{V}\left(\varepsilon\rho_l C+(1-\varepsilon)\rho_c\right)$$

The final concentration balance is:

$$\varepsilon\rho_l\frac{dC}{dt}=\frac{\dot{Q}_{in}}{V}\rho_{in}C_{in}+-\frac{\dot{Q}_{out}}{V}\rho_l C-(\rho_c-C\rho_l)\left(3k_v\int_0^\infty GnL^2 dL+k_v\int_0^\infty \tilde{Q}_{agg}L^2 dL+k_v\int_0^\infty \tilde{S}L^2 dL\right) \qquad \text{[A4.8]}$$

The energy balance

Reference temperature is 60°C:

$$\frac{dE}{dt}=\dot{Q}_{in}\rho_{in}c_{p,l}(T_{in}-T)-\dot{Q}_v\rho_v H_v+\hat{S}H_c \qquad \text{[A4.9]}$$

For the case that a second feed stream contains crystals. The energy balance change to equation A4.10.

$$\frac{dE}{dt}=\dot{Q}_{in}\rho_{in}c_{p,l}(T_{in}-T)+\dot{Q}_{rec}(T_{rec}-T)\left(\varepsilon\rho_l c_{p,l}+(1-\varepsilon)\rho_c c_{p,c}\right)-\dot{Q}_v\rho_v H_v+\hat{S}H_c \qquad \text{[A4.10]}$$

Energy accumulation is zero, because temperature in crystallizer is constant. $\hat{S}$ is the amount of new crystals formed per second. Assumed that agglomeration and nucleation will not consume or produce energy.

$$\hat{S} = 3\int_0^\infty k_v GLf dL \qquad \text{[A4.11]}$$

The final energy balance is:

$$\frac{\dot{Q}_v \rho_v}{V} = \frac{1}{H_v}\left(\frac{\dot{Q}_{in}}{V}\rho_{in} c_{p,l}\left(T_{in} - T\right) + \frac{\dot{Q}_{rec}}{V}\left(T_{rec} - T\right)\left(\varepsilon\rho_l c_{p,l} + \left(1-\varepsilon\right)\rho_c c_{p,c}\right) + 3\frac{H_c}{V}\int_0^\infty k_v GLf dL \right)$$

[A4.12]

The mass balance

For the mass balance the same assumptions hold as for the concentration balance.

$$V\frac{d}{dt}\left(\varepsilon\rho_l + \left(1-\varepsilon\right)\rho_c\right) = \dot{Q}_{in}\rho_{in} + \dot{Q}_{rec}\left(\varepsilon\rho_l + \left(1-\varepsilon\right)\rho_c\right) - \dot{Q}_{out}\left(\varepsilon\rho_l + \left(1-\varepsilon\right)\rho_c\right) - \dot{Q}_v\rho_v$$

[A4.13]

The partial differentiation of the l.h.s. of equation A4.13.

$$V\frac{d}{dt}\left(\varepsilon\rho_l + \left(1-\varepsilon\right)\rho_c\right) = -V\left(\rho_c - \rho_l\right)\frac{d\varepsilon}{dt} \qquad \text{[A4.14]}$$

The population balance equation (A4.3) and the mass balance (A4.13) are combined.

$$V\left(\rho_c - \rho_l\right)\left(3k_v\int_0^\infty GnL^2 dL + \frac{\dot{Q}_{rec}}{V}\left(1-\varepsilon\right) - \frac{\dot{Q}_{out}}{V}\left(1-\varepsilon\right) + k_v\int_0^\infty Q_{agg}L^2 dL\right) \qquad \text{[A4.15]}$$
$$= \dot{Q}_{in}\rho_{in} + \dot{Q}_{rec}\left(\varepsilon\rho_l + \left(1-\varepsilon\right)\rho_c\right) - \dot{Q}_{out}\left(\varepsilon\rho_l + \left(1-\varepsilon\right)\rho_c\right) - \dot{Q}_v\rho_v$$

The final mass balance is:

$$\frac{\dot{Q}_v}{V}\rho_v = \frac{\dot{Q}_{in}}{V}\rho_{in} + \left(\frac{\dot{Q}_{rec}}{V} - \frac{\dot{Q}_{out}}{V}\right)\rho_l - \left(\rho_c - C\rho_l\right)\left(3k_v\int_0^\infty GfL dL + k_v\int_0^\infty \tilde{Q}_{agg}L^2 dL + k_v\int_0^\infty \tilde{S}L^2 dL\right)$$

[A4.16]

Appendix 5: Validation experiments

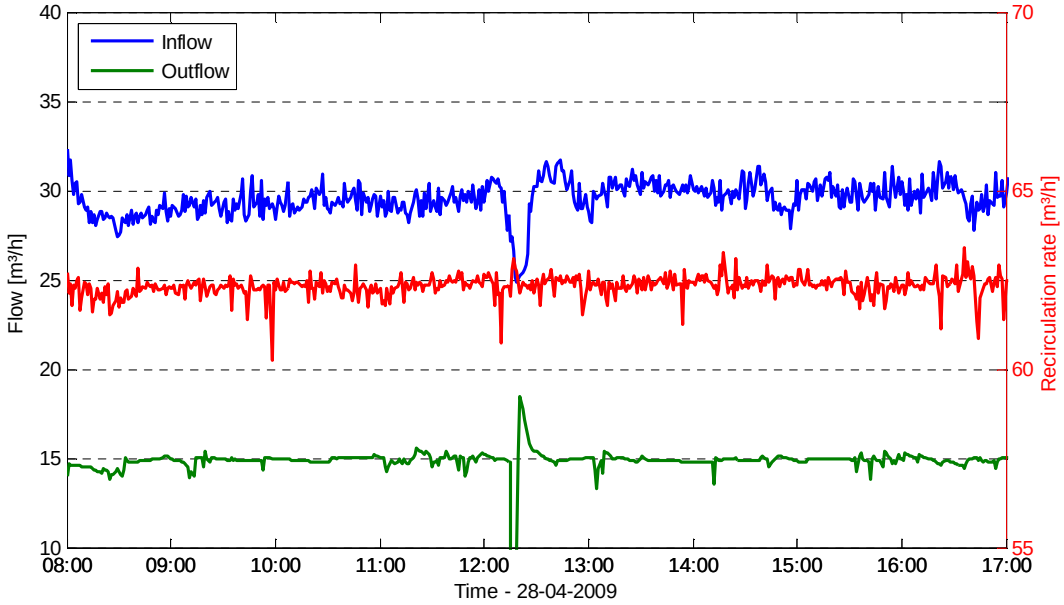

Figure A5.1: The flow rate of the incoming stream, out coming stream and the recirculation stream plotted with time for the rotation experiment.

The validation experiments were done at different values for the temperature and recirculation rate. The stirrer speed and residence time are kept constant at 35 rpm and 1,6 hours, respectively.

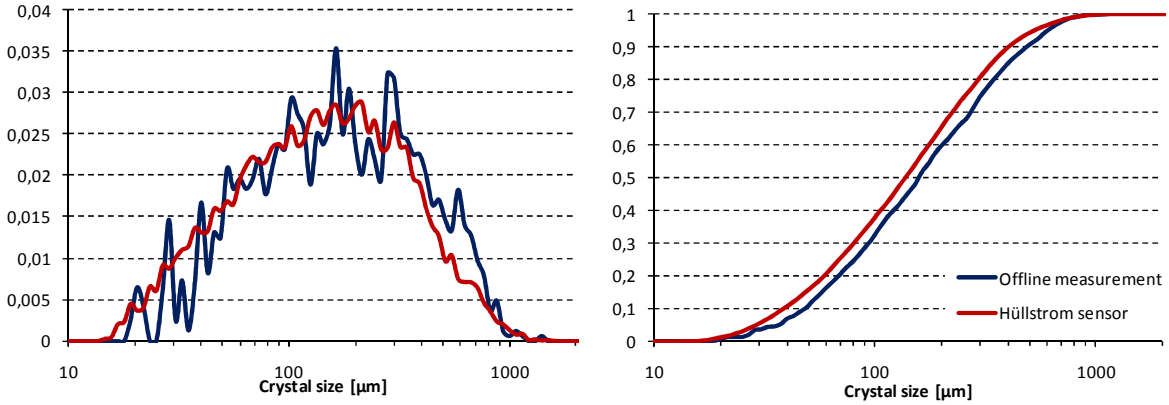

Figure A5.2: Crystal size distribution of the on-line and off-line measurement at 55°C and 30 m³/h for the recirculation rate. *Left:* Normalized particle number distribution. *Right:* Cumulative number distribution.

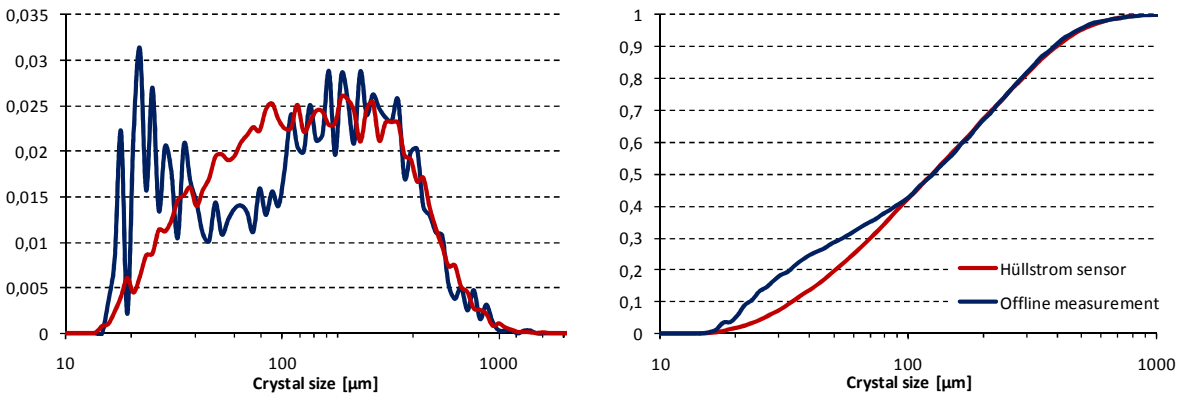

Figure A5.3: Crystal size distribution of the on-line and off-line measurement at 55°C and 60 m³/h for the recirculation rate. *Left:* Normalized particle number distribution. *Right:* Cumulative number distribution.

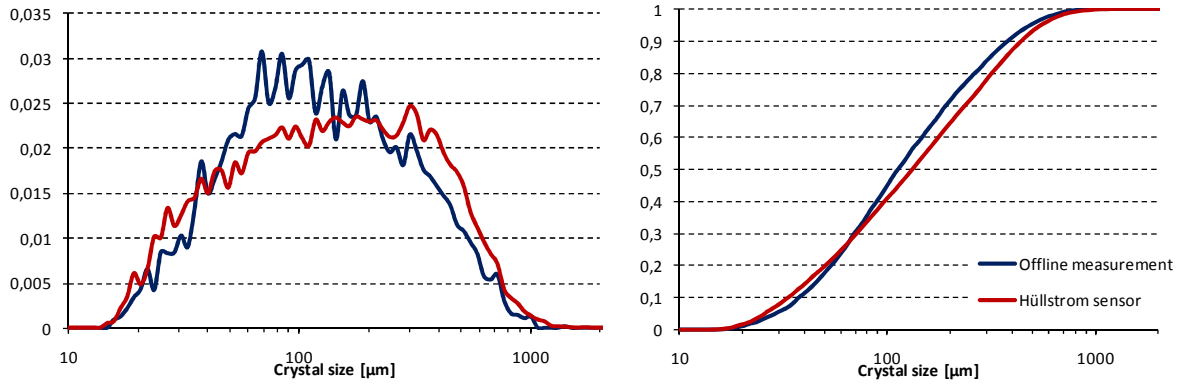

Figure A5.4: Crystal size distribution of the on-line and off-line measurement at 60°C and 60 m³/h for the recirculation rate. *Left:* Normalized particle number distribution. *Right:* Cumulative number distribution.

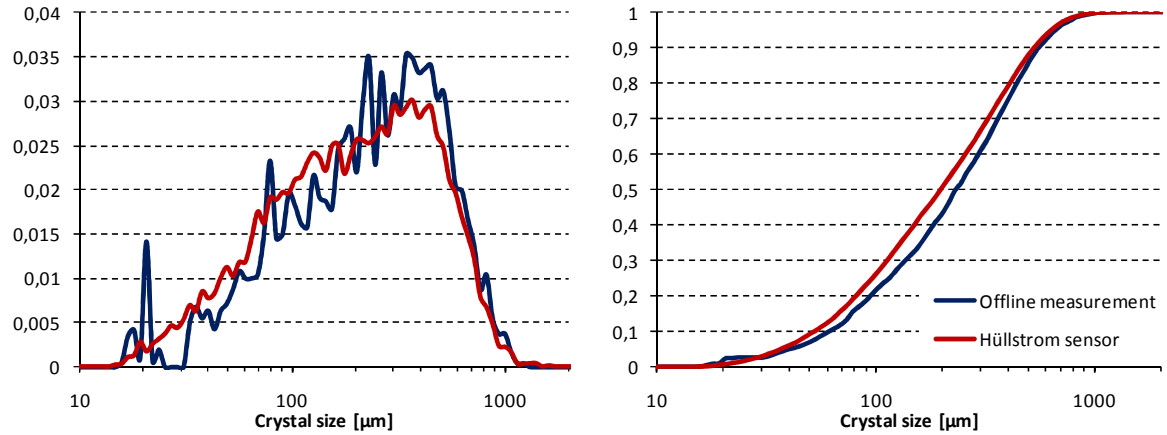

Figure A5.5: Crystal size distribution of the on-line and off-line measurement at 65°C and 60 m³/h for the recirculation rate. *Left:* Normalized particle number distribution. *Right:* Cumulative number distribution.

Appendix 6: Steady state experiments

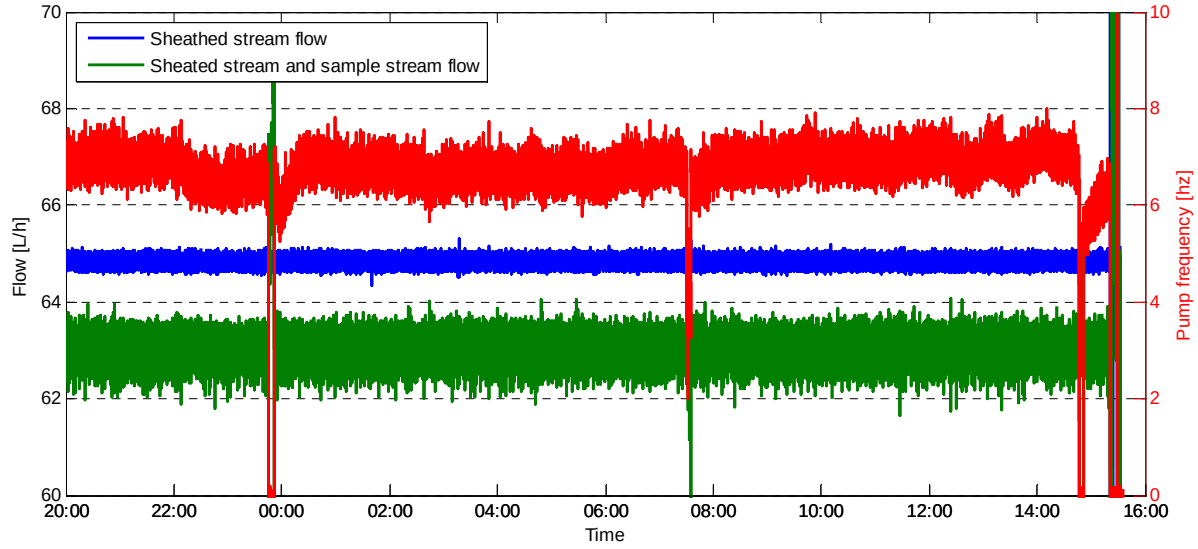

Figure A6.1: The flow of the sheathed stream and the flow of the combined product and sheathed stream is plotted in time. The difference is the sample rate of the sensor. The pump frequency represent the stability of the sensor.

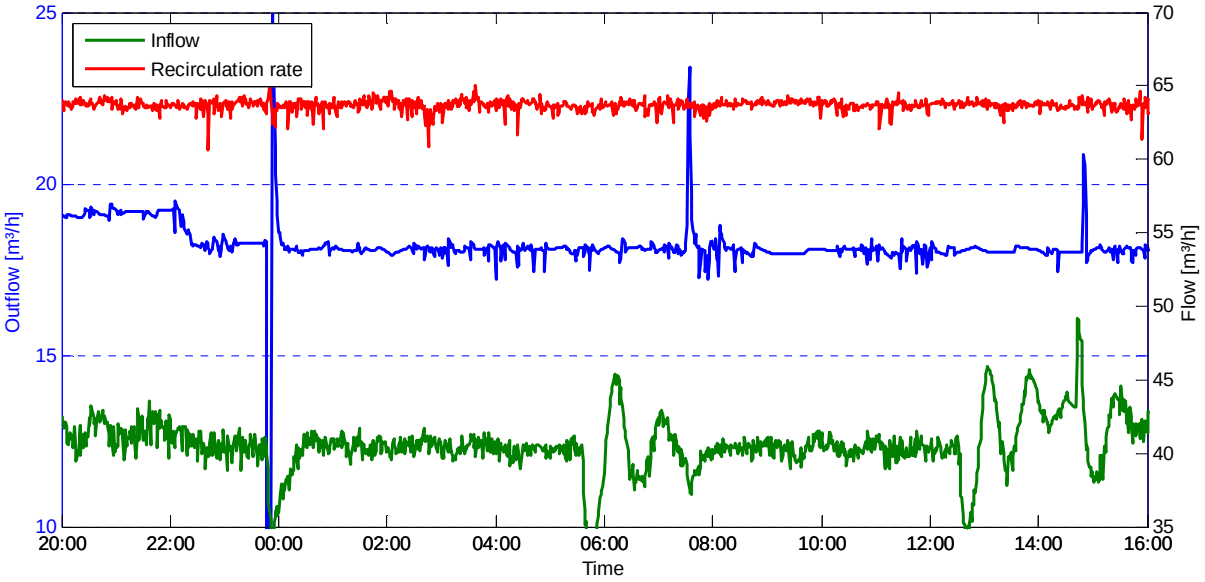

Figure A6.2: The flow rate of the incoming stream, out coming stream and the recirculation stream plotted in time.

Table A6.1: Static process parameters of 14 & 15-05-2009

Process parameter		*unit*
Temperature	59.5	°C
Pressure	200	mbar
Level	73	%
Stirrer speed	34.9	rpm
Recirculation temperature	65	°C
Concentration	40	wt-%

Appendix 7: Temperature experiments

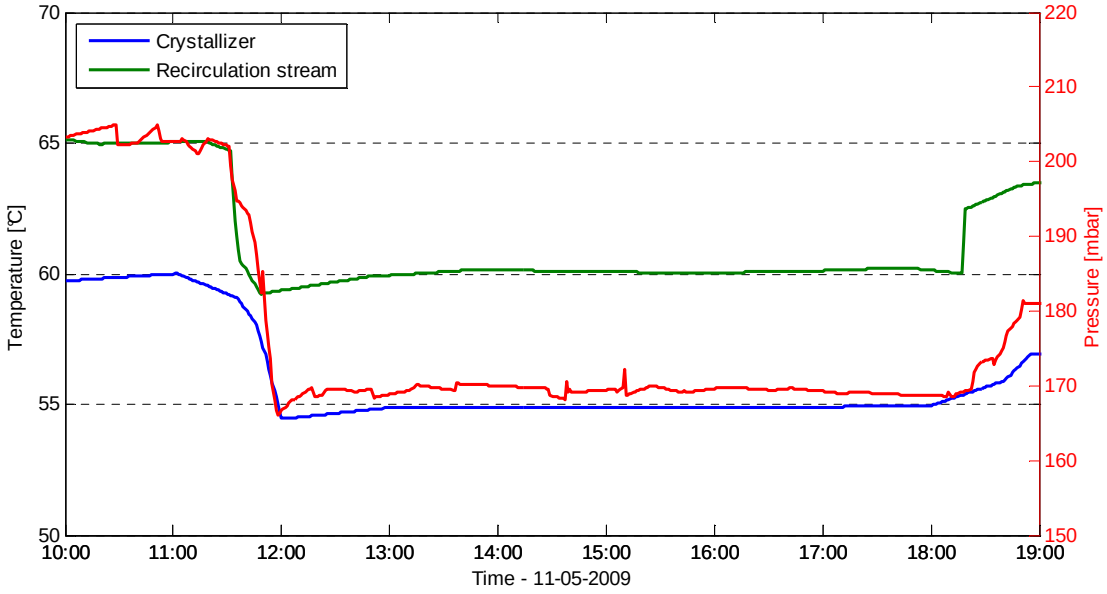

Figure A7.1: The temperature in the crystallizer and in the recirculation stream plotted in time. Also the pressure in the crystallizer is plotted in time.

Table A7.1: Static process parameters of 11-05-2009

Process parameter		*unit*
Inflow	38	m³/h
Outlet flow	16	m³/h
Residence time	1.85	h
Level	73	%
Stirrer speed	34.9	rpm
Recirculation temperature	62	m³/h
Concentration	40.2	wt-%

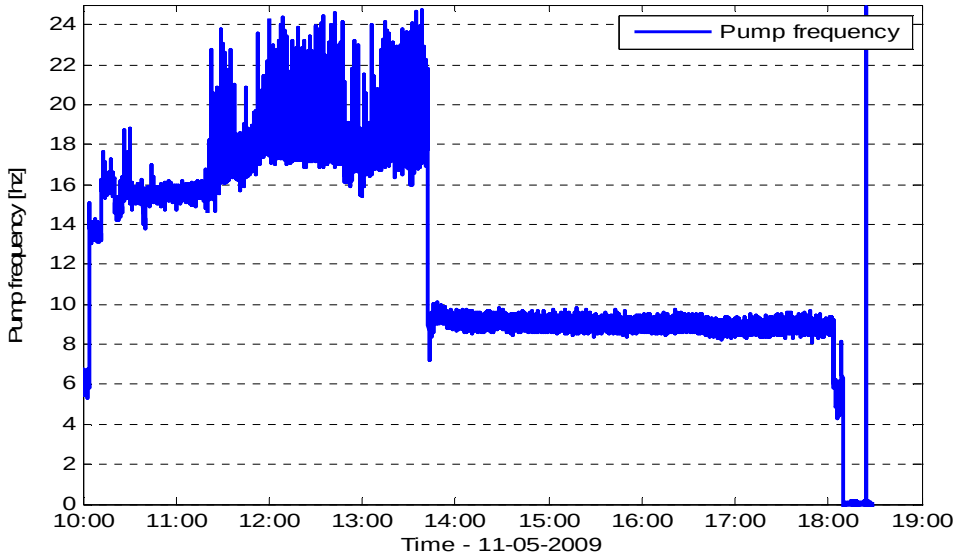

Figure A7.2 The pump frequency of the sensor, it represent the stability of the sensor. Between 11:30h and 14:00 the frequency is not stable probably the crystal concentration is too high.

Appendix 8: Stirrer speed experiments

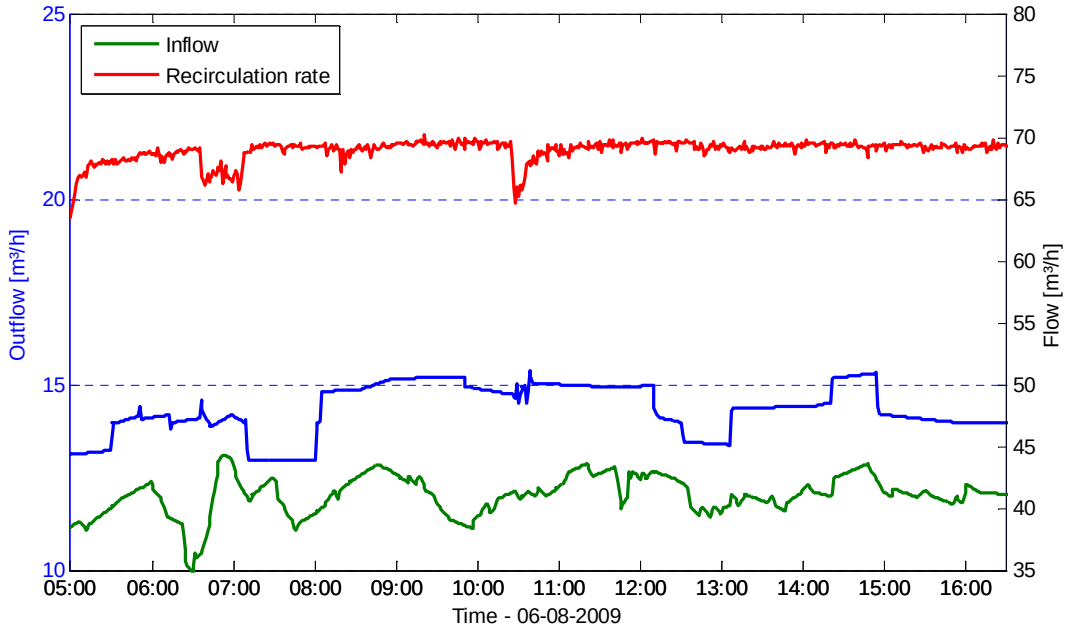

Figure A8.1: The flow rate of the incoming stream, out coming stream and the recirculation stream.

Table A8.1: Static process parameters of 06-08-2009.

Process parameter		*unit*
Temperature	60.3	°C
Pressure	219	mbar
Level	73	%
Stirrer speed	34.9	rpm
Recirculation temperature	65	°C
Concentration	40	wt-%

Appendix 9: Recirculation rate experiments

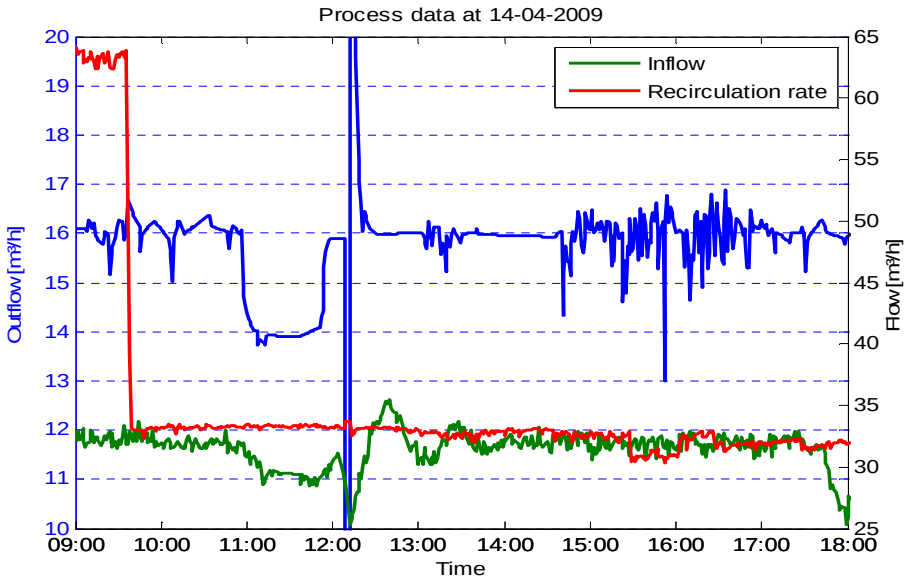

Figure A9.1: The flow rate of the incoming stream, out coming stream and the recirculation stream plotted in time.

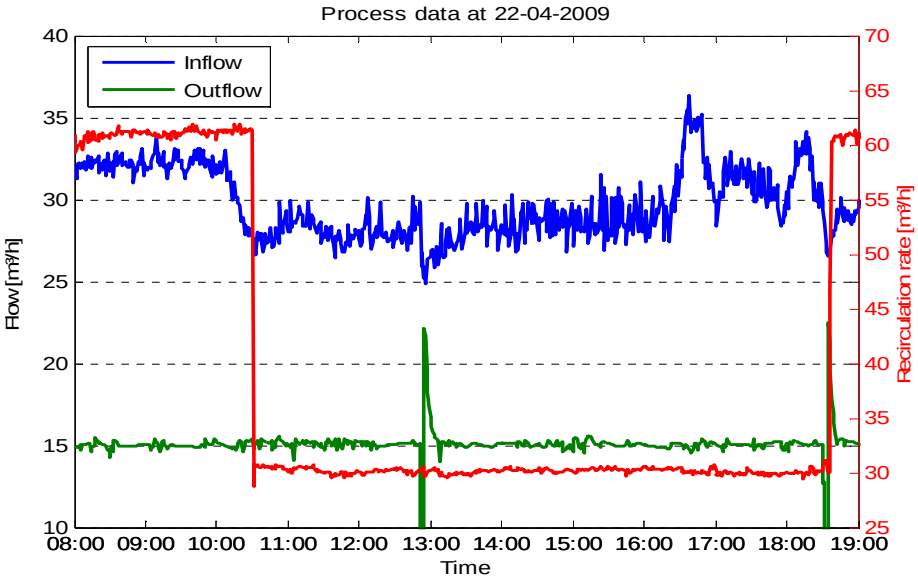

Figure A9.2: The flow rate of the incoming stream, out coming stream and the recirculation stream plotted in time.

Table A9.1: Static process parameters of 14-04-2009 and 22-04-2009.

Process parameter	*14-04*	*22-04*	*unit*
Temperature	59.3	59.2	°C
Pressure	200	200	mbar
Level	74	73	%
Stirrer speed	34.9	34.9	rpm
Recirculation temperature	65	65	°C
Concentration	40	40	wt-%

Appendix 10: Numerical solutions of population balance equations for nucleation, growth and aggregation processes

Shamsul Qamar and Gerald Warnecke (2007a,b)

A comparison between the numerical solutions of the PBE and the numerical solution of Qamar and Warnecke.

Pure Growth (constant growth)

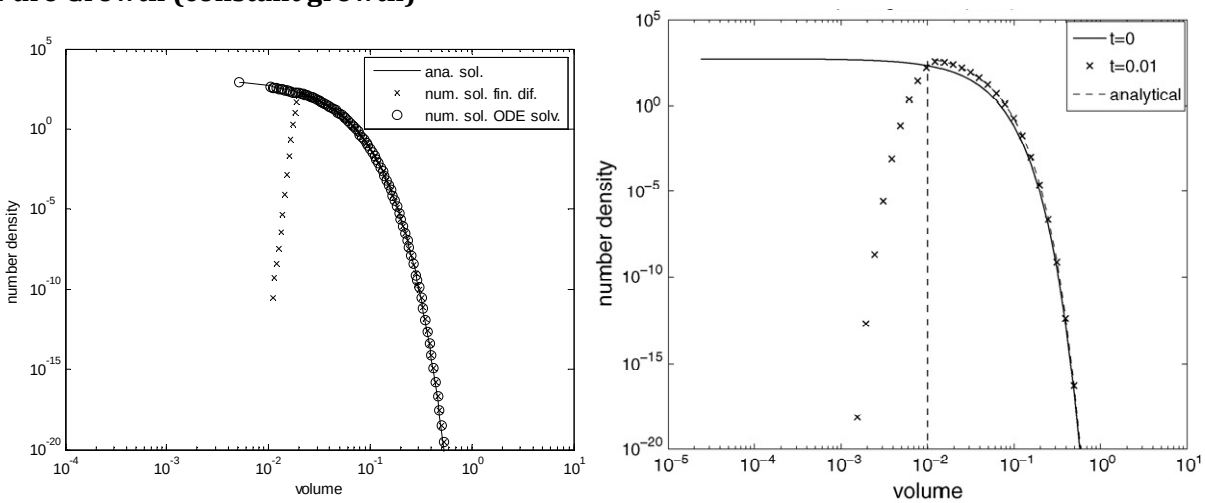

Figure A10.1: *Left:* Two kind of numerical solutions (finite difference and ODE solver) compared with the analytical solution at t = 0,01. Number of grids = 150, q = 15. *Right:* The numerical solution of Qamar and Warnecke (2007a) with the finite volume scheme.

Constant growth and stiff nucleation

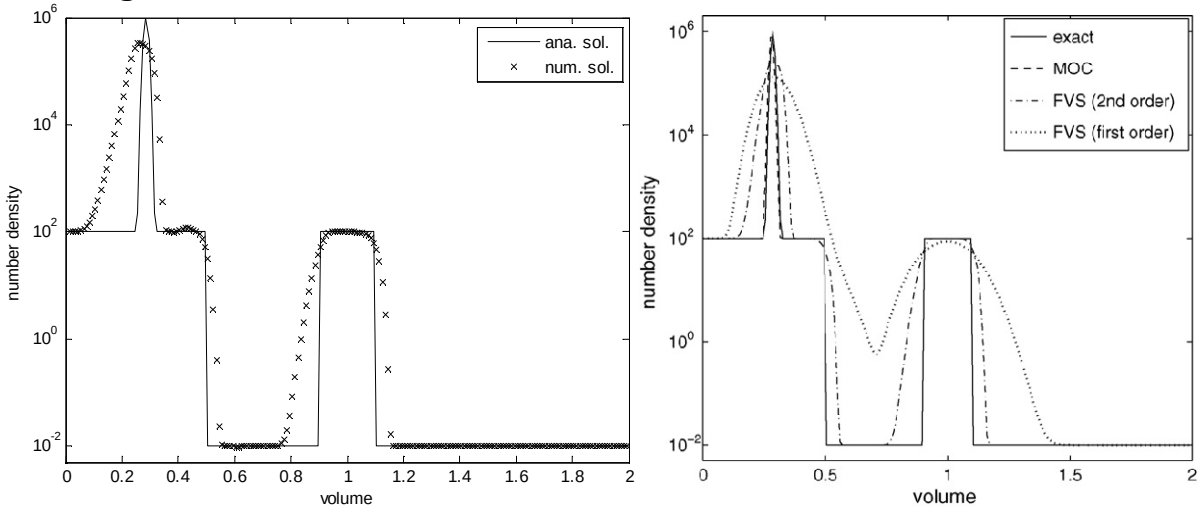

Figure A10.2: *Left*: Numerical solution and analytical solution for constant growth and stiff nucleation on a linear grid. *Right*: The numerical solution of Qamar and Warnecke (2007a) with different methods.

Constant growth and exponential nucleation

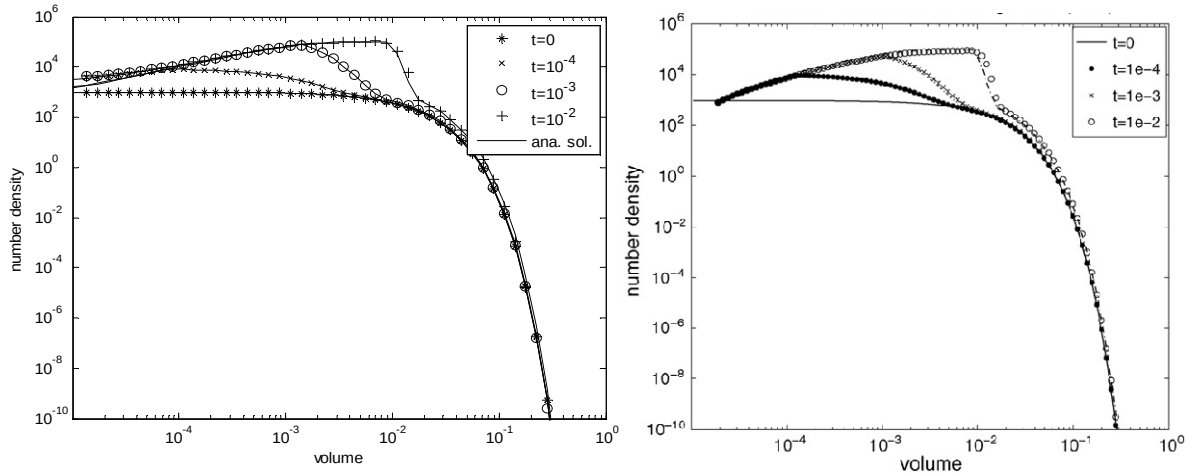

Figure A10.3: *Left:* Numerical solution and analytical solution for constant growth and exponential nucleation on a geometric grid. Number of grids = 50, q = 4. *Right:* The numerical solution and analytical solution of Qamar and Warnecke (2007a) at different times.

Aggregation with constant kernel

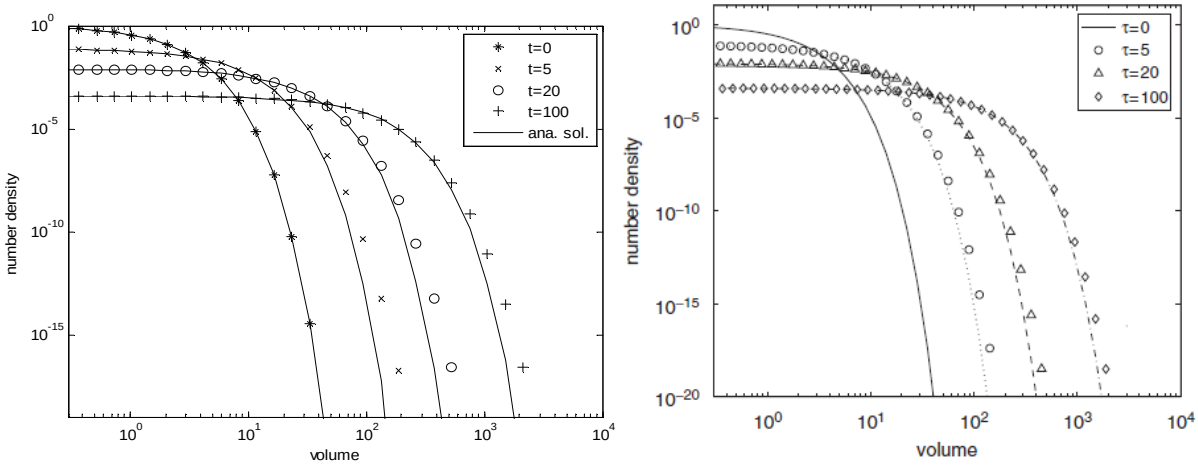

Figure A10.4: *Left*: Numerical solution and analytical solution of aggregation problem with constant kernel at different times. Number of grids = 40, q = 2. *Right*: Numerical solution and analytical solution of Qamar and Warnecke (2007b) at different times.

Constant growth and aggregation with constant kernel

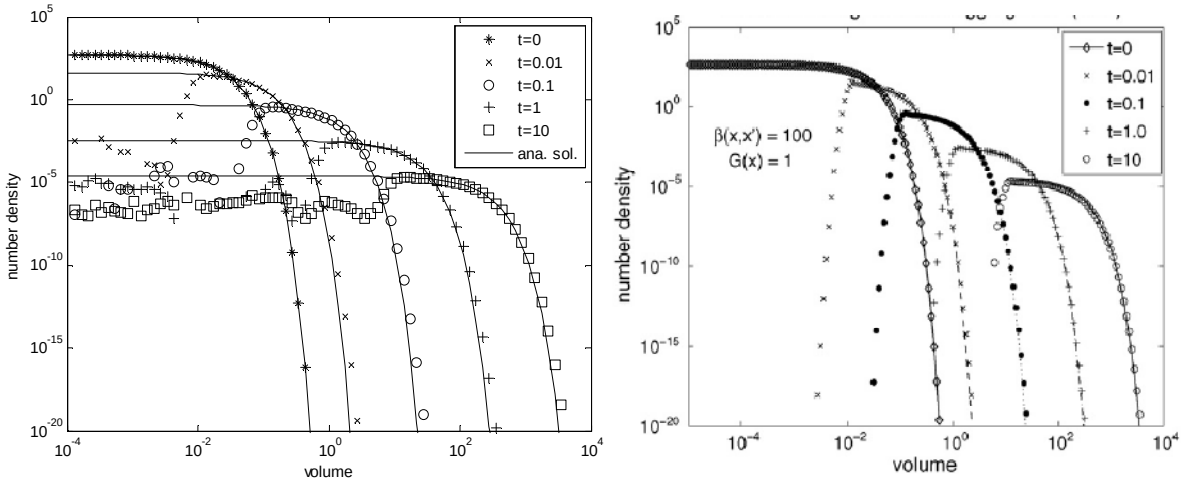

Figure A10.5: *Left:* Numerical solution and analytical solution of a growth and aggregation problem with constant growth (G=1) and a constant kernel (B=100) at different times. Number of grids: 80, q = 3. *Right:* Numerical solution and analytical solution of Qamar et al. (2007) at different times.

Linear growth and aggregation with constant kernel

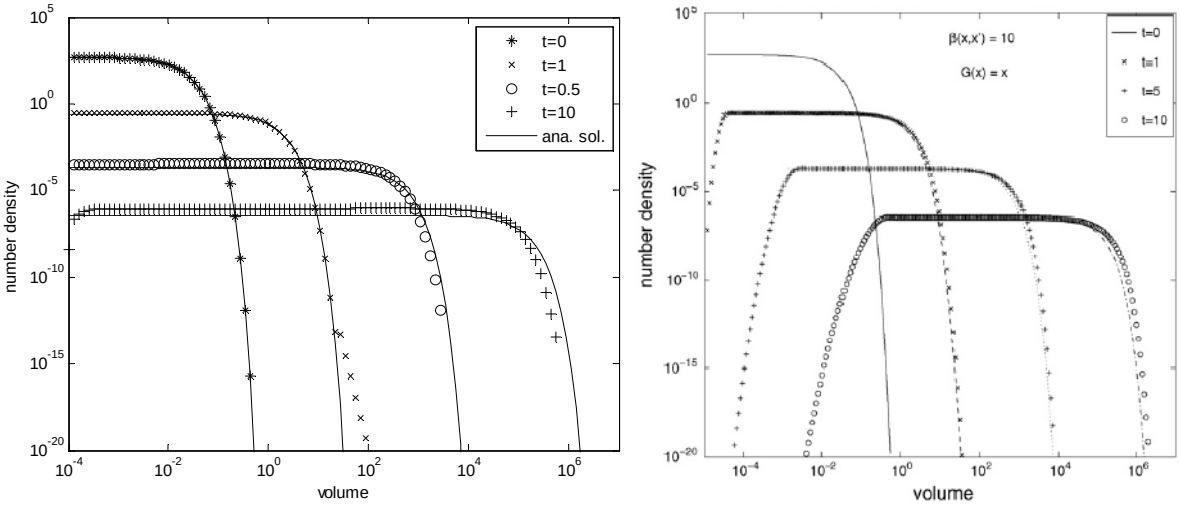

Figure A10.6: *Left:* Numerical solution and analytical solution of a growth and aggregation problem with linear growth (G=x) and a constant kernel (B=10) at different times. Number of grids: 150, q = 3. *Right:* Numerical solution and analytical solution of Qamar and Warnecke (2007a) at different times.

Appendix 11: Modelling of the CSD measured at 07-05-2009

The simulated CSD and concentration profile are shown in Figure A11.1.

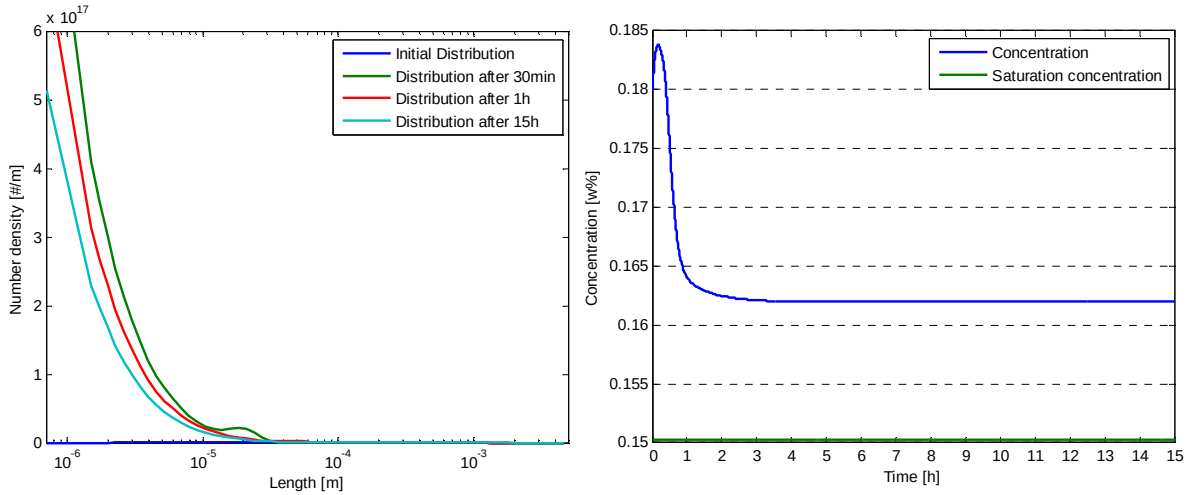

Figure A11.1: *Left:* The simulated CSD after 30 minutes, 1 hour and after 15 hours. *Right:* The concentration in the crystallizer versus the time. The saturation concentration is also plotted.

The coefficient of variation is shown in Figure A11.2.

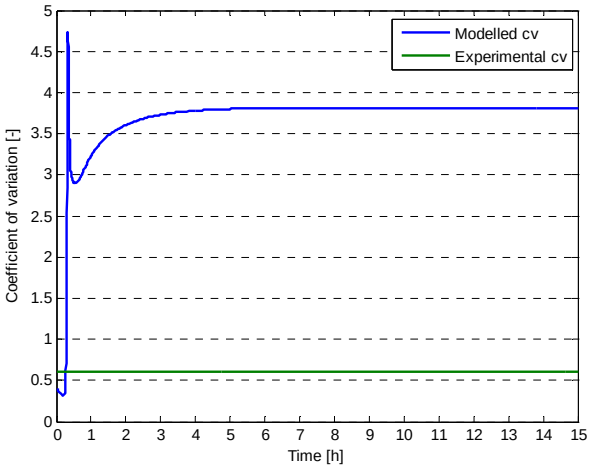

Figure A11.2: The coefficient of variation plotted in time. The green line is the experimental determined coefficient of variation.

Appendix 12: The MATLAB code of the model structure

```
% Growth, nucleation and agglomeration problem, Solution method:
% Second order fully one-sided upwind scheme (kappa=-1) with van Leer's
flux limiter [Qamar et al., 2006]
% Test problem BASF plant:              Size-independent growth
%                                       Agglomeration with constant kernel
%                                       Initial distribution with 2.5% wt-%
%                                       crystals
%                                       Stiff nucleation
clc
clear
tic

%% Constant parameters of the crystallizer and the dissolver
Vc = 34.1;  %[m3], Volume crystallizer or Vc=28.817*L+13.086 (L=level
crystallizer)
T = 60;                             %[C], Temperature of the crystallizer
Csat = 0.7087*exp(0.0509*T)/100;    %[-], Concentration fraction at
                                     saturation (T=temperature crystallizer)
Trec = 65;                  %[°C], Temperature of the recirculation stream
Tfeed = 80;                 %[°C], Temperature of the feed stream

Qin = 20/3600;              %[m³/s], Inlet flow crystallizer
Qout = 77/3600;             %[m³/s], Outlet flow crystallizer
Qrec = 60/3600;             %[m³/s], Recirculation flow crystallizer
Qprod = Qout-Qrec;          %[m³/s], Product flow

RT = Vc/Qprod;              %[s], Residence time
RT_h=RT/3600;               %[h], Residence time

Mtilda = 0.14614;           %[kg/mol], Molar mass of adipic acid [Ullmann]
Rs = 1.0000e-006;           %[Jm / mol], Fit parameter Gahn Model
R = 8.314472;               %[J/K mol], Ideal gas constant
Dab = 1.45E-9;              %[m2/s], Diffusivity [Westhoff, 2003]

Ne = 0.72;                  %[], Newton number [BASF]
Nimp_Crys = 35;             %[rpm], Impeller frequency of the crystallizer
Nimp = Nimp_Crys*0.0167;    %[1/s], Impeller frequency of the crystallizer
Dimp = 2.1;                 %[m], Propeller diameter [Neumann, 2001]
epsilon_imp = (Ne*Nimp^3*Dimp^5)/Vc;  %[m2/s3], Mean specific power input
of the impeller in the crystallizer [Bermingham, 2003]
grav = 9.81;                %[m/s2], Gravitational constant
kr =  2.2169e-004;          %[m/s], Rate constant for surface integration

%% Density
rhocrystal = 1344;      %[kg/m3], Density of crystals Several references
rholiquid  = 1011;      %[kg/m3], Density of a saturated crystal free
adipic acid solution, Westhoff
rhowater = 983.23;      %[kg/m3], Density of water at 60 C Data compagnion
rhoin = 1048;           %[kg/m3], Density of a saturated crystal free
adipic acid solution at 80°C, Westhoff this value is an estimation out of
range

%% Viscosity
visliquid = 0.0004665;    %[Pa.sec], Viscosity of water at 60C [HBCP, 1990]
Kinvis = visliquid/rholiquid;   %[m2/s], Kinematic viscosity of the
saturated crystal free solution at 50 C [Jager, 1990]
```

```
%% Constant parameters for the solute concentration equation
kv = 0.55;          %[-], Volumetric shape factor [used by BASF]
Hc = 115E+3;        %[J/kg], Specific enthalpy of crystals [Ullmann]
Hl = 230E+3;        %[J/kg], Specific enthalpy of liquid 10-20C: 214, 90-
100C: 241. [Ullmann]
Hv = 2.3601E+6;     %[J/kg], Enthalpy of vaporization of water at 60°C
Cp_l = 4022;        %[J/(kg*K)] Specific heat saturated adipic acid solution
@ 50C Westhoff
Cp_c = 1590;        %[J/(kg*K)] Specific heat adipic acid crystals @ 50C
Westhoff

%% Initial concentrations
Ccrysin = 0.18;     %[-], Inlet concentration in wt-%
Cin = 0.4;          %[-], Feed concentration in wt-%
Crys_frac = 0.025;  %[kg/kg] Crystal fraction initially in the crystallizer

%% Parameters for growth, nucleation and agglomeration
a1 = 1e-2;      % Nucleation parameter a1*int(n*L^3dL)_a2-inf
a2 = 27;        % Nucleation parameter a1*int(n*L^3dL)_a2-inf
a3 = 1e-7;      % Growth parameter a3*(C-Csat/Csat)^a4
a4 = 0.7;       % Growth parameter a3*(C-Csat/Csat)^a4
B = 5.58e-15;   % Constant agglomeration rate

%% Boundary and initial conditions
t0 = 0;
tmax = 3600*15;                     %[s] 15h is app 10x residence time

Lmin = 1e-10;                       %[m] Minimum grid length
Lmax = 5e-3;                        %[m] Maximum grid length
ngrids = 60;                        % Number of grids 100
q = 5;                              % Geometric grid factor

epsilon = 1e-10;                    % To avoid division by zero

% Geometric grid mesh
Lhalf(1) = Lmin;

for i = 2:ngrids+1
    Lhalf(i)=Lmin+2^((i-1-ngrids)/q)*(Lmax-Lmin);
end

for i = 1:ngrids
    L(i) = (Lhalf(i)+Lhalf(i+1))/2;
    dL(i) = Lhalf(i+1)-Lhalf(i);
end

% Initial distribution
Og=1.5;                             % Width of the distribution
L0g=100e-6;                         % Mean crystal size
for i=1:ngrids-1
FLOG(i+1) = ((1/L(i+1))*(1/(log(Og)*sqrt(2*pi)))*exp(-
1*(((log(L(i+1)/L0g))^2)/(2*(log(Og))^2))));
%[#m3/m3 m], First log-normal distribution
v(i+1) = FLOG(i+1);                 %[#m3/m3 m], Initial volume distribution
f0(i+1) = Crys_frac*(v(i+1))/(kv*(L(i+1)^3));
%[#/m3 m], Initial number distribution
end
```

```
g0 = f0.*L;

%% Solving the PBE
options = odeset('RelTol',1E-6,'AbsTol',1E-6);
[t,X] = ode15s(@Final_model_ODE_v3,[t0 tmax],[Ccrysin
g0],[],L,dL,Lhalf,epsilon,ngrids,Lmin,Lmax,B,a1,a2,a3,a4,Csat,kv,Vc,rholiqu
id,rhocrystal,rhoin,Hl,Hc,Hv,Cin,Qrec,Qprod,Qout,Qin,Cp_l,Cp_c,T,Trec,Tfeed
,q);
[s1,s2] = size(X);

C = X(:,1);                 %[kg solute/kg solution] Solute concentration

for k = 1:length(t)
    f(k,:) = X(k,2:s2)./L;   %[#/m] Number density
end

%% Moments
for i=1:length(t)
    m0(i) = sum(f(i,:) .* dL);              %[#], 0th moment of time step
    m1(i) = sum(f(i,:) .* L .* dL);         %[m], 1th moment of time step
    m2(i) = sum(f(i,:) .* L.^2 .* dL);      %[m2], 2nd moment of time step
    m3(i) = sum(f(i,:) .* L.^3 .* dL);      %[m3], 3th moment of time step
    m4(i) = sum(f(i,:) .* L.^4 .* dL);      %[m4], 4th moment of time step
end

cv = (m2.*m0./(m1.^2)-1).^0.5;
m4_m3 = m4./m3;
epsilon_c = kv.*m3;

%% Plot of the solution
j = [1 399 452 length(t)];
Figure(1)
clear gcf
semilogx(L(:),f(j,:),'Linewidth',1.5)
axis([0.7e-6 5e-3 0 6e17])
legend('Initial Distribution','Distribution after 30min','Distribution
after 1h','Distribution after 15h')
xlabel('Length [m]')
ylabel('Number density [#/m]')

Figure (2)
clear gcf
plot(t./3600,C,t./3600,0.7087*exp(0.0509*T)/100*ones(length(t),1),'Linewidt
h',1.5)
xlabel('Time [h]')
ylabel('Concentration [wt-%]')
set(gca,'xtick',[0:15],'ygrid','on')
legend('Concentration','Saturation concentration')

Figure (3)
clear gcf
m4_m3b=[m4_m3' 549e-6*ones(length(t),1)];
[AX,H1,H2] = plotyy(t/3600,m4_m3b,t/3600,epsilon_c);
xlabel('Time [h]')
set(get(AX(1),'ylabel'),'string','Mean crystal size [m]')
set(get(AX(2),'ylabel'),'string','Crystal fraction [-]')
set(AX(1),'Xtick',[0:15],'Ytick',[0:0.10e-3:0.70e-3],'Ylim',[0 0.70e-
3],'Ygrid','on')
set(AX(2),'Ytick',[0:0.05:0.35],'Ylim',[0 0.35])
```

```
legend(H1,'Modelled mean crystal size','Experimental mean crystal
size','location','SouthEast');
set(H1,'Linewidth',1.5)
set(H2,'Linewidth',1.5)

Figure(4)
clear gcf
plot(t/3600,cv,t/3600,0.614*ones(length(t),1),'Linewidth',1.5)
xlabel('Time [h]')
ylabel('Coefficient of variation [-]')
set(gca,'xtick',[0:15],'ygrid','on')
legend('Modelled cv','Experimental cv')

disp('m4/m3'),disp(m4(length(t))/m3(length(t)))
disp('epsilon'),disp(epsilon_c(length(t)))
disp('m0'),disp(m0(length(t)))
disp('m1'),disp(m1(length(t)))
disp('m2'),disp(m2(length(t)))
disp('m3'),disp(m3(length(t)))
disp('m4'),disp(m4(length(t)))

toc
```

The function file with the ODE´s.

```
function dX_dt =
Final_model_ODE_v3(t,X0,L,dL,Lhalf,epsilon,N,Lmin,Lmax,B,a1,a2,a3,a4,Csat,k
v,Vc,rholiquid,rhocrystal,rhoin,Hl,Hc,Hv,Cin,Qrec,Qprod,Qout,Qin,Cp_l,Cp_c,
T,Trec,Tfeed,q)

C=X0(1);
f=X0(2:length(X0))';

% if t>180000
%     T=55;
%     Csat = 0.7087*exp(0.0509*T)/100;     %[-], Concentration fraction at
saturation (T=temperature crystallizer)
% end

% Growth kinetics
G = a3*((C-Csat)/Csat)^a4;                  % Evans growth kinetics

m3= f.*L.^2.*dL;                            %[m3], 3th moment of time step
epsilon_p = 1 - kv*sum(m3);                 %[], Liquid fraction in the bulk

% The nucleation section
B0 = a1*sum(m3(a2:length(m3)));

% The agglomeration section
Vhalf = kv.*Lhalf.^3;
V = kv.*L.^3;

Fhalfmin = 0;
Fhalfmax = 0;

for i=1:N-1
    sumk = zeros(N,1);
    for k = 1:i
        Vdif = Vhalf(i+1)-V(k);
```

```
        if Vdif < Vhalf(2)
            Vdif = Vhalf(2);
        end
        alpha = ceil(q*log(((Vdif/kv)^(1/3)-Lmin)/(Lmax -
Lmin))/log(2)+N+1);
        int1 = zeros(N,1);
        for j = alpha:N
            int1 (j) = B/V(j)*(Vhalf(j+1)-Vhalf(j))*f(j);
        end
        int2 = B/Vhalf(alpha)*(Vhalf(alpha)-(Vhalf(i+1)-V(k)))*f(alpha-1);
        sumk (k) = (sum(int1)+int2)*(Vhalf(k+1)-Vhalf(k))*f(k);
    end
    Fphalf (i) = sum(sumk);
end

% For i = 1
Q_agg(1)= -(Fphalf(1)-Fhalfmin)/(Vhalf(2)-Vhalf(1));
for i=2:N-1
    Q_agg(i)= -(Fphalf(i)-Fphalf(i-1))/(Vhalf(i+1)-Vhalf(i));
end
Q_agg(N) = -(Fhalfmax - Fphalf(N-1))/(Vhalf(N+1)-Vhalf(N));

% Concentration balance
Integral = kv*3*sum(G.*f.*L.*dL)+kv*sum(Q_agg.*L.^2.*dL);
dCdt = 1/(epsilon_p*rholiquid)*(Qin/Vc*Cin*rhoin+(Qrec-
Qout)/Vc*C*rholiquid-(rhocrystal-C*rholiquid)*Integral);

% Solving the PBE
% The first finite control volume
Gnim(1) = B0*L(1);                                          % (G*n)@L_1/2
Gnip(1) = G*(((2*(L(2)-L(1))-dL(1))*f(1)+dL(1)*f(2))/(2*(L(2)-L(1))));
% (G*n)@L_3/2
% This expression is obtained from the interpolation relation when kappa=1

df_dt(1)= -(1/dL(1)*(Gnip(1)-Gnim(1))) + Q_agg(1) + G*f(1)/L(1) +
Qrec*f(1)/Vc - Qout*f(1)/Vc;

for i= 2:N-1
    r = (f(i)-f(i-1)+epsilon)/(f(i+1)-f(i)+epsilon);
      % Upwind ratio of two consecutive solution gradients
    FluxL = (abs(r)+r)/(1+abs(r)); % Flux limited function [van Leer, 1985]

    Gnim(i) = Gnip(i-1);           % (G*n)@L_iminus
    Gnip(i) = G*(f(i)+dL(i)/(2*(L(i)-L(i-1)))*FluxL*(f(i+1)-f(i)));
% (G*n)@L_iplus
    df_dt(i) = -(1/dL(i)*(Gnip(i)-Gnim(i))) + Q_agg(i) + G*f(i)/L(i) +
Qrec*f(i)/Vc - Qout*f(i)/Vc;       % Explicit Euler integration scheme
end

% The last finite control volume
Gnim(N) = Gnip(N-1);            % (G*n)@L_(N-1/2)
Gnip(N) = G*(f(N)+dL(N)/(2*(L(N)-L(N-1)))*(f(N)-f(N-1))); %(G*n)@L_(N+1/2)
% This expression is obtained from the interpolation relation when kappa=-1

df_dt(N) = -(1/dL(N)*(Gnip(N)-Gnim(N)))+Q_agg(N)+G*f(N)/L(N) + Qrec*f(N)/Vc
- Qout*f(N)/Vc;
df_dt = df_dt';

dX_dt = [dCdt; df_dt];
```